Smart Sensors, Measurement and Instrumentation 17

Erick Gonzalez Rodriguez

Reconfigurable Transceiver Architecture for Multiband RF-Frontends

Springer

Smart Sensors, Measurement and Instrumentation

Volume 17

Series editor

Subhas Chandra Mukhopadhyay
School of Engineering and Advanced Technology (SEAT)
Massey University (Manawatu)
Palmerston North
New Zealand
e-mail: S.C.Mukhopadhyay@massey.ac.nz

More information about this series at http://www.springer.com/series/10617

Erick Gonzalez Rodriguez

Reconfigurable Transceiver Architecture for Multiband RF-Frontends

Springer

Erick Gonzalez Rodriguez
Institut für Mikrowellentechnik und
Photonik (IMP)
Fachbereich Elektrotechnik und
Informationstechnik (ETiT) D17
Technische Universität Darmstadt
Darmstadt
Germany

ISSN 2194-8402 ISSN 2194-8410 (electronic)
Smart Sensors, Measurement and Instrumentation
ISBN 978-3-319-24579-9 ISBN 978-3-319-24581-2 (eBook)
DOI 10.1007/978-3-319-24581-2

Library of Congress Control Number: 2015950007

Springer Cham Heidelberg New York Dordrecht London

Printed on acid-free paper

Springer International Publishing AG Switzerland is part of Springer Science+Business Media
(www.springer.com)

To my parents:
Lulú and Santiago,
inspiring energy sources of motivation

Foreword

This book presents my research carried out in the Institute of Microwave Engineering and Photonics at Technische Universität Darmstadt.

First of all I would like to express my gratitude to my supervisor Prof. Dr.-Ing. Rolf Jakoby. Without his valuable guidance and warm encouragement, this work could have not been performed.

I deeply appreciate Dr.-Ing. Holger Maune, Dr.-Ing. Yuliang Zheng and Dr.-Ing. Matthias Maasch for their trust, inspiring discussions and constructive support throughout the last years. For the cordial friendship and fruitful advices, I thank Dr.-Ing. Martin Schüßler, Prof. Dr.-Ing. Christian Damm, Dr.-Ing. Margarita Puentes, Dr.-Ing. Alexander Gäbler, Dr.-Ing. Mohsen Sazegar, Dr.-Ing. Onur Karabey, Dr.-Ing. Andreas Penirschke, Dr.-Ing. Christian Mandel, Dr.-Ing. Sebastian Strunck, Saygin Bildik, Matthias Höfle, Carsten Fritzsch, Aleksandar Angelovski, Matthias Hansli, Alex Wiens, Matthias Jost, Tobias Franke, Ananto Eka Prasetiadi, Mohammad Nikfalazar, Wenjuan Hu, Donghang Lu, Arshad Mehmood, María Roig Parras, Bernd Kubina and Christian Weickhmann.

Special thanks to Prof. Dr.-Ing. Abdelhak Zoubir, Prof. Dr.-Ing. Klaus Hofmann, Prof. Dr.-Ing. Matthias Hollick, Lufei Shen, Jing Ning, Adrian Carlos Loch Navarro and Matthias Schulz for the great interdisciplinary cooperation within the framework of the research priority LOEWE Cocoon.

I would like also to thank Prof. Dr.-Ing. Kira Kastell at the University of Applied Sciences Frankfurt am Main and the company DEV-Systemtechnik for the teamwork and fruitful experience within the framework of the BERT Project; Dr.-Ing. Roland Dill, Maria Kaiser, Eleonore Titow, Traudel Micus, Heidi Rossmann, Karin Boye, Peter Kießlich and Andreas Semrad are also warmly thanked for their excellent administrative and practical support at the Institute of Microwave Engineering and Photonics.

Contents

Acronyms

4G	Forth generation of mobile communications
5G	Fifth generation of mobile communications
BER	Bit error rate
BST	Barium strontium titanate
C2C	Car-to-car communication
CR	Cognitive radio
CSN	Cooperative sensor network
DRA	Dielectric resonator antenna
EVM	Error vector magnitude
FMC	FPGA mezzanine card
FPGA	Field-programmable gate array
GSM	Global system for mobile communications
HV	High voltage
IoT	Internet of things
LTE	Long term evolution
M2M	Machine-to-machine communication
MIMO	Multiple input multiple output
MISO	Master in slave out
RF	Radio frequency
RFID	Radio frequency identification
Rx	Receiver
SDR	Software defined radio
SNR	Signal-to-noise ratio
SPI	Serial peripheral interface
TMN	Tunable impedance matching network
Tx	Transmitter
UMTS	Universal mobile telecommunications system
UWB	Ultrawideband
WARP	Wireless open-access research radio

Abstract

Cognitive Radio (CR) and Software Defined Radio (SDR), which have been mere proposals to solve the occupation of mobile services with limited resources more than two decades ago, are now enabled by technologies such as semiconductors, micro-electromechanical systems (MEMS) and ferroelectric Barium-Strontium-Titanate (BST) films offering full reconfigurability with a continuous frequency range of operation.

In this book, the hardware design and implementation is investigated and discussed to achieve smart air interfaces with a reduced number of Radio Frequency (RF) transmitter and receiver chains, or even with a single reconfigurable RF-Frontend in the user terminal. Various hardware challenges are identified and addressed to enable the implementation of autonomous reconfigurable RF-Frontend architectures. Such challenges are: (i) the conception of a transceiver with wide tuning range of at least up to 6 GHz, (ii) the system integration of reconfigurable technologies targeting current compact devices that demand voltages up to 100 V for adaptive controlling and (iii) the realization of a multiband and multistandard antenna module employing agile components to provide flexible frequency coverage.

A solid design of a reconfigurable frontend is proposed from the RF part to the digital baseband. Criteria such as Bit Error Rate (BER) and Error Vector Magnitude (EVM) are taken into account to better exploit the available frequency spectrum compared to conventional techniques. Minimization of the frequency dependence for agile RF components at a defined carrier frequency and signal bandwidth is demonstrated considering a tunable impedance matching network based on ferroelectric varactors. Therefore, system simulation of tunable components is performed in terms of BER and EVM for QPSK, 16-QAM and 64-QAM schemes. BER and EVM results evaluating signal bandwidths of 20 and 40 MHz are compared with current and future mobile standards exhibiting a difference of up to 4 dB in the SNR while applying tuning voltages between 0 and 90 V.

The system integration of different components in the reconfigurable RF-Frontend of a portable-oriented device architecture is demonstrated. Thus, to enable adaptive control of a dualband dielectric resonator antenna (DRA) via tunable matching network, the principle of a detector module is shown. Fabricated detector modules operate from 1.4 to 1.6 GHz and from 1.7 to 2.0 GHz. The lower band of the dualband antenna module around 1.9 GHz (LTE) is independently tuned from the upper band at 5.1 GHz (WLAN). Adaptive matching of the lower band is carried out by a detector module in combination with a tunable matching network, CMOS integrated circuits and FPGA. The achieved 3 dB fractional bandwidth is at least 10.5 %. With the demonstrated concept it is possible to mitigate the effects of environmental impact and frequency dependence.

Chapter 1
Introduction

A new era of RF (Radio Frequency) devices is being expected due to the great advancements in the investigation, design and implementation of communication systems. Particularly, with the advent of the Internet of Things (IoT) and Cooperative Sensor Networks (CSN) to enable smart cities, an ever-increasing amount of data along the frequency spectrum in mobile communications asks for novel solutions to satisfy the exchange of traffic in a dynamic fashion. Yet, current state-of-the-art technologies and devices require a reasonable maturing time to fulfill current and forthcoming communication standards. As a consequence, the study of diverse technologies, not only to develop agile microwave components with reconfigurable characteristics, but also to bring out the proper frequency tuning, requires a major analysis from different fields.

Agile components can be employed for transmission and reception of information in different frequency bands, and thus, to enable multiband and multistandard service. These agile components, combined with Software Defined Radio (SDR) and Cognitive Radio (CR) based platforms, could then offer a promising solution to achieve service convergence in a single device, as well as multifunctionality regarding the frequency of operation.

A reconfigurable architecture is shown in Fig. 1.1. The transmission and reception of signals is performed across a continuous and wide tuning operation of frequencies based on integrated circuits and tunable components. The RF-signal processor together with diverse mixers cover a wide spectrum, while the tunable components are employed to control and to optimize the narrowband signal across a continuous tuning range. Furthermore, a remarkable optimization in the amount of parallel chains can be achieved by using tunable or voltage controllable components. This allows to adapt the same hardware into another service or to adapt any mismatch of the antenna impedance under changing conditions. Thus, the device can be reconfigured to improve its performance and total efficiency by analyzing analog measures, e.g. antenna matching and power consumption, and digital measures, e.g. Bit Error Rate (BER) and Error Vector Magnitude (EVM).

E. Gonzalez Rodriguez, *Reconfigurable Transceiver Architecture for Multiband RF-Frontends*, Smart Sensors, Measurement and Instrumentation 17,
DOI 10.1007/978-3-319-24581-2_1

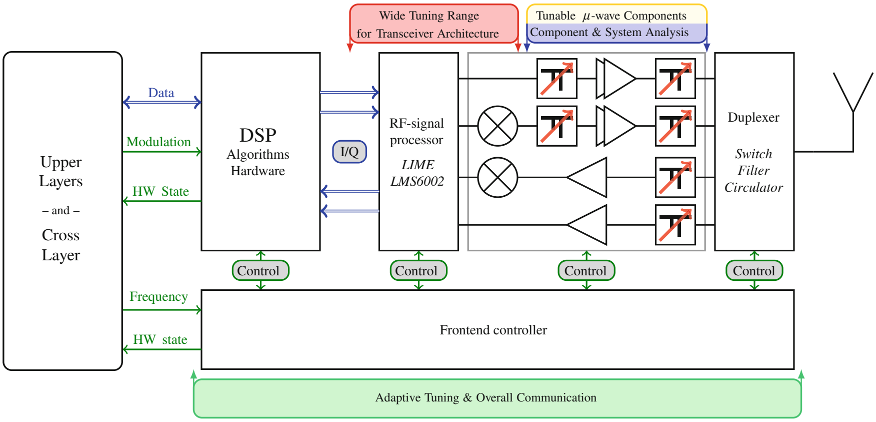

Fig. 1.1 Block diagram of wide tuning multiband and multistandard reconfigurable transceiver with a frontend based on tunable components such as tunable matching networks for antennas and power amplifiers. The frontend is complemented by an RF-signal processor, mixers, algorithms unit for baseband processing and an adaptive control unit to communicate the overall platform

As shown in the prototype platform of Fig. 1.1, the elements of the agile radio can be divided into different cores for the transmitter (Tx) and receiver (Rx) paths: wide frequency range transceiver with tunable RF-Frontend (red area), baseband signal processing and a control unit to communicate with the overall platform (green area). For instance, to perform reconfiguration in terms of frequency, signal bandwidth, modulation scheme and to adaptively control tunable components, such as matching networks (yellow/blue area).

On the transmitter side, different customized mobile standards can be set-up in an adaptive way, e.g. in terms of RF bandwidth and frequency of operation. The main idea is that, after the IQ signals are set-up down in baseband for transmission, they are translated via D/A converters into analog signals. In this way, IQ signals are then amplified and mixed to the desired RF center frequency. Thereafter, the control unit, along with the DC supply voltage, either by look-up tables or adaptive algorithms, selects appropriate bias voltages for the matching networks to carry out an accurate frontend reconfiguration on the amplifier or on the antenna side. This can be performed either for a required power level, defined operation frequency and channel bandwidth.

On the receiver side at the antenna input port, the RF signal is monitored by matching circuit modules, and properly adapted as in the transmitter case in terms of power, frequency and bandwidth. Afterwards, the signal is mixed to be directly downconverted by the signal processor. The resulting IQ signal is then digitalized via A/D converter and processed in the baseband.

Technologies for RF-Components in Reconfigurable Architectures

Implementation of radios entail several aspects to take into account. Performance of these analog and digital measures greatly depend on the type of components' technology or material and their linear behavior at the desired frequency of operation. Moreover, control and integration of components into the overall system represent a critical aspect while the technology is launched onto the market to reach appropriate metrics established by a set of standards and requirements.

New approaches along with functional materials and technologies enable tunable RF devices acting as an important basis for the development of reconfigurable frontends. In the last decade, several competent technologies targeting mobile applications have increased the research effort. Beyond the well-established semiconductor technologies for reconfigurable devices, newly developed technologies have shown specific advantages in their performance and availability. For example, microelectromechanical systems (MEMS), and functional materials such as ferroelectric Barium-Strontium-Titanate (BST) films for low microwave frequency bands ($f < 15\,\text{GHz}$), and liquid crystals for high frequency bands ($f > 10\,\text{GHz}$) [1].

In the last years, different tunable microwave components being integrated in a reconfigurable RF-Frontend have been realized based on the aforementioned technologies, for instance: tunable filters [2–4], power dividers, hybrid couplers [5, 6], matching networks for antennas and power amplifiers [7–13], phase shifters [14–18], and multiband antennas [19–22].

According to the specific characteristics of the components, each technology meets different requirements and specifications. While some candidates offer a good linear performance in terms of power handling, others offer an easier processing method for integration in diverse devices. For example, regarding the tuning speed, while MEMS technology offers tunability in the order of microseconds, semiconductor and ferroelectric reach tuning speeds in the order of nanoseconds or even picoseconds [23, 24].

Currently, BST material for tunable RF components can be processed by using different technologies as thin-film and thick-film. Both technologies provide some remarkable advantages, but also disadvantages. In the case of thin-films, they are considered as a good candidate for integration into reconfigurable transceivers mainly because they can be processed on silicon basis, and due to their low tuning voltage, potentially below 10 V. Furthermore, a large capacitance can be achieved in small footprint due to the efficient utilization of the high dielectric permittivity [25]. Additionally, a very precise control of the film thickness can be achieved, and therefore, resulting in small fabrication tolerances of the capacitance. However, realization of components based on this technology requires several vacuum steps as in semiconductor technology, which yields an increment of production costs [26]. One major drawback of BST thin-films is the excitation of acoustic resonances [27]. Although recent investigations have demonstrated that, by applying a multilayer structure in the fabrication of the varactor, e.g. two layers of the same thickness, excitation of the acoustic resonance can be suppressed [25]. Thus, the series of harmonic resonances essentially constrains the applicable frequency range to discrete narrow bands.

In contrast to thin-films, in thick-films acoustic resonances could also be excited but they are heavily dampened, allowing an application in a continuous wide frequency range without abrupt performance deterioration. On the technical side, such technology enables the realization of distributed components, i.e. they do not require any packaging and soldering as in common surface mounted device (SMD) technology [28]. On the economic side, they are suitable for inclusion in future radios since the production volume of components based on this kind of technology are benefited from scalable printing technology [29]. Among the disadvantages, realization of large capacitances is harder compared to those in current parallel plate topology. Moreover, a major drawback of this kind of technology is that it requires a high tuning voltage because of the relative large gap width between the electrodes. This in turn means, that for most portable devices and mobile applications using tunable components based on this technology, relatively high control voltages in the order of 60–100 V are required. Therefore, compactness can still be a challenge to solve while DC voltage generation is necessary to operate these agile devices.

Throughout this work, special attention is given in ferroelectric thick-film technology. Thus, by analyzing its performance at a component system level, and developing a demonstrator, its potential of usability is shown in scenarios oriented for mobile architectures. For example, by employing tunable matching networks based on ferroelectric varactors to perform an adaptive antenna matching.

Based on the goal to achieve a multiband and multistandard RF-Frontend with a reduced amount of RF chains, a detailed analysis is given throughout different proofs of concepts: to cover all the required frequency spectrum, to ensure or to improve the quality of the narrowband signal employing tunable microwave components, and to adaptively control tunable microwave components used in reconfigurable architectures. It means, smart interfaces and flexible strategies are utilized, such as Cognitive Radio and Software Defined Radio, as well as novel hardware implementations.

Outline

In this work, a study on reconfigurable transceiver architectures is given considering different areas as shown in the diagram of Fig. 1.2. In this chapter, tunable microwave components that enable reconfigurable architectures have been discussed based on different technologies (yellow area). In Chap. 2, the fundamentals and the motivation to enable reconfigurable architectures are reviewed considering current wireless multiband transceivers and required tuning range (red area). An implementation of a wide tuning range reconfigurable transceiver architecture is shown in Chap. 3. This architecture is demonstrated on commercial integrated circuits such as an RF-signal processor and mixer modules. Hence, by employing such components with a wide tuning characteristic, the extended frequency range gives the possibility to sustain wireless communication with up to 7 GHz for transmission and 6 GHz for reception (red area).

Fig. 1.2 Overview of study areas for the realization of a reconfigurable transceiver architecture towards multiband and multistandard functionality proposed in this work

In Chap. 4, a voltage tunable impedance matching network (TMN) is employed based on ferroelectric varactors. Here, a proposed analysis in terms of scattering parameters and group delay variations shows the Bit Error Rate and Error Vector Magnitude performances during tuning. This analysis confirms that, despite an inherent frequency dependence in the phase response of the matching network due to the tunability of the material, ferroelectric varactors stand as a good candidate for inclusion in reconfigurable architectures (blue area).

Chapter 5 extends the practical application of a TMN within a reconfigurable dualband antenna module. This implementation is extended by exploiting a dielectric resonator antenna together with high-voltage integrated circuits (IC). Such ICs are a charge pump and digital-to-analog converter to provide adaptive control of the TMN module. Based on a proposed detector module to monitor the environmental impact and frequency response of the antenna, the overall architecture enables antenna matching self-reconfiguration or spectrum sensing (green area).

Finally in Chap. 6, a summary and outlook of the complete work is given according to current and future trends in wireless communications.

References

1. R. Jakoby, P. Scheele, S. Müller, C. Weil, Nonlinear dielectrics for tunable microwave components, in *MIKON-2004, 15th International Conference on Microwaves, Radar and Wireless Communications* (2004)
2. P. Blondy, D. Peroulis, Handling RF power: The latest advances in RF-MEMS tunable filters. IEEE Microw. Mag. **14**, 24–38 (2013)
3. X. Wang, P. Bao, T. Jackson, M. Lancaster, Tunable microwave filters based on discrete ferroelectric and semiconductor varactors. IET Microw. Antennas Propag. **5**, 776–782 (2010)
4. N. Manh-Tai, W. Yan, E. Horne, Broadband tunable filters using high q passive tunable ics, in *2008 IEEE MTT-S International Microwave Symposium Digest*, June 2008, pp. 951–954
5. E. Lourandakis, M. Schmidt, S. Seitz, R. Weigel, Reduced size frequency agile microwave circuits using ferroelectric thin-film varactors. IEEE Trans. Microw. Theory Tech. **56**, 3093–3099 (2008)
6. E. Fardin, A. Holland, K. Ghorbani, Electronically tunable lumped element 90 deg; hybrid coupler. Electron. Lett. **42**, 353–355 (2006)
7. P. Scheele, F. Goelden, A. Giere, S. Mueller, R. Jakoby, Continuously tunable impedance matching network using ferroelectric varactors, in *2005 IEEE MTT-S International Microwave Symposium Digest*, June 2005, p. 4
8. H. Maune, O. Bengtsson, F. Golden, M. Sazegar, R. Jakoby, W. Heinrich, Tunable RF gan-power transistor implementing impedance matching networks based on BST thick films, in *42nd European Microwave Conference (EuMC)*, 2012
9. A. Tombak, A ferroelectric capacitor based tunable matching network for quad-band cellular power amplifiers. IEEE Trans. Microw. Theory Tech. **55**, 370–375 (2007)
10. M. Schmidt, E. Lourandakis, A. Leidl, S. Seitz, R. Weigel, A comparison of tunable ferroelectric pi- and t-matching networks, in *Microwave Conference, 2007. European*, Oct 2007, pp. 98–101
11. S. Fouladi, F. Domingue, N. Zahirovic, R. Mansour, Distributed mems tunable impedance-matching network based on suspended slow-wave structure fabricated in a standard CMOS technology. IEEE Trans. Microw. Theory Tech. **58**, 1056–1064 (2010)
12. F. Domingue, S. Fouladi, A. Kouki, R. Mansour, Design methodology and optimization of distributed MEMS matching networks for low-microwave-frequency applications. IEEE Trans. Microw. Theory Tech. **57**, 3030–3041 (2009)
13. C. Hoarau, N. Corrao, J.-D. Arnould, P. Ferrari, P. Xavier, Complete design and measurement methodology for a tunable RF impedance-matching network. IEEE Trans. Microw. Theory Tech. **56**, 2620–2627 (2008)
14. O. Karabey, M. Maasch, R. Jakoby, Stable satellite link by liquid crystal based phased array antennas. ATZonline **04**, 46–50 (2012)
15. M. Sazegar, Y. Zheng, H. Maune, C. Damm, X. Zhou, J. Binder, R. Jakoby, Low-cost phased-array antenna using compact tunable phase shifters based on ferroelectric ceramics. IEEE Trans. Microw. Theory Tech. **59**, 1265–1273 (2011)
16. A. Gaebler, F. Goelden, A. Manabe, M. Goebel, S. Mueller, and R. Jakoby, Investigation of high performance transmission line phase shifters based on liquid crystal, in *European Microwave Conference, EuMC 2009*, Sept 2009, pp. 594–597

17. S. Gao, A. Sambell, S.-S. Zhong, Polarization-agile antennas. IEEE Antennas Propag. Mag. **48**, 28–37 (2006)
18. M. Nikfalazar, M. Sazegar, Y. Zheng, A. Wiens, R. Jakoby, A. Friederich, C. Kohler, J. Binder, Compact tunable phase shifter based on inkjet printed bst thick-films for phased-array application, in *2013 European Microwave Conference (EuMC)*, Oct 2013, pp. 432–435
19. P. Bahramzy, O. Jagielski, S. Svendsen, G. Pedersen, Compact agile antenna concept utilizing reconfigurable front end for wireless communications. IEEE Trans. Antennas Propag. **62**, 4554–4563 (2014)
20. M. Kehn, O. Quevedo-Teruel, E. Rajo-Iglesias, Reconfigurable loaded planar inverted-f antenna using varactor diodes. IEEE Antennas Wirel. Propag. Lett. **10**, 466–468 (2011)
21. Y. Zheng, A. Hristov, A. Giere, R. Jakoby, Suppression of harmonic radiation of tunable planar inverted-f antenna by ferroelectric varactor loading, in *2008 IEEE MTT-S International Microwave Symposium Digest*, June 2008, pp. 959–962
22. Y. Zheng, M. Sazegar, H. Maune, M. Arshad, R. Jakoby, Compact tunable dual-channel antenna based on ferroelectric ceramics. Electron. Lett. **47**, 897–898 (2011)
23. C. Siegel, Z. V., C. von Wächter, B. Schönlinner, U. Prechtel, H. Schumacher, Switching speed analysis of low complexity RF-MEMS switches, in *IEEE German Microwave Conference*, March 2006
24. C. Huang, K. Buisman, L. Nanver, P. Zampardi, L. Larson, L. De Vreede, "Design concepts for semiconductor based ultra-linear varactor circuits (invited), in *2010 IEEE Bipolar/BiCMOS Circuits and Technology Meeting (BCTM)*, Oct 2010 pp. 204–211
25. Y. Zheng, *Tunable Multiband Ferroelectric Devices for Reconfigurable RF-Frontends* (Springer, Berlin, 2013)
26. M.H. Francombe, Historical perspective of oriented and epitaxial thin films. J. Vac. Sci. Tech. A: Vac. Surf. Films **12**, 928–935 (1994)
27. S. Gevorgian, A. Vorobiev, T. Lewin, Dc field and temperature dependent acoustic resonances in parallel-plate capacitors based on srtio3 and ba0.25sr0.75tio3 films: Experiment and modeling. J. Appl. Phys. **99**, 12 (2006)
28. S. Gevorgian, *Ferroelectrics in Microwave Devices, Circuits and Systems* (Springer, Berlin, 2009)
29. H. Maune, *Design und Optimierung hochlinearer ferroelektrischer Varaktoren für steuerbare Hochfrequenz-Leistungsverstärker*. Ph.D thesis, Technische Universität Darmstadt, 2011

Chapter 2
Fundamentals

Reconfigurability, a concept of utmost importance in communication systems has been foreseen over two decades ago [1, 2]. Reconfiguration of a radio to achieve higher hardware performance is turning to be not only a requirement, but also a necessity in current radio architectures for services and portable devices in the frequency spectrum below 6 GHz. Advances in software and hardware development have been targeting this idea, and thus, leading to an evolution for modern radio architectures relaying in key concepts, such as Software Defined Radio and Cognitive Radio.

Ideally, a Software Defined Radio has the ability to accommodate an RF-band across a spectrum determined by the user or the platform itself, i.e. to perform a transition and/or coexistence of frequencies considering different air interfaces [3, 4]. Moreover, by accompanying the radio with the use of Cognitive Radio techniques,[1] a certain level of recognition is provided based on the observation or sensing of the environment [5]. That means, a reconfiguration of the communication platform to exploit the available resources is performed.

The amount of circuitry present in a device is continuously optimized and reduced. For instance, according to the road map in semiconductor technology, Moore's Law for integrated circuits in nanometer ranges [6] and carbon nanotubes [7, 8] are considered as an alternative to silicon technology in future microelectronics. Thus, an ambitious revolution is proposed for communication standards and protocols. Nevertheless, these standards and protocols are barely in process to be fulfilled by current devices in mobile systems. For example, IMT-Advanced for 4G [9], and the not yet standardized 5G [10]. As a consequence, these upcoming communications require hardware architectures that are still limited by the complexity and high energy consumption that a multiband and multistandard device represents.

---

[1] For example, programming of baseband algorithms that reconfigure the overall communication architecture according to the capabilities of the employed hardware in the RF-Frontend.

E. Gonzalez Rodriguez, *Reconfigurable Transceiver Architecture for Multiband RF-Frontends*, Smart Sensors, Measurement and Instrumentation 17,
DOI 10.1007/978-3-319-24581-2_2

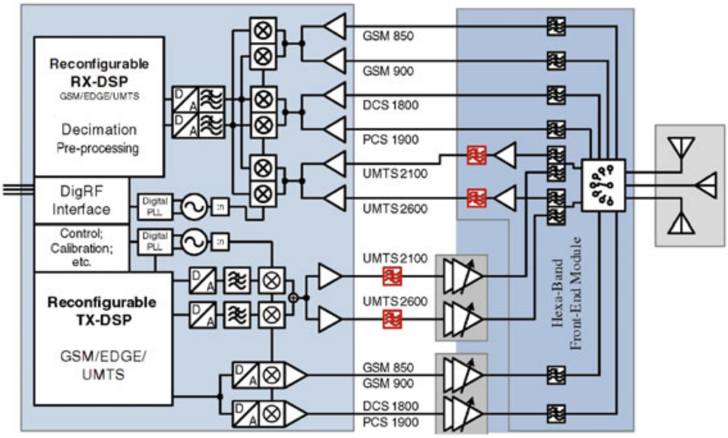

Fig. 2.1 Transmitter and receiver chains of a state-of-the-art multiband and multistandard RF-Frontend with parallelized RF components [11]. The radio is conformed by multiple: filters, amplifiers (PA and LNA), switch/duplexers, and antennas

To exemplify this issue, transmitter and receiver chains of a state-of-the-art multiband and multistandard RF-Frontend supporting 2G and 3G technology standards are shown in Fig. 2.1. Due to the increase in the demand of services, RF components like filters and duplexers are present in large amount of elements in the frontend of the device. Realization is carried out by including, for almost every service, a chain of RF components, resulting in an increment of circuitry, hardware complexity and power consumption.

Thereby, a reduction of parallel chains is fundamental since new standards and more services for communication constantly appear, and therefore, are required to coexist within the same architecture. Hence, if a decrease in the employed circuitry is realized, an improvement of the energy consumption can be obtained while the device is enabled to offer the required multifunctionality covering diverse services.

Considering future trends in communications, reconfigurable frontends, mainly, have to meet specifications such as:

- overall wide tuning range of the transceiver for global functionality,
- control of harmonic rejection due to extended bandwidth,
- required SNR level while allocating a defined channel,
- full-duplex operation for simultaneous transmission and reception,
- compactness of multiband antennas,
- overall low power consumption.

As a consequence of this, reconfigurability plays a key role to enhance the usage and compatibility of a device or user equipment. Hence, this can result in a wide tuning range of the transceiver by means of the components' tunability.

2.1 RF-Spectrum and Requirements for Mobile Communications

During the last decade, the way to communicate with a mobile device has dramatically evolved. The trend is that a mobile phone will perform many more tasks than just a telephone call, e.g. wireless network access considering diverse scenarios (PAN, LAN, MAN, WAN), access to global navigation systems (GNSS), mobile-TV (DVB-NGH), contactless payment and identification using Radio Frequency Identification (RFID). For this reason, the notable augment in hardware to provide signal diversity and global roaming functionality, e.g. MIMO (Multiple Input Multiple Output) applications with multiple antenna links, demands for multiband and multistandard operation [12]. Technologies using present and future communication standards such as LTE, UMTS, GSM, WLAN, WiMAX, NFC, among others, are desired to be all packed into the same architecture rather than using a different device or RF module for each standard [13, 14]. The frequency spectrum allocation of different categorized services typically used in current mobile and portable devices is shown in Fig. 2.2. The used spectrum is covered mainly up to 4 GHz, and from 5 to 6 GHz, while white spaces and unlicensed frequencies are located in the low frequency range below 1 GHz, around 3.2 GHz, and between 4 and 5 GHz.

Thus, if a device aims for global access, the communication platform requires to increase its reconfigurability and flexibility [15]. In other words, modern devices like smartphones or tablets still need to be improved in terms of adaptability and efficiency. That means, a high quality of service to cope with identified constraints such as battery lifetime, alltime online connectivity, dropped calls, and packet loss [16] is required.

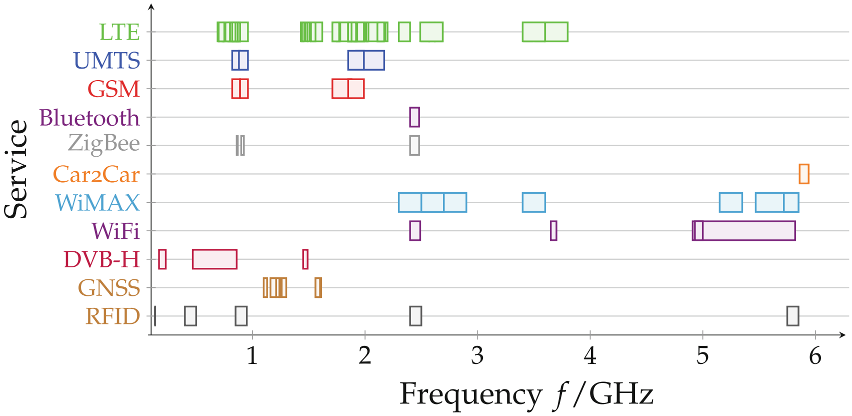

Fig. 2.2 Frequency spectrum allocation of current and future services for global mobile systems and portable devices [17–25]

2.2 Future Mobile and Cognitive Radio Applications

Dynamic and adaptable communication approaches are strongly required with the steady growth of services and applications for portable devices. In that way, an agile reconfiguration should take into account every layer of a typical communication system, i.e. from the application layer to the physical layer [26]. Nevertheless, while a clear road map for protocols and standards has been developed, at the physical layer, the RF-Frontend of a device reaches a bottleneck. This limitation, for example, avoids that forthcoming demands are satisfied according to the technological needs in today's urban areas [27].

Increasing interest towards design and implementation of smart cities and Internet of Things (IoT) has emerged in recent years. The idea of having such a city consists in the employment of technology and advanced systems so that daily life happens in a more efficient and functional way. That means, the integration of physical infrastructures with the digital technologies is what significantly contributes to improve the smartness of a city [28]. An advantage of this, is that a proper utilization of the available technology can greatly improve the interaction of users with their surrounding environment [29, 30]. In this way, a critical demand to face involves the development of high quality devices and the compatibility between them to achieve a smart air interface, i.e. an interface that constantly adapts the necessities or requirements of the user with its environment. Thus, integration of distributed sensors, networks and portable devices like mobile phones, PDAs, and tablets, is required to develop the convergence of the information and communication technologies into global service devices [31].

Based on the general concept to transform conventional communication into an adaptive and energy efficient interoperation of resources, the exchange of data by means of Cooperative Sensor Networks represents a promising attempt to turn a common city into a smart city. CSN are based on a group of interconnected sensors that assist in communication sharing data within a certain area, e.g. to obtain high energy savings of a wireless node [32]. Implementation of embedded system applications connected by cooperative computing provides a flexible solution for sensor networks [33]. For example, to enable mobile cloud computing, an emerging technology that improves the quality of mobile services shares the radio and computing resources [34, 35]. Furthermore, such networks have the characteristic to work dynamically in order to carry out an updated flow of information, either to the end-user or just to another node assigned to perform a predefined task. Thereby, this wireless coordination of sensing devices can perform tasks like monitoring, tracking, warning and surveillance [36].

Strategically located distributed nodes, which continuously sense the environment, are required to be linked and to supply assorted categorized information to the user. Moreover, a user device needs to fulfill demands such as high reliability, mobility and functionality to offer a cost-effective performance of services [37]. That is, the development of smart cities require multiband and multistandard, or even band-less and/or standard-less devices to achieve an efficient communication of the network

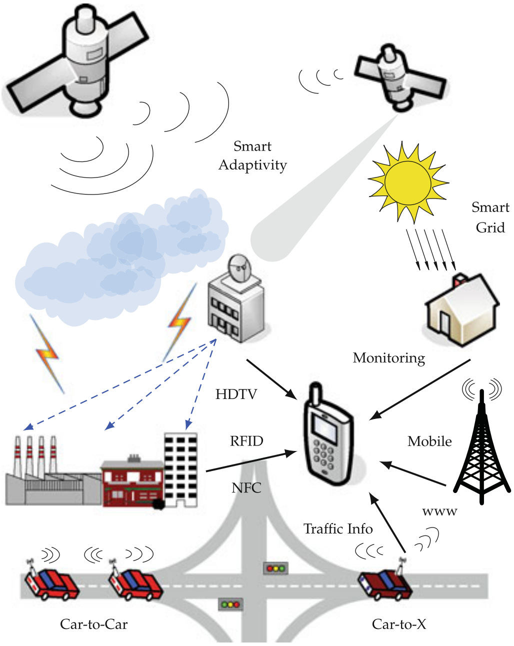

Fig. 2.3 Smart city with interoperation of services and convergence of diverse applications in a multiband and multistandard environment

elements, e.g. between the different nodes, services, and sources of information. Nevertheless, as a result of utilizing different RF modules to handle different services, a lack of a global, energy efficient, and adaptive transmission/reception of information in a device of current architectures is present at the user side [38, 39]. This means, that the current solution is to employ a single hardware module per service if a service is intended to be used [40]. Hence, effective interconnection of living areas between buildings, supermarkets, houses, offices, shopping centers, streets, cars, and parking places, among others is becoming a significant challenge to be solved [41]. Furthermore, other factors like interference and bandwidth constraints will emerge due to the new allocation of services or to the reuse of the frequency spectrum [42].

A smart allocation of frequencies for upcoming applications and services, while supporting current technologies is becoming a particular major issue in today's hardware development [43]. To exemplify this scenario, in Fig. 2.3 possible services and applications within a sensed urban area of a smart city are shown. Alltime online mobile phones, Machine-to-Machine communication (M2M), Car-to-Car communication (C2C & C2X), and smart management of energy in urban areas are just a few examples of on-going developing features. These features demand for the evolution of existing cities, with new kind of architectures, to handle different sources of information within the same device.

Machine-to-Machine Communications

A concept that has been maturing during the last decade is Machine-to-Machine communication (M2M) [44, 45]. This essential part of a smart city has the task to communicate wired or wireless devices which belong to a determined system, or commonly also known as cloud. At another size level compared to a smart city but in a similar fashion, M2M aims to share, improve and monitor, among other characteristics, defined tasks either by the user or by a whole community. For instance, to enable this type of technology using cellular infrastructures, the Third Generation Partnership Project (3GPP) provides machine-type communication when it is used over LTE technology. One characteristic is that a cognitive M2M communication is expected to provide a good approach for dealing with excessive traffic in the network [46].

Here, the management of diverse devices utilizing a variety of mobile technologies, i.e. protocols and standards, represents the use of different kind of devices to realize a defined task. Consequently, the most promising solution is the employment of reconfigurable architectures that are able to handle multifunctionality. For example, by using the minimum amount of hardware to provide a maximum number of services.

Car-to-Car Communications

In a more specific area called Intelligent Transport Systems (ITS), a wireless concept known as Car-to-Car (C2C) communication is arising [47, 48]. It aims at easing road travelling as well as increasing road safety and traffic efficiency. Novelty in the network layer for the exchange of information is established together with the operation at 5.9 GHz defined in the physical layer. Therefore, to provide proper functionality at this frequency band in terms of RF hardware, an increment in the number of architecture elements is expected according to current approaches. Specifically, in the case of components such as antenna, filter, amplifier, and matching network, to enable this mobile technology. This means, that when this technology is adapted into a vehicle, compatibility with other technologies have to be improved in a cost-effective way [49], e.g. to avoid possible sources of interference, and to keep compactness in the RF-Frontend of the portable device.

On top of the described novelty in the concepts of previous examples, M2M and C2C, there is one common denominator which can be translated as an unavoidable increase of hardware. That is, on the one hand, the present solution is to develop a single device for each service to make use of each of these latest features, or to include multiple hardware modules into the current architecture. On the other hand, however, a reconfigurable architecture can overcome the increase of RF modules and hardware complexity.

Wireless Multiband Transceivers

Different approaches to face the challenge of an efficient spectrum management from the hardware point of view are emerging, e.g. at the antenna side of a reconfigurable RF-Frontend [50, 51], or in recent years by implementing fully integrated CMOS based transceivers for SDR applications [52].

A summary of current multiband RF chip transceivers is shown in Table 2.1. These RF-signal processors are used in deployments compliant with standards and technologies employed in nowadays mobile communication systems. Furthermore, this

Table 2.1 Performance of different commercial ICs RF transceivers

	LMS6002D	LMS7002D	AD9361
Communication mode	SISO	MIMO (2 × 2)	MIMO (2 × 2)
RF frequency range	0.3 ∼ 3.8 GHz	0.05 ∼ 3.8 GHz	0.07 ∼ 6 GHz
Baseband BW	0.7 . . . 14 MHz	0.1 . . . 54 MHz	0.2 . . . 56 MHz
Supply voltage	1.8 V	1.8 V	1.3 V
Transmitter			
Maximum output power	<+6 dBm	<+19 dBm	<+9.5 dBm
Gain control	56 dB	70 dB	90 dB
Gain control step	1 dB	1 dB	0.25 dB
D/A converter	12 bits	12 bits	10 bits
LO leakage	<−50 dBc	<−50 dBc	<−50 dBc
DC current	280 mA	<200 mA (2 Tx)	<820 mA (2 Tx)
	@+6 dBm	@−7 dBm	@+7 dBm
Receiver			
Gain control	<61 dB	<70 dB	<75 dB
Gain control step	3 dB	1 dB	1 dB
Noise figure	<10 dB	<3.6 dB	<3.8 dB
IIP3	−1 dBm	3 dBm	>−18 dBm
A/D converter	12 bits	12 bits	12 bits
DC current	220 mA	280 mA (2 Rx)	<445 mA (2 Rx)

This comparison takes different general parameters into account for the signal processors, considering their transmitter and receiver characteristics [53, 54]

kind of transceivers can make use of its flexibility so that additional implementations of reconfigurable transceivers based on CR and SDR techniques can be enabled. Three different signal processors are compared: LMS6002D and LMS7002D from Lime Microsystems [53], and AD9361 [54] from Analog Devices. While the first chip transceiver supports only SISO (Single Input Single Output) communication, the last two ICs are MIMO enabled.

At the time of realization of this work, only the RF-signal processor LMS6002D was commercially available, and therefore, it was taken into account for the development of hardware demonstrations. However, these demonstrations are fully compatible with the current version of the IC LMS7002D.

To summarize this section it should be mentioned that different approaches, such as the combination of SDR and CR techniques, and technologies can enable agile radios depending on the necessities and constraints of the design itself. For example, frequency of operation, required tunability and power handling. Furthermore, special attention to integrate the RF-Frontend in the transceiver should be given based on the hardware control of all RF components to optimize the narrowband signal at the desired frequency. In this way, the best performance in the overall architecture can be guaranteed. That is, the combination of wide tuning reconfigurable transceivers, as well as state-of-the-art material technologies that enable microwave components and integrated circuits, represent an attractive solution to cover the complete spectrum where allocated mobile services, current and future portable applications form part of the ever-increasing smart interfaces.

References

1. J. Mitola, Software radios: survey, critical evaluation and future directions. IEEE Aerosp. Electron Syst. Mag. **8**, 25–36 (1993)
2. F. Jondral, A. Wiesler, R. Machauer, A software defined radio structure for 2nd and 3rd generation mobile communications standards, in *2000 IEEE Sixth International Symposium on Spread Spectrum Techniques and Applications*, 2000
3. J. Mitola, Cognitive radio an integrated agent architecture for software defined radio, PhD thesis, (Royal Institute of Technology (KTH), 2000)
4. A. Margulies, J. Mitola, Software defined radios: a technical challenge and a migration strategy, in *Proceedings of the IEEE 5th International Symposium on Spread Spectrum Techniques and Applications*, vol. 2 September (1998), pp. 551–556
5. J. Mitola, G. Maguire, Cognitive radio: making software radios more personal. IEEE Pers. Commun. **6**, 13–18 (1999)
6. R. Courtland, The end of the shrink. IEEE Spectr. **50**, 26–29 (2013)
7. C. Vu, Made in ibm labs: researchers demonstrate initial steps toward commercial fabrication of carbon nanotubes as a successor to silicon. Online, Oct 2012. Accessed Feb 2014
8. H. Park, A. Afzali, S. Han, G. Tulevski, A. Franklin, J. Tersoff, J. Hannon, W. Haensch, High-density integration of carbon nanotubes via chemical self-assembly. Nat. Nanotechnol. **7**, 787–791 (2012)
9. 3GPP tr 36.942 version 8.2.0 release 8. LTE. evolved universal terrestrial radio access (E-UTRA). radio frequency (RF) system scenarios, 2009
10. Mobile and wireless communications Enablers for the Twenty-twenty Information Society, Metis, 2014
11. S. Heinen R. Wunderlich, High dynamic range rf frontends from multiband multistandard to cognitive radio, in *Semiconductor Conference Dresden (SCD)*, 2011
12. T. Zahariadis, K. Vaxevanakis, C. Tsantilas, N. Zervos, N. Nikolaou, Global roaming in next-generation networks. IEEE Commun. Mag. **40**, 145–151 (2002)
13. H. Okazaki, A. Fukuda, K. Kawai, T. Furuta, S. Narahashi, Mems-based reconfigurable rf front-end architecture for future band-free mobile terminals, in *European Microwave Conference* (2007)
14. I. Nam, H. Moon, J.-D. Bae, B.-H. Park, A wideband cmos rf front-end using ac-coupled current mirrored technique for multiband multistandard mobile tv tuners. IEEE Microw. Wirel. Compon. Lett **17**, 739–741 (2007)
15. I. Cha, Y. Shah, A. Schmidt, A. Leicher, M. Meyerstein, Trust in m2m communication. IEEE Veh. Technol. Mag. **4**, 69–75 (2009)
16. M. Cinque, D. Cotroneo, Z. Kalbarczyk, R. Iyer, How do mobile phones fail? A failure data analysis of symbian os smart phones, in *37th Annual IEEE/IFIP International Conference on Dependable Systems and Networks, 2007. DSN '07*, pp. 585–594, June 2007
17. 3GPP ts 34.121-1 version 9.3.0 release 9. Universal mobile telecommunications system (UMTS); User Equipment (UE) conformance specification; radio transmission and reception (FDD); part 1: Conformance specification. etsi ts 134 121-1 v9.3.0, 2011
18. Lte; evolved universal terrestrial radio access (e-utra); user equipment (ue) conformance specification; radio transmission and reception; part 1: Conformance testing (3gpp ts 36.521-1 version 10.4.0 release 10). etsi ts 136 521-1 v10.4.0 (2013-02), 2013
19. 3rd generation partnership project; technical specification group gsm/edge radio access network; radio transmission and reception (release 11). 3gpp ts 45.005 v11.2.0 (2012-11), 2012

20. Digital video broadcasting (DVB); DVB-H implementation guidelines. ETSI TR 102 377 v1.3.1 (2009-03), 2009
21. IEEE std 802.11-2012. IEEE standard for information technology-telecommunications and information exchange between systems local and metropolitan area networks-specific requirements. part 11: Wireless lan medium access control (mac) and physical layer (phy) specifications, 2012
22. IEEE std 802.15.1-2005. IEEE standard for information technology-telecommunications and information exchange between systems—local and metropolitan area networks—specific requirements part 15.1: Wireless medium access control (MAC) and physical layer (PHY) specifications for wireless personal area networks (WPANs) (2005)
23. IEEE std 802.15.4-2006. IEEE standard for local and metropolitan area networks-part 15.4: Low-rate wireless personal area networks (lr-wpans) (2006)
24. IEEE std 802.16.2-2004. IEEE recommended practice for local and metropolitan area networks coexistence of fixed broadband wireless access systems (2004)
25. B. Eissfeller, G. Ameres, V. Kropp, D. Sanroma, Performance of gps, glonass and galileo, in *Photogrammetric Week*, 2007
26. A. Tanenbaum, *Computer Networks* (Pearson Education, New Jersey, 2003)
27. V. Nguyen, F. Villain, Y. Le Guillou, Cognitive radio RF: Overview and challenges. VLSI Des. **2**, 1–12 (2012)
28. D.M. Gann, M. Dodgson, D. Bhardwaj, Physical-digital integration in city infrastructure. IBM J. Res. Dev. **55**, 8:1–8:10 (2011)
29. B. Morvaj, L. Lugaric, S. Krajcar, Demonstrating smart buildings and smart grid features in a smart energy city, in *Proceedings of the 2011 3rd International Youth Conference on Energetics (IYCE)* (2011)
30. L. Lugaric, S. Krajcar, Z. Simic, Smart city platform for emergent phenomena power system testbed simulator, in *Innovative Smart Grid Technologies Conference Europe (ISGT Europe), 2010 IEEE PES* (2010)
31. R. Singh, P. Bhargava, S. Kain, Smart phones and interactive reports leave traffic in the rearview mirror. IEEE Potentials **27**, 33–38 (2008)
32. M. Elhawary, Z. Haas, Energy-efficient protocol for cooperative networks. IEEE/ACM Trans. Netw. **19**, 561–574 (2011)
33. C. Borcea, D. Iyer, P. Kang, A. Saxena, L. Iftode, Cooperative computing for distributed embedded systems, in *Proceedings of 22nd International Conference on Distributed Computing Systems* (2002)
34. R. Kaewpuang, D. Niyato, P. Wang, E. Hossain, A framework for cooperative resource management in mobile cloud computing. IEEE J. Sel. Areas Commun. **31**, 2685–2700 (2013)
35. M. Milosavljevic, S. Sofianos, P. Kourtessis, J. Senior, Self-organized cooperative 5g rans with intelligent optical backhauls for mobile cloud computing, in *2013 IEEE International Conference on Communications Workshops (ICC)*, pp. 900–904, June 2013
36. C. Cassandras, W. Li, Sensor networks and cooperative control. Eur. J. Control **11**(4–5), 436–463 (2005)
37. J. Wang, Z. Cheng, I. Nishiyama, Y. Zhou, Design of a safety confirmation system integrating wireless sensor network and smart phones for disaster, in *2012 IEEE 6th International Symposium on Embedded Multicore Socs (MCSoC)*, pp. 139–143, September 2012
38. M. Kennedy, A. Ksentini, Y. Hadjadj-Aoul, G. Muntean, Adaptive energy optimization in multimedia-centric wireless devices: A survey. Communications Surveys Tutorials, IEEE **15**, 768–786 (2013)
39. C. Schwartz, F. Lehrieder, F. Wamser, T. Hossfeld, P. Tran-Gia, Smart-phone energy consumption vs. 3g signaling load: The influence of application traffic patterns, in *2013 24th Tyrrhenian International Workshop on Digital Communications—Green ICT (TIWDC)*, pp. 1–6, September 2013
40. H. Jiang, D. Zhang, Y. Gang, Rf front end design for receiver of smart gsm mobile phone, in *2010 6th International Conference on Wireless Communications Networking and Mobile Computing (WiCOM)*, pp. 1–5, September 2010

41. M. Naphade, G. Banavar, C. Harrison, J. Paraszczak, R. Morris, Smarter cities and their innovation challenges. IEEE Comput. Soc. **44**, 32–39 (2011)
42. L. Sciacca, R. Evans, Cooperative sensor networks with bandwidth constraints, in SPIE 4741. Battlespace Digitization and Network-Centric Warfare **II** , 192 (2002)
43. S. Del Barrio, M. Pelosi, G. Pedersen, On the efficiency of frequency reconfigurable high-q antennas for 4g standards. Electron. Lett. **48**, 982–983 (2012)
44. A. Osseiran, F. Boccardi, V. Braun, K. Kusume, P. Marsch, M. Maternia, O. Queseth, M. Schellmann, H. Schotten, H. Taoka, H. Tullberg, M. Uusitalo, B. Timus, M. Fallgren, Scenarios for 5g mobile and wireless communications: the vision of the metis project. IEEE Commun. Mag. **52**, 26–35 (2014)
45. A. Lo, Y. Law, M. Jacobsson, A cellular-centric service architecture for machine-to-machine (m2m) communications. IEEE Wirel. Commun. **20**, 143–151 (2013)
46. H. kwan Lee, D.M. Kim, Y. Hwang, S.M. Yu, S.-L. Kim, Feasibility of cognitive machine-to-machine communication using cellular bands. IEEE Wirel. Commun. **20**, 97–103 (2013)
47. Car 2 car communication consortium. http://www.car-to-car.org, Accessed Aug 2014
48. Safe intelligent mobility—test field germany (sim^{TD}). http://www.simtd.de, Accessed Aug 2014
49. K. Borgeest, Practical papers, articles and application notes: Emc aspects of car communication systems. IEEE Electromagn. Compat. Mag. **1**, 35–41 (2012)
50. P. Hall, P. Gardner, J. Kelly, E. Ebrahimi, M. Hamid, F. Ghanem, F. Herraiz-Martinez, D. Segovia-Vargas, Reconfigurable antenna challenges for future radio systems, in *IEEE European Conference on Antennas and Propagation* (2009)
51. Y. Tawk, J. Costantine, C. Christodolou, Cognitive-radio and antenna functionalities: A tutorial. IEEE Antennas Propag. Mag. **56**(01), 231–243 (2014)
52. J. Craninckx, M. Liu, D. Hauspie, V. Giannini, T. Kim, J. Lee, M. Libois, B. Debaille, C. Soens, M. Ingels, A. Baschirotto, J. Van Driessche, L. Van der Perre, P. Vanbekbergen, A fully reconfigurable software-defined radio transceiver in 0.13um cmos, in *IEEE Solid-State Circuits Conference* (2007)
53. Lime microsystems ultra flexible FPRF solutions, 2014. http://www.limemicro.com/, Accessed Aug 2014
54. Analog Devices AD9361 RF Agile Transceiver Datasheet (2013)

Chapter 3
Reconfigurable Transceiver Architecture with Wide Tuning Range

As shown in the previous chapter, the innovation in hardware interfaces that enables interconnection between different nodes, plays an important role in future developments to provide communication in the most efficient way [1]. Depending on the adaptability of the node, a complete network reflects how functional and effective it can behave. In this case, a node is namely a user terminal or any object capable of receiving and transmitting information to handle diverse sources of information. Thus, such adaptability bears in mind the frequency of operation, energy consumption, data rate, and connectivity between the nodes. Hence, resulting in a so called ubiquitous city, a smart city where every urban system and resource makes its data available for monitoring, analysis, and control [2].

3.1 Concept and Tuning Range

To overcome aforementioned requirements, the objective is to conceive a communication platform able to cover the spectrum of frequencies of at least up to 6 GHz, where services are typically allocated for mobile communications. Furthermore, the platform should handle a reduced amount of parallel RF modules to minimize the required supplied energy. Finally, it should offer a flexible hardware reconfiguration of the operation frequency for transmission and reception of data, as well as for further digital signal processing. For example, tasks like sensing of the occupied spectrum can be performed by monitoring both, the baseband and the RF part. In this way, a spectrum management can be realized in terms of frequency allocation and bandwidth efficiency. Therefore, in this chapter, a demonstrator is developed to enable transmission and reception of signals with a reconfigurable architecture including a reduced amount of RF chains.

E. Gonzalez Rodriguez, *Reconfigurable Transceiver Architecture for Multiband RF-Frontends*, Smart Sensors, Measurement and Instrumentation 17,
DOI 10.1007/978-3-319-24581-2_3

Considering the aforementioned challenges concerning the implementation of a reconfigurable transceiver with multiband and multistandard functionality, a promising architecture is proposed, implemented, investigated and compared to current architectures. Based on state-of-the-art components, e.g. RF-signal processor, mixers, filters, amplifiers and circulator, integration of the reconfigurable frontend allows to attain a continuous tuning range from 0.3 GHz up to more than 7 GHz. As a result of the wide frequency range, typical services for portable devices, as shown in the spectrum of Fig. 2.2, can be covered within the same architecture. Apart from the RF-signal processor and mixing stage, the reconfigurable frontend is complemented by an ultrawideband monopole antenna, switches, amplification stage and filters. A circulator is used to isolate transmitted and received signals, hence, bidirectional communication is introduced at the input port of a single antenna.

3.1.1 RF-Signal Processor and Wideband Synthesizer

To solve the requirement of transmission and reception of signals across a wide tuning range of frequencies with extended tuning range, a proposed reconfigurable transceiver architecture, considering the architecture in Fig. 1.1, is proposed in Fig. 3.1. The prototype for technology evaluation is based on the LMS6002D processor from the manufacturer Lime Microsystems [3] and the RFFC5071A mixer module from the manufacturer RFMD [4]. The mixer module is employed to extend the frequency tuning range of the Tx and Rx paths of the RF-signal processor, thus, covering more than the minimum targeted frequency operation range of 6 GHz. Thereafter, the Tx and Rx paths are complemented by components with wideband frequency characteristic.

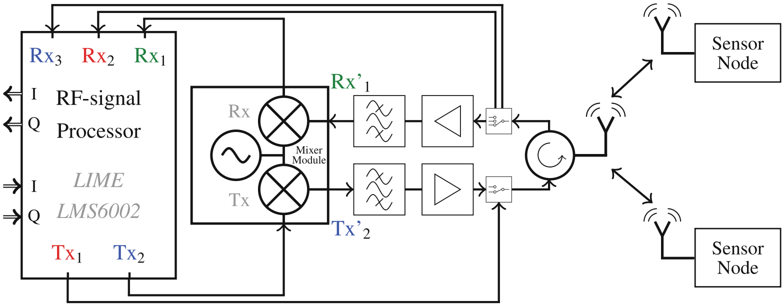

Fig. 3.1 Reconfigurable wideband transceiver chain with extended continuous frequency range towards multiband and multistandard functionality based on the RF-signal processor LMS6002D and mixer module RFFC5071A

RF-Signal Processor

The RF-signal processor LMS6002D [5] includes a continuous transmission and reception from 0.3 to 3.8 GHz with a signal bandwidth of up to 28 MHz.

The integrated signal path tailored for commercial communication services as well as for SDR and CR applications, comprises different working bands. These bands employ LNA, power amplifier, Tx/Rx mixers and filters, gain control, and power control, along with a digital baseband interface linked by means of 12-bit D/A and A/D converters to monitor the IQ signals.

Reconfiguration of the RF-signal processor across the complete band in terms of power, frequency and signal bandwidth can be enabled from a control unit via backend software, e.g. with a serial port interface. To enable the transmission and reception of signals, the entire path can be extended from the baseband up to the RF part. On the baseband part, e.g. processed by an external unit such as FPGA (Field-Programmable Gate Array), and on the RF part by including external components such as filters, matching networks, mixers, amplifiers, a circulator, and antennas.

In Fig. 3.2, the integrated circuit LMS6002D is embedded within a board for evaluation by including two RF ports for transmission and three ports for reception matched at different frequency bands. Furtheremore, it contains USB port for connection with a backend software, digital Tx/Rx 12-bit I/O, baseband board connector, and analog IQ pins for monitoring of the Tx/Rx signals.

One of the main advantages of the RF-signal processor is that it integrates different input/output ports for transmission and reception within the complete signal path. In the Tx part, two bands assigned in two RF ports can be used for evaluation along its complete bandwidth. For the Rx part, three different bands are allocated, each one with an independent RF port.

The Tx and Rx frequency bands are configured to provide a good performance in terms of amplitude and harmonics control as follows: (a) Band Tx$_1$ and band Tx$_2$, both transmitting from 0.3 to 3.8 GHz, and (b) Band Rx$_1$ receiving from 0.3 to

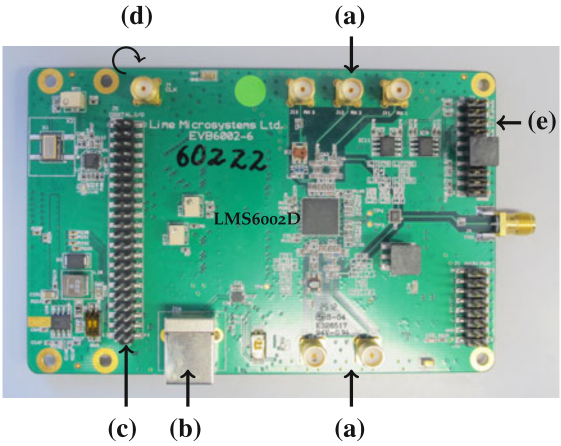

Fig. 3.2 Lime board with embedded RF-signal processor LMS6002D including mainly: (**a**) two RF ports for Tx and three RF ports for Rx; (**b**) USB connector; (**c**) digital Tx/Rx 12-bit I/O; (**d**) baseband board connector (from *bottom view*); (**e**) analog IQ pins for Tx/Rx signal monitoring

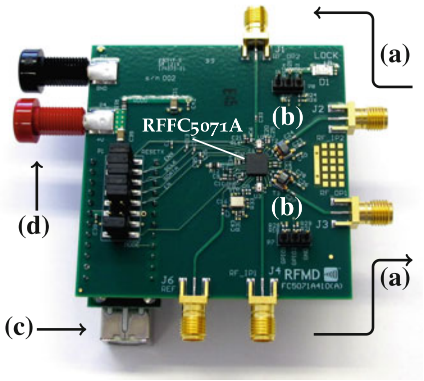

Fig. 3.3 Evaluation board with two mixers embedded in the RFFC5071A integrated circuit. The mixer module includes mainly: (**a**) $\mathrm{RF_{in}}$ and $\mathrm{RF_{out}}$ ports of both mixers. (**b**) Matching circuits at input/outputs of the IC for broadband matching. (**c**) USB interface for control via backend software. (**d**) Power supply with maximum 3.3 V

2.8 GHz, band $\mathrm{Rx_2}$ receiving from 1.5 to 3.8 GHz and band $\mathrm{Rx_3}$ receiving from 0.3 to 3.0 GHz.

Wideband Synthesizer with Integrated Mixers

In a similar fashion to the RF-signal processor, the wideband synthesizer with integrated mixers can be enabled also via backend software, e.g. USB/SPI interface [6]. Among the most important characteristics of this module is the wide tuning frequency range of the local oscillator (LO) between 85 MHz and 4.2 GHz. The LO frequency can be selected at the same operation frequency for Tx and Rx, resulting in the possibility to employ half-duplex or duplex communication in upconversion and downconversion mode with the RF-signal processor ports. Thus, the generated LO signal with f_{LO} is routed to the integrated mixers used for downconversion up to 6.3 GHz, and for upconversion up to a frequency range of at least 7.3 GHz.

In Fig. 3.3, the integrated circuit RFFC5071A is embedded within a board for evaluation by including two mixers, a fractional phase-locked loop (PLL) with voltage controlled oscillator, USB connector. Thus, one mixer is used for Tx upconversion and the other for Rx downconversion.

3.1.2 Extended Tuning Range and Transceiver Operation Modes

A continuous transmission and reception of signals across the complete frequency range is enabled. Thus, the LO frequency is selected according to the difference between lower-boundary frequency and upper-boundary frequency of the RF-signal processor. This difference is then equal to the LO frequency supplied by the mixer module. That is, $f_{\mathrm{LO}} = 3.5$ GHz for boundary frequencies 0.3 GHz and 3.8 GHz. In this way, maximization of the band's usability is ensured over a continuous tuning range, specially where upconversion and downconversion are performed, i.e. at the upper-bound frequency 3.8 GHz of the RF-signal processor bands $\mathrm{Tx_2}$ and $\mathrm{Rx_1}$.

In order to extend the overall tuning range, two mixers are required to enable transmission and reception of signals at the same, i.e. bidirectional communication employing different frequency bands. Thus, mixer 1 is used for upconversion described by

$$\begin{aligned} f_{\mathrm{RF,out}} = f_{\mathrm{RF,in}} + f_{\mathrm{LO}} &= (0.3\ldots3.8)\ \mathrm{GHz} + 3.5\,\mathrm{GHz} \\ &= (3.8\ldots7.3)\ \mathrm{GHz}, \end{aligned} \tag{3.1}$$

where $f_{\mathrm{RF,in}}$ is the frequency band of the outgoing signal from Tx_2 band at the RF-signal processor. The resulting $f_{\mathrm{RF,out}}$ represents the frequency of the upconverted signal at the output of the mixer module to transmit in the extended band Tx'_2. Mixer 2 is used for downconversion set up according to

$$\begin{aligned} f_{\mathrm{RF,out}} = f_{\mathrm{RF,in}} - f_{\mathrm{LO}} &= (3.8\ldots6.3)\ \mathrm{GHz} - 3.5\,\mathrm{GHz} \\ &= (0.3\ldots2.8)\ \mathrm{GHz}, \end{aligned} \tag{3.2}$$

where $f_{\mathrm{RF,in}}$ is the frequency of the incoming signal at the input of the mixer module to receive in the extended band Rx'_1, and $f_{\mathrm{RF,out}}$ is the frequency of the downconverted signal at Rx_1 band of the RF-signal processor.

The overall transceiver architecture previously shown in Fig. 3.1, can be implemented by the combination of the RF-signal processor and the mixer module. As a consequence, two different operation modes are enabled for upconversion and downconversion. The first, with the single operation of the RF-signal processor, and the second, including the operation of the RF-signal processor together with the mixer module.

Two ports of the RF-signal processor, Tx_2 and Rx_1, combined with the mixing stage, are used for upconversion and downconversion, correspondingly. In the transmission case with signals in the range of up to 7 GHz, and in the receiver case with signals in the frequency range of up to 6 GHz. Furthermore, integrated low pass filters in both Tx and Rx paths of the RF-signal processor provide an adjacent image rejection of more than 55 dB[1] falling into the first 3 MHz below or above the desired signal.

Due to the flexibility of operation of the reconfigurable architecture, other combinations can be realized between the frequency bands of the RF-signal processor and the local oscillator frequency f_{LO} of the mixer module. Hence, resulting in multiple solutions to achieve a determined tuning range. Factors such as the operation frequency of the components that integrate the signal path, available power in the RF-signal processor, and conversion gain of the mixer module, are considered to achieve the realization of the demonstrator in the following configuration.

Upconversion Mode Operation. In Fig. 3.4, the configuration of the transceiver upconversion bands for the Tx ports are shown. The bands covered by the RF-signal processor are shown at the top of the figure. At the bottom, the configuration can be

---

[1] Current mobile standards define different requirements such as in-band blocking (−56 dBm), out-of-band blocking (−44 dBm) and narrowband blocking (−57 dBm) [7].

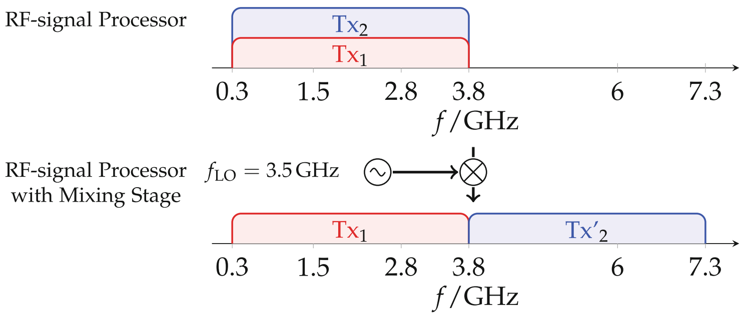

Fig. 3.4 Upconversion: Extension of the transceiver tuning range for the transmission signal path by frequency conversion. The frequency conversion is realized with a mixing stage of the Tx_2 band at the RF-signal processor, into Tx'_2 band at the output of the mixer module

seen for extended frequency operation with the mixer module. In this case, the Tx_2 port was selected so that, together with Tx_1, the transmitter can cover a continuous frequency range from 0.3 to 7.3 GHz.

Downconversion Mode Operation. Figure 3.5 shows the configuration of the transceiver downconversion bands for the Rx ports. Extended frequency operation with the mixer can be seen at the top of the figure. Covered bands by the RF-signal processor are shown at the bottom. The Rx_1 port was selected in such a way that, in combination with Rx_2 and Rx_3, the receiver can cover a continuous band from 0.3 to 6.3 GHz.

Operation at border frequencies, e.g. 1.5, 3.0 or 3.8 GHz, is ensured in both operation modes, i.e. either by Tx_1 or Tx'_2 bands, and Rx_2 or Rx'_1 bands, for transmission and reception, correspondingly. This characteristic is attained since the transceiver

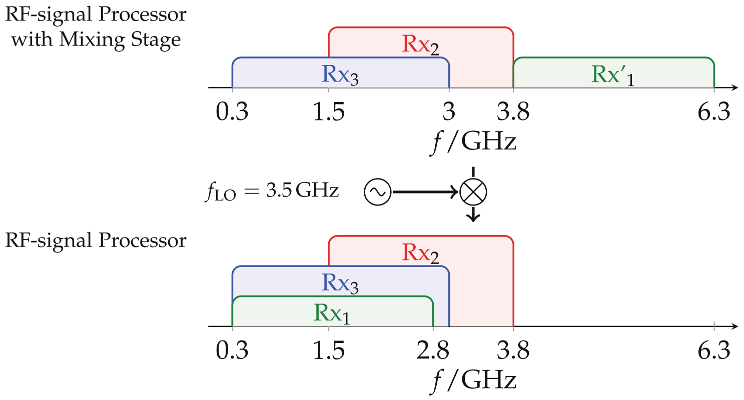

Fig. 3.5 Downconversion: Extension of the transceiver tuning range for the receiver signal path by frequency conversion. The frequency conversion is realized with a mixing stage of the Rx'_1 band at the input of the mixer module, into Rx_1 band at the RF-signal processor

architecture, based on separated RF ports, provide enough isolation between the signal paths.

Although the selected LO frequency is used to achieve a compromise between overlapping bands and operation frequency of the LMS6002D signal processor together with the mixer module, other configurations of the LO frequency can be used to shift the bands of the RF-signal processor.

3.2 Characterization of RF Components

Due to the very large frequency range in which the transceiver operates, technology evaluation of the transceiver previously shown in Fig. 3.1 requires components with a wideband characteristic.

To establish the complete Tx/Rx signal path, RF ports of the signal processor LMS6002D are enabled for higher operation frequencies. This implementation employs a wideband synthesizer with integrated mixer and a filtering stage at the outputs of the mixer for upconversion and downconversion. Furthermore, a gain block amplifier for compensation of the conversion gain is used along with a circulator to isolate the Tx signal from the Rx signal, and a circular monopole antenna.

3.2.1 Wideband Synthesizer with Integrated Mixers

As previously shown in Sect. 3.1, mixers for upconversion and downconversion are used to extend the covered frequency range of the transceiver for the Tx and Rx paths. Thereafter, a filtering stage for rejection of harmonics outside the desired range is employed, and an amplifier for compensation of the mixer conversion loss.

Since the IC RFFC5071A includes two mixers and a local oscillator, to guarantee the duplex operation mode of the platform, the Tx and Rx paths use the same frequency for upconversion and downconversion, i.e. $f_{\mathrm{LO}} = 3.5\,\mathrm{GHz}$. Furthermore, the control of both, signal processor and mixer module, can be performed by a backend software.

A model of the input and output impedances of the mixer are shown in Fig. 3.6. The mixer itself has a common gate input. The input is dominated by parasitic impedances of the package and PCB stray, such as shunt capacitance of the device gates $C_{\mathrm{P1}} = 0.5\,\mathrm{pF}$ along with the bond wire inductances of about $L_{\mathrm{w}} = 0.5\,\mathrm{nH}$, and the resistance R_{in} which is inversely proportional to the mixer current setting. A typical value for this resistance is $R_{\mathrm{in}} = 85\,\Omega$ for a current of 20 mA. In a similar way as for the inputs, the impedance at the outputs can be modeled by a resistance of $R_{\mathrm{out}} = 2\,\mathrm{k}\Omega$ with a shunt PCB stray capacitance of $C_{\mathrm{P2}} = 1\,\mathrm{pF}$ and the bond wires inductances [8].

Considering the input and output impedances of the mixer, in case of the mixer input, a balun with corresponding matching circuit is needed to transform from a

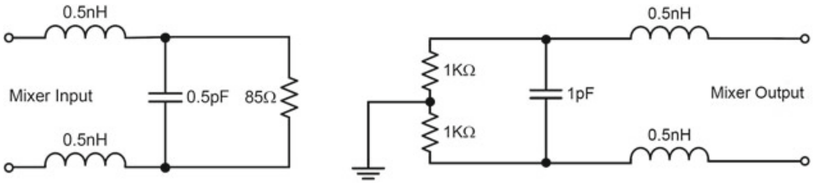

Fig. 3.6 Equivalent circuit of the mixer with input and output impedances of the mixer board with embedded IC RFFC5071A [4]

Table 3.1 Employed components for conversion of the balanced input and output ports to typical unbalanced 50 Ω system characteristic impedance in the mixer module

Balun	Operation mode	Frequency range (GHz)
4000BL14U100	Down conversion input	3.1–4.8
	Up conversion output	
RFXF8553	Down conversion output	0.5–2.5
RFXF9503	Up conversion input	<3

typical 50 Ω unbalanced source into the complex balanced impedance. In the other case, the mixer output is designed to drive a load resistance around 200 Ω. Hence, a 4:1 balun is used to perform the balanced-to-unbalanced conversion together with the impedance transformation.

An important challenge is the required matching along the frequency range of interest at the input and output ports of the mixer module to perform proper signal conversion. A trade-off should be found between the conversion gain, the frequency range, and the required matching realized by external components at the input and output ports of the mixer [8]. A variety of commercially available baluns exists, nevertheless most of them do not cover the complete necessary frequency range to perform the required conversion. Specifically, baluns from the manufacturer Johanson Technology cover from 3.4 to 4.0 GHz and from 4.9 to 5.9 GHz, or from 3.1 to 4.9 GHz from the manufacturer TDK. State-of-the-art components were considered in terms of the required operation range and available footprint in the RFMD module board. Thus, the baluns shown in Table 3.1 were used for implementation of the matching circuits as presented in the equivalent circuits of Fig. 3.7.

In Fig. 3.8 the ideal conversion gain (dashed) is shown considering a perfectly matched lossless mixer employing scattering parameters from the manufacturer for the RFXF8553 and 4000BL14U100 baluns at the corresponding frequency range. The ceramic balun from Johanson Technology 4000BL14U100 with a frequency range from 3.1 to 4.8 GHz was used at the RF input for downconversion (a) and RF output for upconversion (d).

In the case of the IF output for downconversion (b), an RFXF8553 4:1 balun from RFMD was used with a shunt inductance to give best performance at frequencies around 1 GHz. Although at required frequencies the balanced to unbalanced impedance transformation is performed, the performance of the balun is abruptly

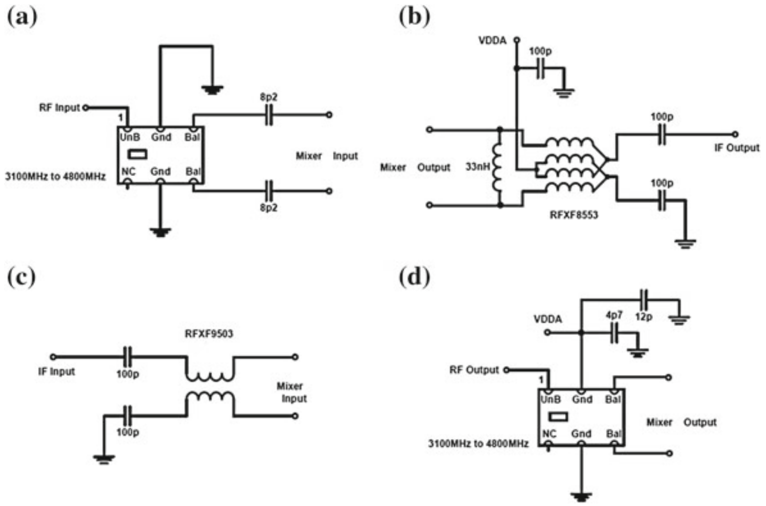

Fig. 3.7 Matching circuits at the inputs and outputs of the mixers included in the mixer module RFFC5071A [4]. **a** Down Conversion RF Input, **b** Down Conversion IF Output, **c** Up Conversion IF Input, **d** Up Conversion RF Output

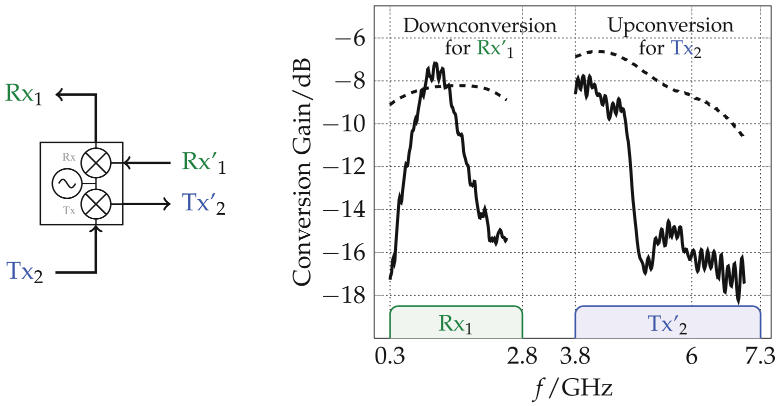

Fig. 3.8 *Left* Diagram of mixer module with the corresponding routed RF inputs and outputs for extension of the transceiver tuning range. *Right* Ideal (*dashed*) conversion gain of baluns and measured (*solid*) conversion gain of downconversion and upconversion for extension of band Rx_1 and band Tx'_2

reduced outside its frequency of operation. This abrupt behavior is caused due to the narrowband characteristic of the inductor $L = 33\,\mathrm{nH}$ at the output of the circuit. Finally, the RFXF9503 1:1 balun enabling the frequency range up to 3 GHz was employed in the case of the IF input for upconversion (c).

Conversion gain measurements of the mixers for the selected local oscillator frequency $f_{\mathrm{LO}} = 3.5\,\mathrm{GHz}$ were performed for upconversion and downconversion stages to combine with the LMS6002D bands, i.e. Rx_1 and Tx'_2. Figure 3.8 also shows the resulting mixer conversion gain (solid) of band Tx_2 after upconversion: Tx'_2 (mixer RF output), and of Rx'_1 band after downconversion: Rx_1 (mixer IF output) along the required frequency range. The conversion gain was measured with power input values from -10 to $+5$ dBm for the upconversion mode from 3.8 to 4.8 GHz and for the downconversion mode from 0.8 to 1.6 GHz. Different input powers between -10 dBm and $+5$ dBm cover these frequency ranges in effect similarly. Although the measured conversion gain outside the considered frequency ranges decays to values lower than -16 dB due to the narrowband characteristic of the components, compensation of the decay is taken into account in the amplification stage for improvement of the overall response.

As it can be seen, a major drawback of this mixer are the balanced ports. However, the compactness of the integrated local oscillator and the two mixers within a single IC are key factors for purposes of this implementation. These factors result in the employment of a minimum amount of components to cover a continuous wide frequency band.

Although an extension of the transceiver frequency range of operation is shown, due to the noticeable abrupt change in the conversion gain, special attention to overcome this limitation can be given. Such limitation can be mitigated by compensating the conversion gain through an amplification block, and by selecting baluns for the corresponding differential inputs/outputs of the mixer. Thereafter, the required operation frequency can be optimized via adaptive matching.

Due to the fact that most of current mobile applications concentrate in the lower part of the frequency spectrum below 3.5 GHz, the mixer RF output for downconversion and RF input for upconversion is less challenging to implement. On the contrary, in the case of the RF input for downconversion and RF output for upconversion, the number of components commercially available is limited at the frequency range above 3.5 GHz. At the time of this implementation, components covering this range were not available due to the required wide frequency range, e.g. from 3 GHz up to at least 6 GHz. However, extension of the frequency operation range of the transceiver is proven with the proposed mixing stage principle. In this case, to improve the mixer performance at the specified bands, the PCB layout of the mixer module should be redesigned according to the required footprint of the balun with its corresponding matching circuit to enable the wide frequency operation range of at least up to 6 GHz.

3.2.2 *Band-Pass Filter for Extended Bandwidth*

To provide a reliable rejection of signals out of the desired extended frequency range of operation, a filtering stage is added to the Tx and Rx signal path. Due to the low commercial availability of band-pass filters for the required frequency range, the filtering stage consists of two cascaded coaxial filters. This cascaded filters are a low-pass filter and high-pass filter from the manufacturer Mini-Circuits [9, 10]. Measurements of the low-pass and high-pass response are shown in Fig. 3.9 (left).

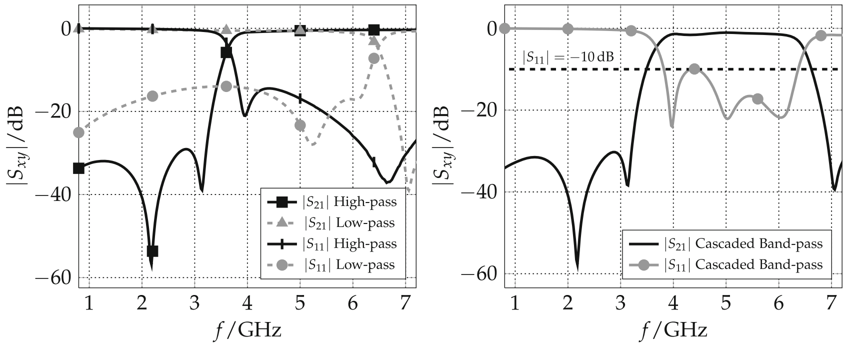

Fig. 3.9 *Left* Scattering parameter measurements of the high-pass filter and low-pass filter. *Right* Scattering parameter measurements of the cascaded band-pass filter with cutoff frequencies at 3.7 GHz and 6.4 GHz

The high-pass filter exhibits a flat passband from 3.7 GHz and higher than 7 GHz. The low-pass filter exhibits a flat passband below 6.4 GHz. Both filters exhibit a transmission loss better than 1 dB and a maximum input reflection of −14 dB.

Consequently, the resulting passband created by the cascaded filters lies between 3.7 GHz and 6.4 GHz. In Fig. 3.9 (right), scattering parameter measurements of the cascaded coaxial filters forming a band-pass filtering are shown. The overall response exhibits a flat transmission loss of 1.4 dB and a minimum reflection of −10 dB in the passband. Moreover, in the phase response at the frequency range of interest of the S_{21} parameter, a linear characteristic predominates.

3.2.3 Gain Amplifier

To select the amplification stage, characteristics such as covered frequency range, maximum gain, noise figure, external biasing, and simplicity of integration were taken into account to realize a modular design. An amplifier with gain over a wide frequency response is realized to have the flexibility of its employment covering all of the transceiver bands. Thus, it can be used either for improvement of the signal at the RF ports of the RF-signal processor, or after the mixing stage where the extended frequency range operates. That is, at a lower frequency range from 2 to 3.8 GHz for downconversion, or at a higher frequency range between 3.8 GHz and at least up to 6 GHz for upconversion to compensate the mixer conversion gain.

A gain amplifier module in planar microstrip technology to employ along the frequency range up to 6 GHz shown in Fig. 3.10, was fabricated on an FR4 substrate with $\varepsilon_r = 4.4$, loss tangent $\tan\delta = 0.027$ and 1.33 mm thickness. The NBB-400 broadband amplifier from the manufacturer RFMD [11] with noise figure of around 3 dB was used with regulated external biasing $V_{\mathrm{CC}} = +5$ V for a component supply voltage of 3.6 V.

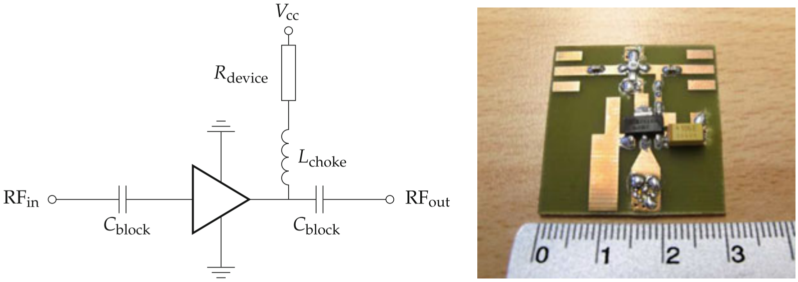

Fig. 3.10 Schematic of the gain amplifier biasing circuit and photo of the fabricated component

According to the requirements considering the conversion gain of the mixing stage which decreases around 8 dB at 1 GHz and 4 GHz, at least a gain of 10 dB is required over the complete frequency range up to 6 GHz. In Fig. 3.11 (left), the input reflection $|S_{11}|$ and forward transmission $|S_{21}|$ parameters from the manufacturer are compared with the measurements of the implemented amplifier. The $|S_{11}|$ parameter has an input reflection better than -10 dB up to 5.5 GHz. As shown in the forward transmission $|S_{21}|$, the gain over the whole frequency range from 1 to 7 GHz decreases gradually from a maximum gain of 17 dB to 7 dB. Reduction of the transmission parameter is observed due to fabrication constraints in the ground contacts of the amplifier. This reduction results in a slight frequency notch around 5.6 GHz that affects also the phase response at this frequency. Phase response of the forward transmission S_{21} is shown in Fig. 3.11 (right). The amplifier exhibits a linear phase characteristic over the frequency range up to 5.5 GHz. Above this frequency, due to the influence of the notch shown in the forward transmission, the phase loses linearity at frequencies above 5.6 GHz and below to 7 GHz.

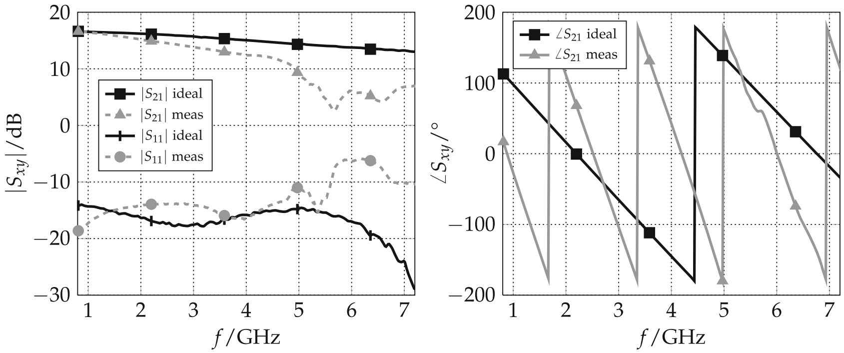

Fig. 3.11 *Left* S-parameter magnitude measurements of the amplifier with 17 dB at 1 GHz, 12 dB gain at 4 GHz and decreasing around 6 dB at 6 GHz. *Right* S-parameter phase measurements of the amplifier with linear phase up to 5 GHz, and at 5.6 GHz with a variation influenced by the notch presented at the same frequency in the magnitude of the transmission

Improvement of the fabrication process can be realized although a flat gain response is difficult to achieve covering the complete frequency range for the Tx and Rx path with current available components. Such improvements can be performed by employing wire bonding and keeping the distance between the bond wires as short as possible. Another option is to increase the amount of attached vias holes and clamping of metalizations into the substrate. This means, an effective grounding of the component results in a reduction of the losses in the overall frequency response. Hence, the losses introduced by the mixer conversion gain can be mitigated.

3.2.4 Coaxial Circulator

A circulator to enable the transceiver for duplex communication is employed before the antenna input port. The circulator has the task to simultaneously separate and isolate the signals to transmit and to receive from a single antenna in this reconfigurable transceiver architecture. Scattering parameter measurements of the coaxial circulator D3C2060 from Ditom Microwave [12] are shown in Fig. 3.12.

The $|S_{13}|$ parameter describing the path from the Tx port to the antenna input port, and $|S_{21}|$ parameter from the antenna input port to the Rx port, exhibit an average transmission value of −0.3 dB within a 3 dB-bandwidth from 1.8 to 6.5 GHz. The measured $|S_{33}|$ at the Tx port, and $|S_{22}|$ at the Rx port, show a minimum input reflection of −16 dB. And the isolation $|S_{23}|$ between the Tx and Rx port exhibits a minimum value of −17 dB.

On the wide tuning range up to 7.3 GHz for the Tx path and 6.3 GHz for the Rx path, as shown in Fig. 3.12, in this implementation the circulator essentially limits the original wide operation frequency range. Consequently, due to its limited frequency passband the resulting covered range is from 1.8 to 6.5 GHz.

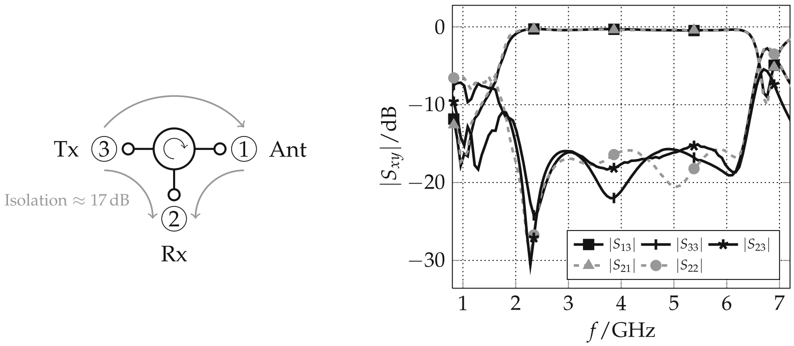

Fig. 3.12 Scattering parameters magnitude measurements of the circulator. $|S_{13}|$ transmission from Tx port to antenna port, $|S_{21}|$ transmission from antenna port to Rx port, $|S_{33}|$ input reflection at Tx port, $|S_{22}|$ reflection at Rx port, and $|S_{23}|$ isolation between Tx and Rx ports

Regarding the isolation, achieved values of around −17 dB can be compared with services employed in portable devices such as GPS or WLAN. This can be also compared when an isolation around −20 dB is required in a scenario using a single antenna per service; or for MIMO applications, where investigations demonstrate an isolation between the antennas of around −15 dB [13, 14]. For applications such as UMTS or LTE a minimum isolation of −40 dB should be planned in the different Tx/Rx bands with a single antenna [15]. Thus, since the value of around −20 dB is not sufficient for proper isolation according to current standards, typically an additional filtering stage for every band is required to block the energy of the undesired signal. For example, single and dual filters from the manufacturers Epcos (B85xx and B86xx for LTE, and B94xx or B9604 for navigation, WLAN and Bluetooth among others) or Murata (SAWFD1G90 or SAFEA2G) can be used. The main constraint of these kind of components is that they are narrowband. Hence, leading to an increase in the amount of components in the RF-frontend. That is, the ideal solution requires a component with a wide band characteristic which currently is not available.

A trade off should be found between the amount of elements used and the resulting benefit to the overall system. That is, the fact that a reconfigurable transceiver with wide frequency range is employed, means that it can be covered a very large amount of operation frequencies. As a consequence, a very high number of components for different bands would be required if such isolation is intended to be achieved with a single antenna port. Therefore, different approaches can be realized to overcome this limitation. Such is the case of the employment of different antennas to separate Tx/Rx signal paths; and reduction of the signal correlation between the antennas by realizing, for example, feeding networks based on decoupling elements to optimize the antenna matching [16–18].

3.2.5 Circular Monopole Antenna

An circular monopole antenna is employed for evaluation of the reconfigurable transceiver and to enable the transmission and reception of signals across the resulting frequency range shown by the circulator, i.e. covering the spectrum between 1.8 GHz and less than 6.5 GHz.

The antenna shown in Fig. 3.13 was simulated on CST Microwave Studio [19] and fabricated on a Rogers RT5880 substrate with $\varepsilon_r = 2.2$, loss tangent $\tan\delta = 0.0001$ and 1.576 mm thickness. The diameter of the circular monopole is 51 mm, and the occupied area of the ground plane is 15cm^2. The required bandwidth exhibits an input reflection of at least $|S_{11}| < -10$ dB covering from 1.3 GHz up to more than 7 GHz. In Fig. 3.14, the current distribution for different operation frequencies covering different services is shown: (a) at 1.9 GHz covering mobile services and bluetooth/zigbee, (b) at 3.6 GHz for WLAN, WiMAX and higher bands of LTE, and (c) at 5.9 GHz for higher bands of WLAN and Car-to-Car communication. In the case of the operation frequency at 1.9 GHz, it can be seen that a vertical current flow is excited through the monopole. When the frequency increases, as in the case

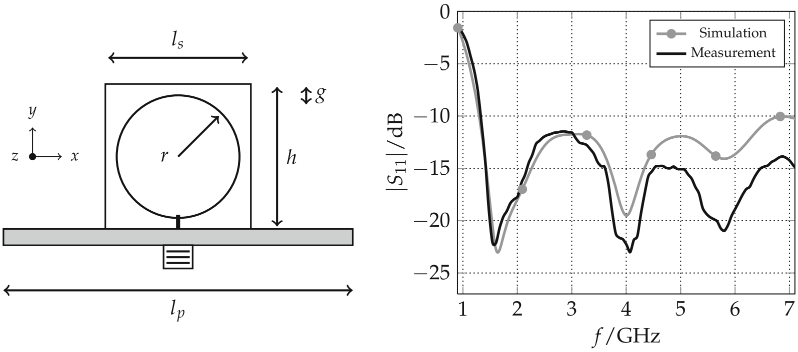

Fig. 3.13 Dimensions of the circular monopole. Scattering parameter measurement of the monopole antenna with input reflection $|S_{11}| < -10\,\text{dB}$ from 1.3 GHz up to more than 6 GHz

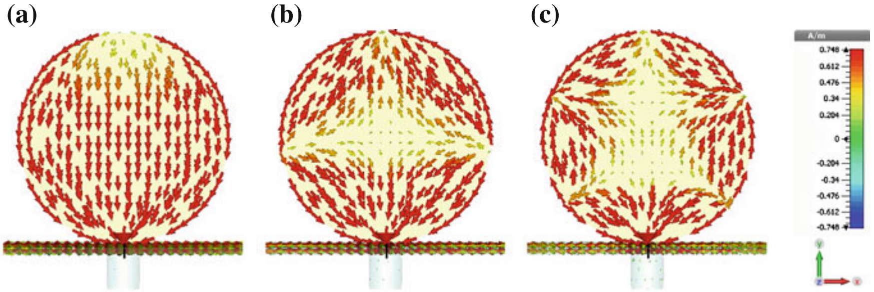

Fig. 3.14 Surface current distribution of the planar circular monopole for different operation frequencies: **a** 1.9 GHz, **b** 3.6 GHz and **c** 5.9 GHz

of 3.6 GHz and 5.9 GHz, higher modes are excited and thus, nulls in the monopole with intense current flow along the edges are generated. It can be recognized that the exhibited input matching of the antenna is due to the progressive beveling of the monopole together with the position of the feeding strip. That is, since the feeding strip is centered and closely attached to the ground plane of the antenna, it leads to a wide frequency match.

In Fig. 3.15, simulation results of the antenna farfield patterns for frequencies between 1.5 GHz and 6 GHz in the YZ-plane and XY-plane are shown. In the case of the YZ-plane it can be seen that a quasi-omnidirectional behavior is exhibited with nulls at ±90°. In the case of the XY-plane the main lobe direction is at around 45° and 135° in the considered frequency range. This angle can be decreased towards 0° by increasing the area of the ground plane [20].

As shown by the antenna farfield pattern in Fig. 3.16, the simulated antenna gain is considered at an angle of 45°. Hence, an average value of around 2 dB from 1.5 to 3.0 GHz is obtained. And for higher frequencies a maximum value at 4 GHz of

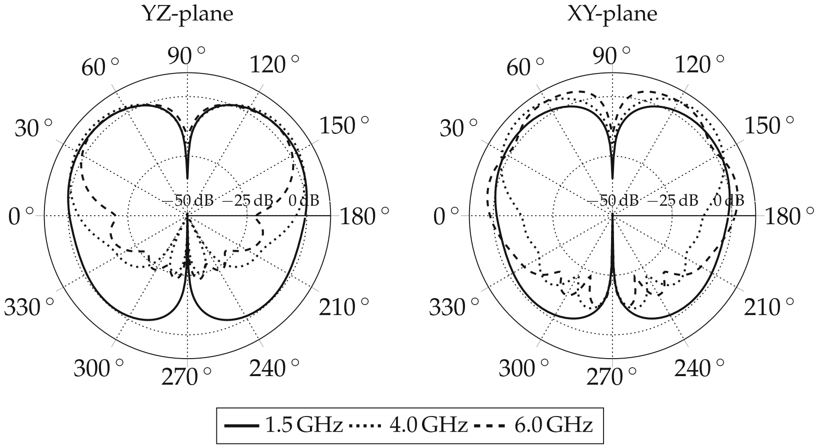

Fig. 3.15 Farfield patterns of the circular monopole antenna gain in the YZ-plane and XY-plane for different operation frequencies, e.g. 1.5 GHz, 4 GHz and 6 GHz

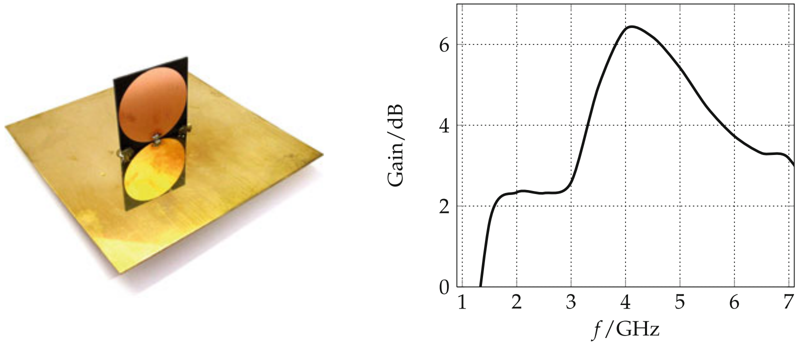

Fig. 3.16 Photo of the fabricated circular monopole antenna and simulated antenna gain over the frequency range with an average value of around 5 dB

6.3 dB is achieved, while along the frequency range above 4 GHz up to 7 GHz the gain smoothly decreases to 3 dB.

For demonstration purposes, this antenna satisfies the requirement to transmit and receive signals over the required frequency range. Monopole antennas can be used, for example, to enable a CR platform for spectrum sensing applications, and/or with several narrowbands for communication purposes. Several investigations in the literature have shown implementations focusing on the reconfiguration principle by employing techniques such as mechanical-electrical controlled rotational patch [21] and using switches, e.g. MEMS and p-i-n diodes [22, 23]. Therefore, by improving their characteristics, e.g. starting from static UWB antennas and converting them into reconfigurable UWB antennas, or by employing a discrete amount of tunable narrowband antennas, they can be an attractive approach to reduce the requirements

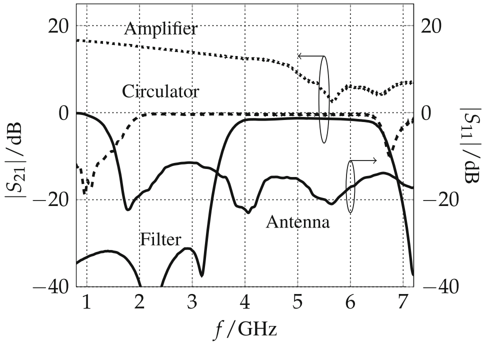

Fig. 3.17 S-parameters measurement of backend transceiver components focused on the performance for extension of the transceiver frequency range bands Rx'_1 and Tx'_2

of band rejection [24, 25], as well as to achieve reconfiguration of the operation frequency [26].

To have an overview of the frequency response of each component with the proposed Tx/Rx signal path, measurements of the forward transmission $|S_{21}|$ of the filter, amplifier, and circulator, as well as the input reflection $|S_{11}|$ of the circular monopole antenna are summarized in Fig. 3.17.

3.3 Transceiver Link Budget and Evaluation

Measurements of the Tx/Rx part of the reconfigurable transceiver were performed following the transceiver setup shown in Fig. 3.1. First, considering the transceiver only. Afterwards, measuring the transceiver at a distance of 1 m, as shown in Fig. 3.18. For evaluation of the setup, a double-ridged horn antenna from the manufacturer ETS-Lindgren 3115 with a gain of around 9 dB across the desired frequency range was used at the signal analyzer and signal generator.

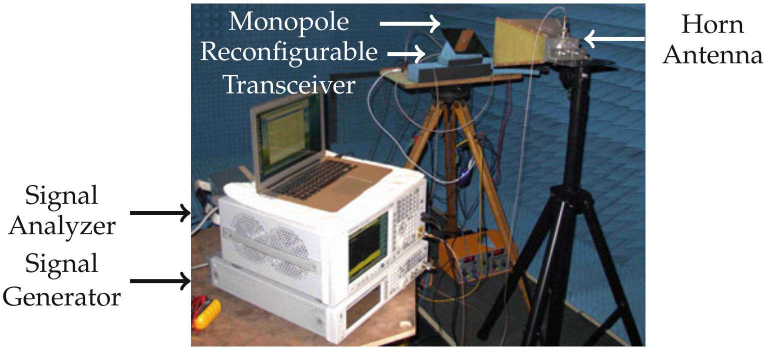

Fig. 3.18 Wireless spectrum measurement setup in the anechoic chamber

Straightforward calculation of the link budget from port Tx_2 up to the antenna at the signal analyzer, based on element-wise measurements of the transceiver components, yields

$$P_{\mathrm{SA}} = P_{\mathrm{Tx2}} + G_{\mathrm{m}} - L_{\mathrm{c}} + G_{\mathrm{a}} + G_{\mathrm{Ant\,Tx}} - L_{\mathrm{s}} + G_{\mathrm{Ant\,Rx}}. \tag{3.3}$$

On the one hand, gain of the amplifier G_{a} and gains of the Tx/Rx antennas, G_{AntTx} and G_{AntRx} correspondingly, are taken into account. On the other hand, G_{m} is defined by the mixer conversion gain, L_{c} by the filter, switches, circulator and cable losses, and L_{s} by the free space loss

$$L_{\mathrm{s}} = 20\log_{10}\left(\frac{4\pi d}{\lambda}\right) \tag{3.4}$$

considering a separation d between Tx antenna and Rx antenna. Thus, resulting in a received power

$$P_{\mathrm{SA}} \approx +6\,\mathrm{dBm} - 8\mathrm{dB} - 5\,\mathrm{dB} + 13\mathrm{dB} + 4\,\mathrm{dB} - 44\,\mathrm{dB} + 6\,\mathrm{dB} = -28\,\mathrm{dBm}, \tag{3.5}$$

of the double-ridge horn antenna port at 4 GHz. The reached level of $P_{\mathrm{SA}} \approx -28$ dBm is confirmed by the measured amplitude at the same frequency of 4 GHz equal to −27.04 dBm in Fig. 3.20.

Evaluation of the Reconfigurable Wideband Transceiver

Figure 3.19 shows the completely mounted demonstrator. To verify the proof of concept, wireless measurements of the reconfigurable transceiver measured power P are performed with a separation of 1 m between Tx and Rx antennas. Results of the experimental validation and modeled link budget from 1 to 7 GHz considering the measured power at the signal analyzer are shown in Fig. 3.20.

According to the defined bands Tx_1 and Tx'_2, a signal swept over the frequency range of interest is transmitted from the demonstrator. (i) For Tx_1, the maximum power of the signal processor is +6 dBm optimized at 2 GHz, nevertheless its performance changes while the frequency is tuned due to the change of the impedance matching at external components around the integrated circuit. (ii) In Tx'_2, due to the amplification stage with the mixer, the best performance is present from 4 to 5 GHz. The performance above 5 GHz exhibits a stronger decay mainly due to the reduced upconversion gain combined with the amplification stage shown in Figs. 3.8 and 3.11 correspondingly, thus, resulting in values lower than −50 dBm above 5 GHz.

Performance overview of the transceiver transmitted power together with the wireless measurement results is shown in Fig. 3.20. Similarly to the wireless measurement results, the transmitted power decay can be recognized for higher frequencies with an amplitude variation of around 30 dBm. However, results of the amplitude variation can be achieved when the performance of the mixing stage and amplification stage is improved according to the results shown in their corresponding sections. Regarding the employed components in this architecture, the ideal amplitude variation of the

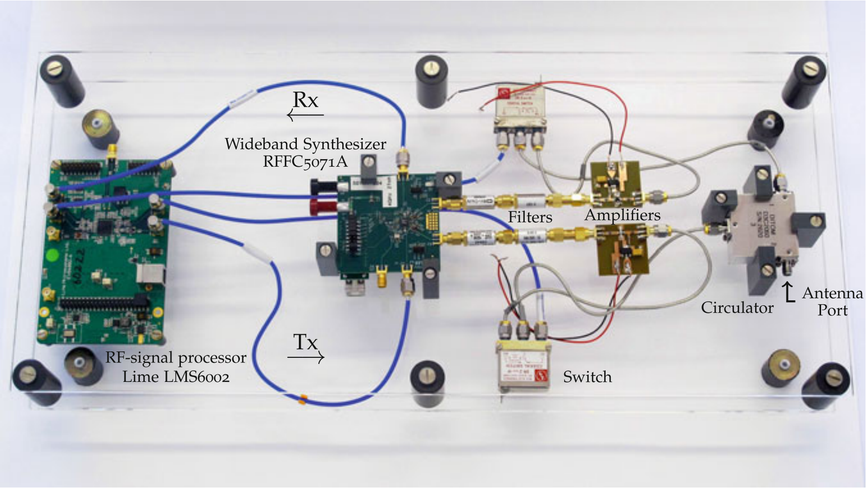

Fig. 3.19 Photo of whole demonstrator of the reconfigurable transceiver with RF-signal processor LMS6002D and wideband synthesizer RFFC5071A for extended continuous tuning range up to 7 GHz for transmission and 6 GHz for reception. The realized demonstrator has been developed within the framework of the LOEWE research priority program Cocoon "Cooperative Sensor Communication"

transmitted power shown in Fig. 3.20 takes into account enhancement of the mixer matching and amplification in the Tx'_2 band. Further improvement can be achieved if a larger frequency passband is considered compared to the passband of the employed circulator. Regarding the mixing stage, simulation of the employed balun in Fig. 3.8 is

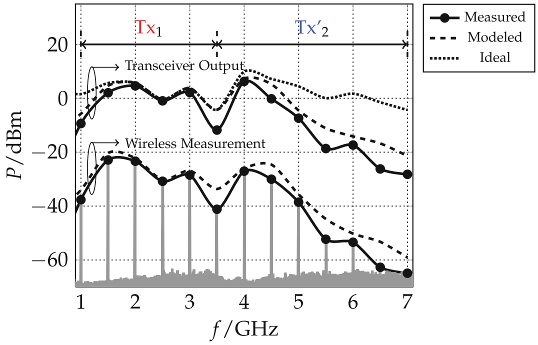

Fig. 3.20 *Wireless measurement* Measured power of reconfigurable transceiver transmitted power for direct mode Tx_1 and upconversion mode Tx'_2. Wireless measurement performed with a separation of 1 m between Tx and Rx antennas. *Transceiver output* Performance of transceiver ideal and measured transmitted output power. The ideal performance is achieved by improving the amplitude characteristics of the employed mixing stage and amplification stage. Transmitted power of Tx_1 band: direct mode operation (RF-signal processor only) and Tx'_2 band: upconversion mode (extended tuning range)

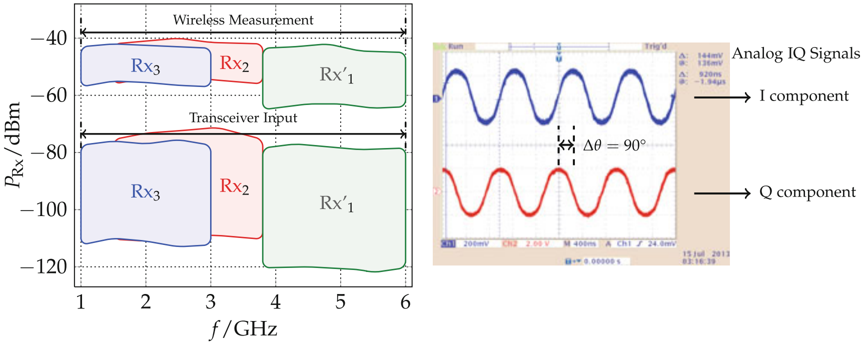

Fig. 3.21 *Wireless measurement* Spectrum P_{Rx} of reconfigurable transceiver received power for direct mode Rx_2 and Rx_3, and downconversion mode Rx'_1 performed with a separation of 1 m between Rx and Tx antennas. *Transceiver input* Performance of transceiver received power without considering free space loss and antenna gains. *Analog IQ components* Wireless measurement performed at Rx_1 port of a receiver test at an $f_{\mathrm{Rx}} = 5.9$ GHz for downconversion to baseband

taken into account with the improved mixer conversion gain, specifically from around 10 dB to 7 dB in the range from 5 to 7 GHz. For the amplification stage shown in Fig. 3.11, simulations of the manufacturer are considered yielding an amplitude variation lower than 5 dB over the complete band. As a result, the complete frequency range from 1 to 7 GHz is improved with an amplitude variation of around 14 dBm and maximum output power of up to $P_{\mathrm{Tx}} = +10$ dBm.

For the Rx case, a signal was swept over frequency from the signal generator (Tx) and transmitted by the commercial antenna to the reconfigurable platform (Rx) from 1 to 6 GHz. IQ components with a phase difference of 90° were measured at the signal processor. Measurement results of the Rx transceiver part are shown in Fig. 3.21. The wireless measured received power at the input of the transceiver laid from around −57 dBm to −40 dBm for band Rx_3 and band Rx_2, and from −65 dBm to m−42 dBm for band Rx'_1, respectively. The measured received power at the input of the transceiver without considering L_s free space loss and antenna Tx/Rx gains laid from around −113 dBm to −71 dBm for band Rx_3 and band Rx_2, and from −121 dBm to −78 dBm for band Rx'_1, respectively. This values can be compared with those in current and future mobile standards such as GSM, UMTS and LTE, with required values of the user equipment from around −70 dBm to −115 dBm [27].

As an example of previous results, by employing an oscilloscope and measuring directly at the analog IQ pins of the RF-signal processor, comparison of the IQ components of a transmitted signal at $f_c = 5.9$ GHz is shown in Fig. 3.21. The received power at Rx_1 port of the RF-signal processor was detected at a level of −46 dBm with receiver operation frequency of 2.4 GHz. Thus, the IQ components with a difference of 90° were taken with a period of the signal corresponding to 1 μs in the oscilloscope view.

As shown by the characterization of the signal path in the overall transceiver, the performance of the proposed frequency range is reduced by the mixing stage, the employed circulator, amplification stage (Tx case only), and of less magnitude, the gain of the circular monopole antenna. However, by improving the frequency characteristic of the mixing stage and amplification stage an optimized amplitude mitigates the strong decay for frequencies above 4 GHz. Due to the low availability of components covering the proposed wide frequency range, other solutions can be realized to overcome the shortening constraint of the wide operation range. For example, two antennas that separate the Tx and Rx paths can be employed to keep the requirement of a duplex communication platform at the expense of an increment in the amount of elements or components used. Similarly, depending on the required services and applications, improvement of the isolation between neighboring frequencies and/or Tx and Rx bands can be realized by employing further filtering stages. Furthermore, compactness of the antenna is an open task to face. The implemented UWB monopole antenna satisfies the system requirements for demonstration purposes. However, different criteria should be further considered in the case of a compact and portable implementation. For instance, its size should be optimized to meet housing requirements as well as adequate matching to environmental influences targeting focused applications of the user equipment. This can be realized by compact reconfigurable multiband antennas employing an adaptive matching where the narrowband signal is instantaneously tuned covering the required wide frequency tuning range.

References

1. J. Lotze, S. Fahmy, J. Noguera, L. Doyle, A model-based approach to cognitive radio design. IEEE J. Sel. Areas Commun. **29**, 455–468 (2011)
2. P. McFdries, The city as system [technically speaking]. IEEE Spectr. **51**, 36–36 (2014)
3. Lime microsystems ultra flexible fprf solutions, 2014. http://www.limemicro.com/. Accessed August 2014
4. RFMD RFFC5071A/2A Datasheet. Wideband Synthesizer VCO with Integrated 6 GHz Mixer (2012)
5. LMS6002D Quick Start Manual. Lime Microsystems Limited (2012)
6. RFMD GUI Control Software Tool Setup V2.0.00a (2012)
7. 3GPP ts 34.121-1 version 9.3.0 release 9. universal mobile telecommunications system (UMTS); User Equipment (UE) conformance specification; radio transmission and reception (FDD); part 1: Conformance specification. etsi ts 134 121-1 v9.3.0 (2011)
8. RFMD. RFFC507x Application Note Mixer Performance Above 4 GHz (2012)
9. Mini-Circuits Coaxial Low Pass Filter VLF-5500
10. Mini-Circuits Coaxial High Pass Filter VHF-3800
11. RFMD NBB-400 Cascadable Broadband GaAs MMIC amplifier DC to 8 GHz
12. Ditom Microwave D3C2060 SMA Circulator Datasheet
13. J. Guo, J. Fan, L. Sun, B. Sun, A four-antenna system with high isolation for mobile phones. IEEE Antennas Wirel. Propag. Lett. **12**, 979–982 (2013)
14. D. Yuan, Z. Du, K. Gong, Z. Feng, A four-element antenna system for mobile phones. IEEE Antennas Wirel. Propag. Lett. **6**, 655–658 (2007)
15. Technical specification group radio access network; lte for 700 mhz digital dividend. 3gpp tr 36.820 v11.1.0 (2012-09), (2012)
16. R. Gomez-Garcia, M. Sanchez-Renedo, J.-M. Munoz-Ferreras, A type of planar array-antenna feeding network with single/multiband filtering capability. IEEE Antennas Wirel. Propag. Lett. **9**, 1271–1274 (2010)

17. C. Yang, J. Kim, H. Kim, J. Wee, B. Kim, C. Jung, Quad-band antenna with high isolation mimo and broadband SCS for broadcasting and telecommunication services. IEEE Antennas Wirel. Propag. Lett. **9**, 584–587 (2010)
18. A. Mak, C. Rowell, R. Murch, Isolation enhancement between two closely packed antennas. IEEE Trans. Antennas Propag. **56**, 3411–3419 (2008)
19. CST - Computer Simulation Technology 3D EM Simulation (2013)
20. Y. Lu, Y. Huang, H. Chattha, P. Cao, Reducing ground-plane effects on UWB monopole antennas. IEEE Antennas Wirel. Propag. Lett. **10**, 147–150 (2011)
21. P. Lotfi, M. Azarmanesh, S. Soltani, Rotatable dual band-notched UWB/triple-band WLAN reconfigurable antenna. IEEE Antennas Wirel. Propag. Lett. **12**, 104–107 (2013)
22. B. Badamchi, J. Nourinia, C. Ghobadi, A. Valizade Shahmirzadi, Design of compact reconfigurable ultra-wideband slot antenna with switchable single/dual band notch functions. IET Microw. Antennas Propag. **8**, 541–548 (2014)
23. S. Yang, C. Zhang, H. Pan, A. Fathy, V. Nair, Frequency-reconfigurable antennas for multiradio wireless platforms. IEEE Microw. Mag. **10**, 66–83 (2009)
24. A. Kalteh, G. DadashZadeh, M. Naser-Moghadasi, B. Virdee, Ultra-wideband circular slot antenna with reconfigurable notch band function. IET Microw. Antennas Propag. **6**, 108–112 (2012)
25. J. Perruisseau-Carrier, P. Pardo-Carrera, P. Miskovsky, Modeling, design and characterization of a very wideband slot antenna with reconfigurable band rejection. IEEE Trans. Antennas Propag. **58**, 2218–2226 (2010)
26. S. Aghdam, Reconfigurable antenna with a diversity filtering band feature utilizing active devices for communication systems. IEEE Trans. Antennas Propag. **61**, 5223–5228 (2013)
27. H. Holma, A. Toskala, *WCDMA for UMTS: HSPA Evolution and LTE*. Wiley, New York (2010)

Chapter 4
System Level Modeling for Tunable Components

As shown in the previous chapter, the response over the complete frequency range presents different amplitude values derived from the variation in the impedance matching at discrete frequencies. Ideally, a wide impedance matching in the considered frequency range is desired to hold a certain quality of signal at all operation bands. However, fundamental limitations indicate that in order to obtain a perfect impedance matching, a reduction of the available bandwidth is present at a certain frequency. As a result, the matching requires to be adapted by finding a compromise considering the minimum tolerance on the magnitude of the input reflection over the prescribed frequency [1, 2]. As shown in Fig. 4.1 this improvement can be realized by employing tunable components to dynamically cover a frequency range, to reduce the noise of diverse sources of distortion and to improve the impedance matching at an operation frequency considering a narrowband signal.

In practice, to reach the maximum bandwidth efficiency of a determined radio an improved signal path is required at the frequency range of interest, e.g. proper amplification, matching networks, and filters, to guarantee a certain level of signal quality. Furthermore, in real scenarios, portable devices are subject to different sources of distortion, which lead to a change of their input impedance. Consequently, the input impedance of the antenna becomes dependent on the operating frequency, the input power and the surrounding environment, $Z_{\mathrm{Ant}}(f, P_{\mathrm{in}}, \text{environment})$ [3, 4]. In this way, the performance of the device itself is affected in terms of rejection to interference, supported bandwidth, as well as battery lifetime.

The scope of this chapter is the modeling and evaluation performance of agile components that compose a reconfigurable system architecture. This analysis is realized in terms of analog measures, such as the scattering parameters, and digital measures, for instance, the Bit Error Rate (BER) and the Error Vector Magnitude (EVM). Due to reconfiguration of a microwave tunable component, consideration of group delay variations can lead not only to provide a proper functionality in the RF chain, but also

E. Gonzalez Rodriguez, *Reconfigurable Transceiver Architecture for Multiband RF-Frontends*, Smart Sensors, Measurement and Instrumentation 17,
DOI 10.1007/978-3-319-24581-2_4

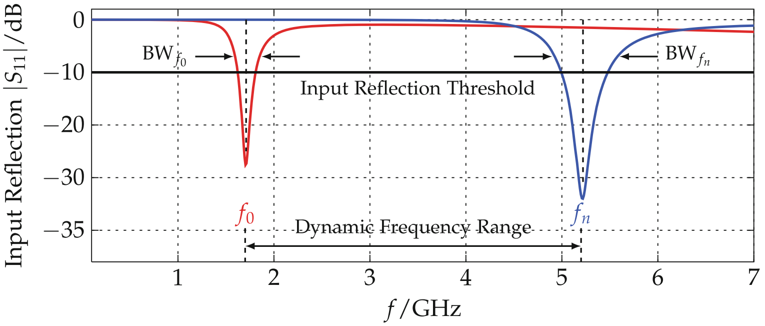

Fig. 4.1 Input reflection covering a dynamic frequency range employing tunable components over a continuous spectrum of frequencies

to ensure the best achievable performance of a single component in the RF chain. Such is the case of a tunable impedance matching network (TMN), when it fixes the emerging mismatch of the antenna in the RF-Frontend of a transceiver at a defined frequency of operation.

4.1 Effects of Nonlinear Phase and Group Delay Variations

An enhancement of the same communication system, e.g. a handheld device, can be achieved by proper adjustment and tuning of those components with the strongest influence on the quality of a signal. The signal path represented in Fig. 4.2 shows a typical receiver architecture and an architecture employing tunable components. The typical architecture consists of RF components such as antenna, matching network, low noise amplifier (LNA), filter, mixer and voltage controlled oscillator (VCO) via IF filter and D/A converter down to the digital baseband to perform an analysis in terms of digital measures, such as BER and EVM. In this case, a single digital analysis is performed to identify the quality of a signal. However, this kind of analysis is suitable for architectures employing components designed for operation at single frequencies or within a determined range without any reconfiguration properties.

Compared to the typical RF chain, the reconfigurable chain shows an architecture based on tunable components where a multiple digital analysis is necessary to identify a required performance while tuning. That is, the Bit Error Rate performance of each component in the signal path can be investigated. This leads to perform a jointly analog and digital analysis of each component to recognize how inherent nonlinear effects employing tunable components gradually influence their overall performance, and thus, in a system. In this way, possible improvement of the component's performance, as well as sources of error or distortion in the signal path can be identified. Hence, the quality of the signal, represented in terms of the scattering parameters, and digital measures, e.g. BER and EVM, can be quantified and

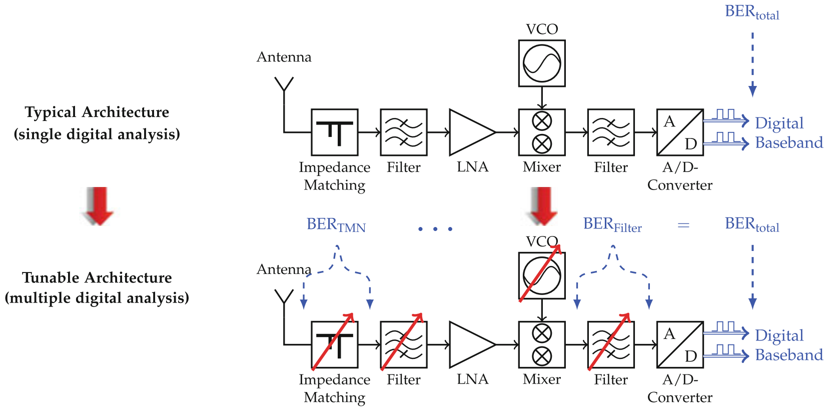

Fig. 4.2 *Typical receiver architecture* of an RF-Frontend with different components. Single digital performance analysis of the communication system to determine the signal quality. *Reconfigurable receiver architecture* of an RF-Frontend employing tunable components. Multiple digital performance analysis of the communication system to determine the signal quality at a component level

evaluated to perform a correction or enhancement of every single component in the transceiver chain.

Among the most important factors dealing with digital phase modulation schemes, group delay variations take an important place regarding BER degradation and the influence on the EVM [5–10]. To acquire reliable results in terms of these measures when the component is tuned to reconfigure its characteristics, it is important to evaluate a response considering the degree of dispersion.[1] This dispersion is characterized considering the transmission parameter S_{21} within the available bandwidth at an RF operation frequency f_c. In this way, the impact of the ripples and tilting in the amplitude response and phase can be evaluated, and therefore, the behavior of the component as well as the influence on the overall system can be recognized and improved.

An important measure to define and ensure the quality of a signal are the variations in the phase response of an RF component in terms of analog and digital measures. When a component is reconfigured or tuned into another state, e.g. to achieve a required level of the reflection parameter S_{11} at a certain frequency of operation, changes in the amplitude and phase of the transmission parameter S_{21} also appear. As a consequence of this dispersion, effects in the group delay response can be represented in different ways. First by analyzing the magnitude and phase of the forward transmission parameter S_{21}, and finally by performing an evaluation of the digital measures BER and EVM.

---

[1] The effect of a frequency response is considered dispersive when the frequency and the phase are not linearly connected, e.g. by the phase velocity of the wave $v = \frac{\omega}{k} = \frac{1}{\sqrt{\mu\varepsilon}}$ [11].

In practice, the response of every component in a system can distort the information of a signal. Most likely, the influence shown by the magnitude response in a 2-port network is more obvious to recognize than that of the phase response, e.g. by the losses included in the forward transmission parameter. To investigate the effect of phase dispersion of a component, e.g. an arbitrary filter with transfer function $H(j\omega)$, an excitation composed by the sum of two cosinusoidal responses of the form

$$x(t) = A_1 \cos(\omega_0 t) + A_2 \cos[(\omega_0 + \Delta\omega)t], \tag{4.1}$$

with frequencies $\Delta\omega \ll \omega_0$ can be considered at its input. As a result, after applying a few mathematical steps described in detail in Appendix A.1, to express the change of the phase in terms of the frequency at ω_0 and $\omega_0 + \Delta\omega$, the filter output can be written as

$$\begin{aligned} y(t) = {} & A_1 |H(j\omega_0)| \cos\left\{\omega_0 \left[t + \frac{\theta(\omega_0)}{\omega_0}\right]\right\} \\ & + A_2 |H[j(\omega_0 + \Delta\omega)]| \cos\left\{(\omega_0 + \Delta\omega)\left[t + \frac{\theta(\omega_0)}{\omega_0} + \tau_T\right]\right\}, \end{aligned} \tag{4.2}$$

where the overall delay τ_T in terms of the frequency change

$$\tau_T = \frac{\Delta\omega}{\omega_0} \cdot \left(\frac{\partial\theta(\omega_0)}{\partial\omega_0} - \frac{\theta(\omega_0)}{\omega_0}\right) \tag{4.3}$$

includes the phase delay and group delay

$$\tau_{\mathrm{p}} = \frac{\theta(\omega_0)}{\omega_0}, \tag{4.4}$$

$$\tau_{\mathrm{g}} = \frac{\partial\theta(\omega_0)}{\omega_0}, \tag{4.5}$$

correspondingly.

This means, on the one hand, that when the delay term $\tau_T = 0$, the filter's output at frequencies ω_0 and $\omega_0 + \Delta\omega$ is constantly delayed in time by $\frac{\theta(\omega_0)}{\omega_0}$, i.e. the output signal $y(t)$ is a delayed replica of the input signal $x(t)$. And on the other, that when the delay term $\tau_T \neq 0$, the filter's output at frequencies ω_0 and $\omega_0 + \Delta\omega$ is differently shifted, thus, resulting in a phase distortion, and consequently, in the group delay of the signal.

It is well known, that the group delay varies in accordance with the characteristic frequency response, e.g. in the phase parameter $\angle S_{21}$ of a 2-port network. Ideally, if the phase of a device shows linear behavior over frequency, the group delay

$$\tau_{\mathrm{g}}(f) = \frac{\partial \angle S_{21}}{\partial f}, \tag{4.6}$$

which represents the change of the forward transmission phase compared to the change of the frequency, would not have any influence on the transmission of pulses over the required passband. Nevertheless, most devices exhibit a dispersive behavior with a non-constant group delay.

As previously shown, signals with different frequencies exhibit different arrival times when nonlinearity of the phase response is present. Therefore, more errors in the reception of data arise due to the overlapping of energy associated with different symbols that might cause a false detection. In that way, when a signal with a defined bandwidth is transmitted or received, the group delay response depends on the response of every component in the RF signal path. Thus, considering a component within an RF chain of a frontend, the overall variation in the group delay parameter $\tau_{\mathrm{g}}(f)$ of the phase $\angle S_{21}$ with respect to its mean value $\mu[\tau_{\mathrm{g}}(f)]$ averaged across the signal bandwidth $\mathrm{BW}_{\mathrm{RF}}$ can be described by

$$S_{\tau_{\mathrm{g}}} = \int_{\mathrm{BW}} \left|\tau_{\mathrm{g}}(f) - \mu[\tau_{\mathrm{g}}(f)]\right| \mathrm{d}f. \tag{4.7}$$

This means, that a minimum zero value indicates a nondispersive behavior, and positive values indicate the degree of dispersion in the component.

To evaluate this variation, in the following sections the influence of the group delay is shown considering previous analysis. This analysis relates analog measures such as the S-parameters, and digital measures such as BER and EVM, with the dispersion introduced by a microwave component.

Throughout this investigation, evaluation of the BER for theoretic comparison with different digital modulation schemes, and EVM for comparison with current mobile standards, are taken into account. Thus, this nonlinearity is first introduced by a BER comparison between a flat filter and a filter with ripples in the amplitude response at a center frequency f_{c} in Sect. 4.1.2. Finally, by a thorough investigation of a tunable matching network based on ferroelectric varactors, a tunability analysis based on the scattering parameters taking into account group delay variations is shown in Sects. 4.2.3 and 4.2.4. Furthermore, a comparison between different modulation schemes in terms of the influence on the BER and EVM is given.

4.1.1 System Level Analysis

To evaluate the group delay variations of single components, a system in the form of a testbed is designed considering the exhibited behavior of a scattering parameters network in terms of the BER and EVM. In the system under investigation, coherent modulation and demodulation of a transmitted QAM (Quadrature Amplitude Modulation) is considered. The QAM signal of the form [12]

$$s_i(t) = \sqrt{\frac{2}{T_s}} g_a(t) \cos(2\pi f_c t) + \sqrt{\frac{2}{T_s}} g_b(t) \cos(2\pi f_c t) \tag{4.8}$$

through an Additive White Gaussian Noise (AWGN) channel is used. At coordinates of the in-phase and quadrature components $a_i\sqrt{\varepsilon}$ and $b_i\sqrt{\varepsilon}$, with signal energy ε, g_a and g_b represent the ith message point. The complete setup is based on different digital modulation schemes under the influence of AWGN so that theoretical performance according to [13] can be used for comparison.

Different kinds of testbeds have been developed in recent years by means of simulations including theoretical models to represent the channel only. They are also used to evaluate new algorithms and robust techniques that may improve the overall performance of a communication system [14–18]. Nevertheless, only little attention has been given to the analysis and evaluation of tunable components that form a reconfigurable RF chain. An individual investigation of these elements is needed to show the impact in the overall system. Thus, the testbed developed in Matlab and Simulink is focused on the analysis of passive elements, such as filters and matching networks.

The communication system simulator shown in Fig. 4.3 links Matlab with Simulink to extend overall control over the proposed designed system by setting up: (i) the signal properties of the waveform, such as modulation scheme, signal bandwidth, gain control and determined center carrier frequency; (ii) the passive network in terms of its reference impedance along with scattering parameters for amplitude, phase linearity and group delay analysis as well as; (iii) the computation properties for Monte Carlo simulations in terms of the number of bits and errors at a defined SNR level, i.e. 1×10^7 and 1×10^4 correspondingly. Thus, a reliable comparison of the Bit Error Rate and Error Vector Magnitude is acquired.

In the aforementioned passive network block (DuT), located after the AWGN channel, simulated or measured scattering parameters of a characterized network are

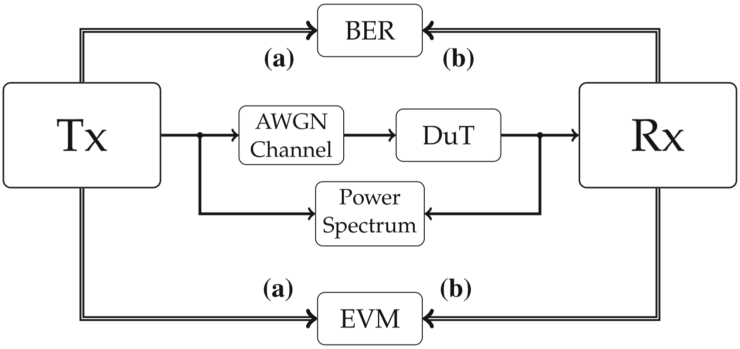

Fig. 4.3 Communication system simulator with passive matching network under investigation (DuT: Device under Test). The chain is modeled in Matlab and Simulink, including deembedded scattering parameter measurements of a TMN. (**a**) Reference signal, (**b**) recovered signal

included as a representation of the transmitter chain in the RF domain. For example, in the first case, to analyze scattering parameters of filters with different characteristics. And in the second case, scattering parameter measurements when a tunable matching network is biased at different voltages representing different matched impedances. Thus, the setup allows to include measured characteristics of an RF signal path and to perform simulations at selected frequencies.

A random signal with uniform distribution is used as a symbol generator, and data is sampled at a time T_{symbol} so that the sampling frequency f_s easily fulfills the Nyquist criteria. Baseband I/Q modulation process, signal power and phase compensation are modeled on the transmitter (Tx) side. The receiver side (Rx) focuses on the demodulation process. Deft handling synchronization of data between discrete reference signal and recovered signal is also carried out to ensure accurate BER and EVM values. That means, the number of samples by which the received data lags behind the transmitted data, is compensated to perform a correct computation of the results.

4.1.2 Microwave Characterization of RF-Filters

A quantitative evaluation of an RF filter characteristic at an operating frequency f_c can be performed based on the scattering parameters, e.g. of a 2-port network. Thus, two filters with a 3 dB-bandwidth of 36 MHz and $f_c = 1.5$ GHz are employed for analysis. The forward transmission S_{21} and input reflection S_{11} of a flat filter and a Chebyshev filter with an amplitude ripple of 0.5 dB are shown in Fig. 4.4.

Typically in an RF design, independent of the losses exhibited by the component, the magnitude response is optimized for a determined working frequency range or single frequency of operation with a defined bandwidth. Nevertheless, due to the behavior in the magnitude parameter $|S_{21}|$, a certain behavior also emerges in the

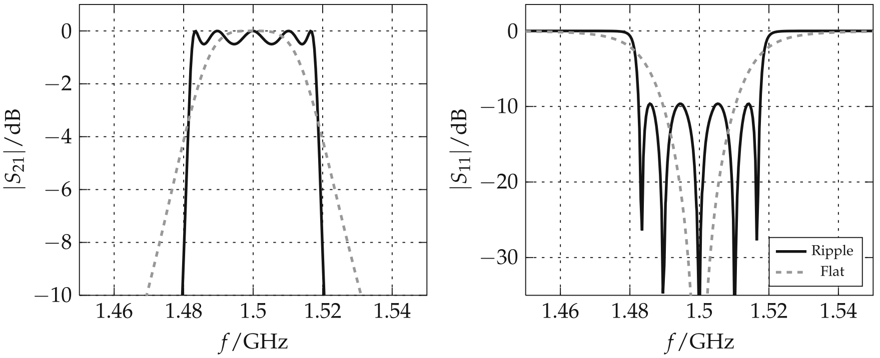

Fig. 4.4 Forward transmission and input reflection of filter with flat amplitude response and filter with a ripple of 0.5 dB

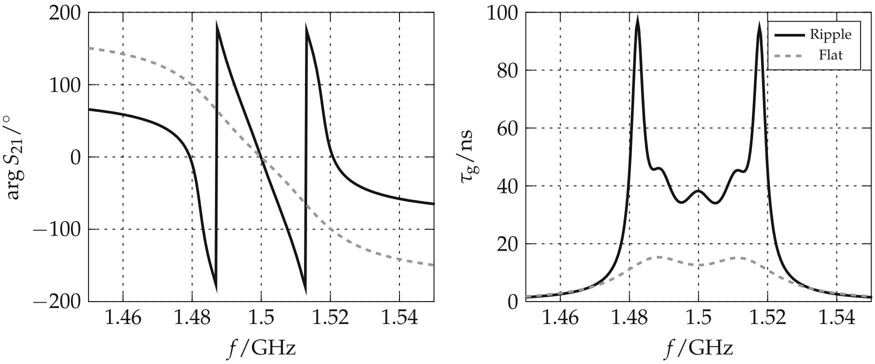

Fig. 4.5 S_{21} phase and group delay of filter with flat amplitude response and filter with a ripple of 0.5 dB

phase response $\angle S_{21}$, and as a consequence variations in the group delay $\tau_g(f)$ appear in the case of a nonlinear phase.

To exemplify this effect, in Fig. 4.5 the S_{21} phase parameter and group delay are shown. Regarding the group delay comparison, a smoother response with group delay values of 13 ns is exhibited by the flat filter, while the filter with ripples shows abrupt fluctuations around 36 ns at the frequency f_c. Furthermore, the comparison between the filters shows that the filter with a flat response encloses a smoother phase compared to the steeper response of the filter with ripples in the amplitude. Thus, resulting in a higher group delay at the passband of the center frequency at 1.5 GHz. Considering these responses, it is expected that the performance of the BER is affected by the filter with a higher group delay response.

4.1.3 Digital Performance of RF-Filters

In order to clearly demonstrate the effects in a communication system due to group delay variations, a digital performance evaluation of the filters response is given by taking into account the magnitude and phase of the transmission parameter S_{21} in terms of the BER for a 16-QAM modulation scheme.

To evaluate the difference in the group delay derived from the phase of the $\angle S_{21}$ parameter, an assessment of the BER performance is performed at the center frequency f_c. The considered RF bandwidth of the signal corresponds to 10 MHz. In that way, only the influence over the BER of the amplitude, phase, and group delay is ensured without being affected by the roll-off filter response at the −3 dB corner frequencies of the overall 36 MHz RF passband.

In Fig. 4.6, the BER comparison for a 16-QAM scheme between the flat filter and filter with ripples in relation to different SNR values is shown. The dashed curve represents the ideal behavior of the digital modulation scheme, and is employed to verify the validity of the computed results according to the developed testbed. It can

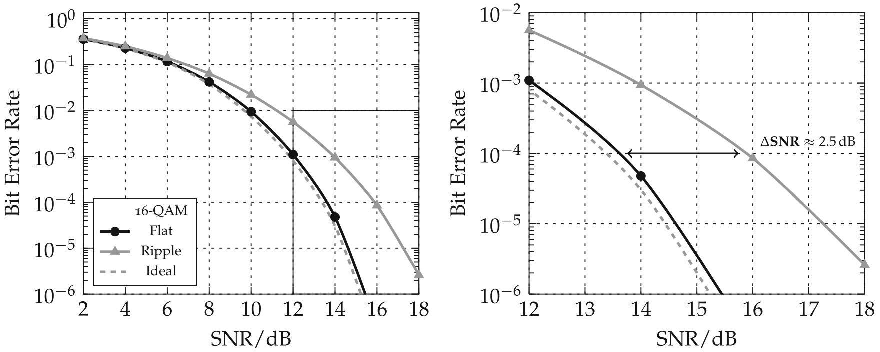

Fig. 4.6 16-QAM BER comparison of flat filter and filter with ripples of 0.5 dB in the amplitude response. The filter with a flat amplitude outperforms the results of the filter with ripples due to the influence of group delay variations around $f_c = 1.5\,\text{GHz}$. *Left* BER comparison of both filters. *Right* Exploded view of the marked area in the BER comparison

Table 4.1 Comparison between flat filter and filter with ripples at the center frequency $f_c = 1.5\,\text{GHz}$ in terms of group delay and BER at an SNR of 14 dB

Filter	S_{τ_g}	$\text{BER}_{14\,\text{dB}}$
Flat	0.81×10^{-3}	4.7×10^{-5}
Ripple	3.41×10^{-3}	9.41×10^{-4}

be seen that the flat filter clearly outperforms the behavior of the Chebyshev filter. While the BER results at 1×10^{-3} have a difference $\Delta\text{SNR} \approx 2\,\text{dB}$, this difference increases to a value of around 3 dB for BER values at a level of 1×10^{-6}.

By simple inspection of the group delay behavior in Fig. 4.5, it can be seen that the error probability of the flat filter is smaller and rather constant than that of the filter with ripples around the center frequency $f_c = 1.5\,\text{GHz}$. Thus, as a consequence of this effect, degradation of the BER is present.

To compare the performance of the flat filter and filter with ripples in terms of an SNR level of 14 dB, in Table 4.1 BER values as well as their corresponding overall group delay variation S_{τ_g} are given. Due to the difference of the group delay variation between both filters of around $\Delta S_{\tau_g} \approx 2.5 \times 10^{-3}$, a remarkable difference in the BER results of almost 1×10^{-3} is exhibited. Consequently, if the filter with ripples is employed instead of the filter with a flat amplitude response, the system would require to increase the SNR by at least 2.5 dB for BERs higher than 1×10^{-4}. Further comparison can be seen in real scenarios, for example in satellite communication systems, where the received signal level is reduced below a specified threshold value. This threshold values, also known as fade margin, can vary depending on different characteristics (effects of rain attenuation, multipath fading, operation band). Typical values for comparison can be found from 10 to 15 dB considering BERs of at least 1×10^{-3}, hence, such imperfections in the order of 3 dB can represent up to 30 % of the fade margin in a satellite receiver [19].

4.2 Ferroelectric Tunable Matching Network

Among other characteristics, tunable matching networks are implemented to adaptively compensate the emerging mismatch caused by operating the mobile device under changing conditions, e.g. position of the mobile phone, surrounding material, proximity to human body or to metallic structures. This reconfiguration can be performed at a fixed operation frequency performing a fine tuning to adjust a required input matching. Tunable matching networks can also operate at different operation frequencies satisfying a defined matching condition. Thus, the performance of this component is critical to hold a certain signal quality, and therefore, to maximize the total efficiency of the user equipment [20].

During the last years, a variety of materials and processing techniques have been applied to realize these kind of agile components that enable flexible radios and reconfigurable architectures. In this work, due to some of its main characteristics, such as low power consumption, fast tuning and high linearity, i.e. low intermodulation distortions compared to other technologies [21], a ferroelectric tunable matching network is considered for analysis.

4.2.1 Microwave Characterization of Tunable Matching Networks

It is well known that a matching network adapts, e.g. the impedance of the antenna at the input port of a mobile device, in the best case, to an impedance value of $50\,\Omega$, otherwise the signal is reflected back without being able to be transmitted or received. However, when a tunable matching network is designed at certain operation frequency or frequency range, a great amount of tuning states can satisfy a required matching level of the input reflection, e.g. $|S_{11}| \leq -10\,\text{dB}$. Consequently, to exploit the best performance of the antenna together with the tunable matching network, an analysis of the tunability in terms of digital measures, e.g. BER and EVM, is required based on a microwave characterization to identify and guarantee the most suitable tuning state.

Ferroelectric material can be employed to form a varactor, where permittivity, and hence the capacitance, change by applying an external electrostatic field, i.e. a biasing voltage. A tunable matching network, from [22, 23], composed of a pair of interdigital capacitors built on ferroelectric BST thick-film is shown in Fig. 4.7.

The BST layer shows a loss tangent of $\tan\delta \leq 0.02$ around 2 GHz and relative permittivity of $\varepsilon_\mathrm{r} = 410$ in the untuned state. Highly narrow resistive strips made of indium-tin-oxide are used for integrated DC-RF bias decoupling [23]. The TMN module shown in Fig. 4.7 is based on BST thick-film varactors in series and consists of RF input/output, two DC controls for each capacitor (C_1 and C_2), and an external shunt inductor connected to the central pad of the varactor module.

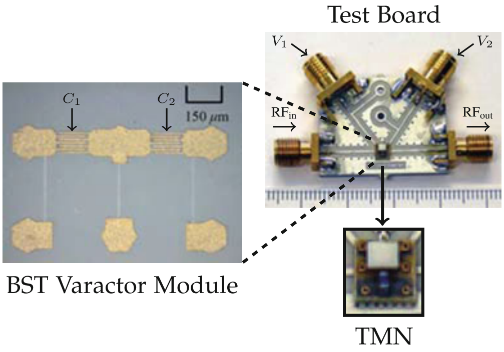

Fig. 4.7 *Left* varactor pair on BST thick-film ceramics [23]. *Right* tunable impedance matching network in the center of a test board [22]

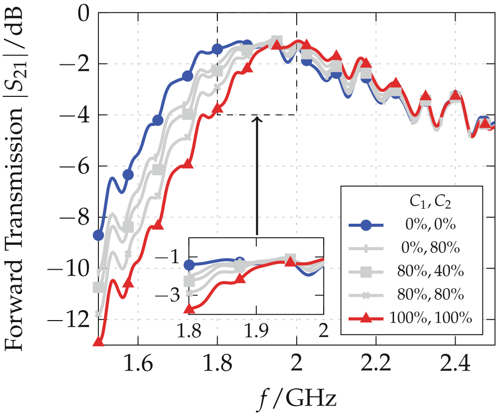

Fig. 4.8 Measured forward transmission of the TMN module for different capacitance values biased from 0 to 90 V, i.e. from untuned to maximum tuned state [22]

To address the analysis in terms of the tunability exhibited by the scattering parameters, Figs. 4.8 and 4.9 show the measured magnitude of the transmission parameter and input reflection parameter for different tuning voltages, respectively [22]. In that way, scattering parameters of the TMN with a 50 Ω environment at the input and output port of the module were measured each time after applying a DC biasing voltage to the BST varactors. In this case the biasing voltage range lies between 0 V to 90 V for each varactor. Thus, by setting a combination of voltages in both varactors, different tuning states satisfy a matching condition. For example, when both varactors are set in the untuned state at 0 V, the input reflection notch is located at around 1.8 GHz, and when the voltage is increased up to 90 V, the notch is tuned at around 1.9 GHz.

In Fig. 4.8 a rather constant $|S_{21}|$ parameter over all tuning states with a maximum insertion loss of less than −1.2 dB at 1.9 GHz is shown. The maximum variation of the insertion loss between tuning states at the center frequency is only 0.2 dB.

Measurement results of $|S_{11}|$ with a return loss of less than −11.5 dB across the tuning range from 1.8 to 2.0 GHz are shown in Fig. 4.9. This result can be compared to the typical requirement of $|S_{11}| \leq -10$ dB in mobile standards, such as GSM,

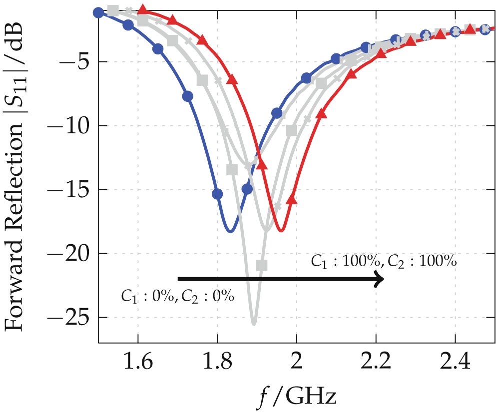

Fig. 4.9 Measured input reflection of the TMN module for different capacitance values biased from 0 to 90 V, i.e. from untuned to maximum tuned state [22]

UMTS and LTE for this frequency operation range, nevertheless, this value can vary depending on the required service or application, e.g. with a less restricted −6 dB value using bluetooth wireless technology [24, 25]. The Q-factor of the varactors at the target frequency is around 60. The varactors are biased from 0 V (0 %) to 90 V (100 %), covering a capacitance range from 0.31 pF to 0.22 pF respectively, thus, achieving a tunability of $\tau_{\mathrm{BST}} = 40\,\%$. The tunability is defined as the capacitance change divided by the maximum value in the untuned state.

4.2.2 Group Delay Variations of Tunable Matching Networks

Adaptive matching considering a required bandwidth and an agile modulation scheme selection are important requirements in reconfigurable architectures. Electrically tunable matching networks in the antenna of an RF-Frontend can overcome this necessity. Thus, enabling the same hardware module to fit efficiently into another service of different characteristics. However, due to the tunability, the dispersion of the passive network becomes obvious when the phase of the component is analyzed for different applied biasing voltages that adapt Z_{L} impedance values with an acceptable input matching.

Hence, to achieve maximum efficiency of the system, the effect of group delay variations has to be considered since different varactor tuning states can lead to different BER and EVM performance in spite of the fulfillment of the matching condition $|S_{11}| \leq -10\,\mathrm{dB}$ at the input of the antenna.

In Fig. 4.10 the corresponding phase parameter $\angle S_{21}$ of the TMN is given. From the untuned state to the tuned state, i.e. when the varactors are biased from 0 V (0 %) to 90 V (100 %), a gradual increment in the phase parameter of about 35° is observed. Nevertheless, the slightly different slope of each response raises group delay variations for each state in the TMN.

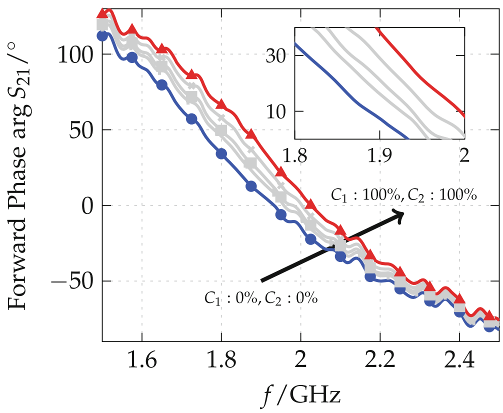

Fig. 4.10 Forward transmission phase measurement of the TMN module. Exhibited phase difference from the untuned state to tuned state of more than 30° at an operation frequency $f_c = 1.9\,\text{GHz}$

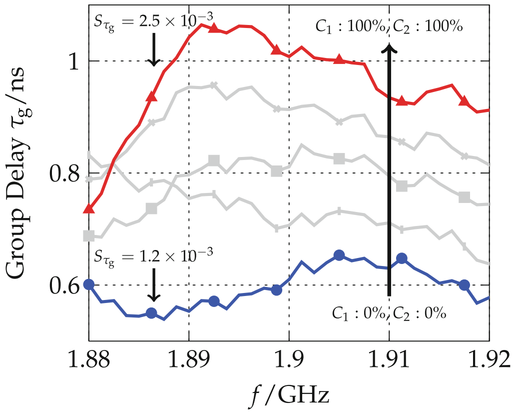

Fig. 4.11 Group delay of forward transmission phase of the TMN module within a frequency range of 40 MHz considering tunability of the varactors from 0 V (0 %) to 90 V (100 %) with corresponding group delay variation S_{τ_g}

In Fig. 4.11, group delay responses are shown for each tuning state across a signal bandwidth of up to 40 MHz. The magnitude of the group delay variation S_{τ_g} increases gradually from 1.2×10^{-3} to 2.5×10^{-3} while the biasing of the matching network increases from 0 to 90 V. Thus, exhibiting different overall group delay responses from one to another state. This group delay variation described in (4.7), has shown a considerable difference of almost 3 dB by evaluating different kind of filters in terms of the BER. However, the overall group delay variation and the influence on the BER depend also on factors such as modulation scheme and signal bandwidth. In effect, to investigate this influence in a TMN, the analysis requires to be extended regarding the evaluation of different biasing voltages that satisfy a matching condition of at least $|S_{11}| = -10\,\text{dB}$. This is also supported by digital modulation schemes with RF signal bandwidths that are considered for current mobile standards.

Likewise in Sect. 4.1.1 considering the analysis of filters, in the system under investigation, coherent modulation and demodulation of a transmitted QAM signal is taken into account. In this case, different orders of the quadrature amplitude scheme are analyzed, i.e. QPSK (Quadrature Phase Shift Keying), 16-QAM and 64-QAM digital modulation schemes. Signals with two different RF bandwidths are analyzed, $\mathrm{BW_{RF}} = 20\,\mathrm{MHz}$ and $\mathrm{BW_{RF}} = 40\,\mathrm{MHz}$. It is worth mentioning, that one of the key parts of this setup resides in the passive network module. In this module scattering parameters can be read out at a desired carrier frequency and defined tuning state that represent a different matching condition. Thus, signals with different characteristics in terms of bandwidth and modulation scheme can be efficiently processed to determine if reconfiguration is required of the tunable component or the system.

In the following Sects. 4.2.3 and 4.2.4, the BER and EVM analysis considers the tunability of the introduced matching network. Based on previous analysis considering group delay variations, a higher influence on the BER and EVM analysis is predicted when the characteristics of the proposed system are also increased. Such is the case of modulation schemes with higher order and wider RF signal bandwidth.

4.2.3 Influence on Bit Error Rate

Modulation schemes with high spectral efficiency are more vulnerable to system imperfections, arousing other transmission impairments, e.g. intermodulation distortion, echo or crosstalk [26–28]. Hence, in order to clearly show an influence of group delay on the transmitter side of a reconfigurable frontend, QAM schemes with a different order have been chosen for evaluation.

To obtain BER performances of the TMN module considering tuning states that satisfy a matching condition $|S_{11} \leq -10\,\mathrm{dB}|$, RF signals are evaluated through the matching circuit for different SNR levels. Since tunability of the varactors has shown the best input reflection at a center carrier frequency $f_\mathrm{c} = 1.9\,\mathrm{GHz}$, this frequency is considered for investigation. Two RF signal bandwidths taking into account group delay variations have been chosen for evaluation. $\mathrm{BW_{RF}} = 20\,\mathrm{MHz}$ which is the maximum bandwidth in LTE for single carrier mode, and $\mathrm{BW_{RF}} = 40\,\mathrm{MHz}$ as an exemplification of future implementations for carrier aggregation mode [29].[2] As a representation of the overall tuning range of the TMN module, combinations of the varactor biasing voltages (C_1, C_2) are selected in the following form: $(0\,\mathrm{V}, 0\,\mathrm{V})$, $(0\,\mathrm{V}, 72\,\mathrm{V})$, $(72\,\mathrm{V}, 36\,\mathrm{V})$, $(72\,\mathrm{V}, 72\,\mathrm{V})$, and $(90\,\mathrm{V}, 90\,\mathrm{V})$. Hence, they represent a matched impedance Z_L state in the TMN considering the tuning range of the varactors at a frequency f_c. Furthermore, different modulation schemes with different spectral efficiency are evaluated for comparison, i.e. QPSK, 16-QAM and 64-QAM. Typically, raw BER values around 1×10^{-2} and 1×10^{-5} are typically considered for a quasi-error free transmission without applying any forward error correction. However, these values can vary since they depend on the type of service,

---

[2] Up to five carriers with a bandwidth of up to 20 MHz each can be aggregated in LTE-Advanced. Furthermore, data rates of the order of 1 Gbps might theoretically be achieved using contiguous bandwidths of 40 MHz or more [29].

e.g. video, voice or data. Furthermore, a gray coded constellation for BER and EVM calculations is employed according to different standards, such as IEEE 802.11 and HiperLAN/2 [30, 31].

QPSK Modulation Scheme

In Fig. 4.12 the BER results of selected tuning states for a QPSK modulation scheme are shown. Comparison with the theoretical or ideal case, i.e. considering only the effect of the AWGN channel, shows an influence of 0.4 dB only over the analysis for all tuning states with $\mathrm{BW_{RF}} = 20\,\mathrm{MHz}$. In the case of $\mathrm{BW_{RF}} = 40\,\mathrm{MHz}$, a difference of around 0.8 dB is exhibited compared to the initial tuning state (C_1 : 0 %, C_2 : 0 %) at a BER of 1×10^{-6}.

Considering the tunability of the matching network, the analysis of different tuning cases shows practically the same performance when the overall set of impedances tuned from (C_1 : 0 %, C_2 : 0 %) to (C_1 : 100 %, C_2 : 100 %) are evaluated with the signal bandwidth $\mathrm{BW_{RF}} = 20\,\mathrm{MHz}$. However, a difference of less than 0.5 dB is present when the whole set of tuning cases is compared for different signal bandwidths, i.e. $\mathrm{BW_{RF}} = 20\,\mathrm{MHz}$ and $\mathrm{BW_{RF}} = 40\,\mathrm{MHz}$.

The small variation between different tuning states presented in the BER for the QPSK scheme is due to the low number of bits per symbol. For higher order schemes, however, this variation increases. In the case of a 16-QAM, for example, instead of having a quadrant containing four possible symbols, QPSK includes just one. Thus, because of the large distance between the symbols in the constellation diagram, this influence is not as pronounced as in the following modulation schemes. Furthermore,

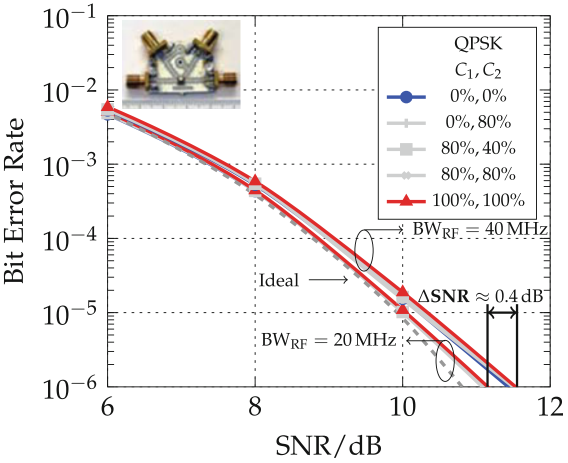

Fig. 4.12 BER comparison of different voltage tuning states for two RF signal bandwidth cases taking into account a QPSK modulation scheme. Corresponding voltage tuning states in percentage: 0 % = 0 V, 40 % = 36 V, 80 % = 72 V, 100 % = 90 V

in spite of practically same values of BER for different tuning states considering the same signal bandwidth, results for each case still exhibit the influence described by the group delay.

16-QAM Modulation Scheme

Compared to a QPSK scheme, results considering a 16-QAM scheme show a stronger difference when different tuning voltages are applied and different RF signal bandwidths are considered. A thorough analysis is therefore required to understand the behavior of the tunability in the matching network. Figure 4.13 shows a comparison of the BER in relation to the SNR for different voltage tuning states and two RF signal bandwidths, $\mathrm{BW_{RF}} = 20\,\mathrm{MHz}$ and $\mathrm{BW_{RF}} = 40\,\mathrm{MHz}$, in a 16-QAM modulation scheme. The difference compared to the ideal case for $\mathrm{BW_{RF}} = 20\,\mathrm{MHz}$ is of around 0.4 dB, however, for $\mathrm{BW_{RF}} = 40\,\mathrm{MHz}$ this difference increases to around 1 dB considering the initial tuning state $(C_1 : 0\,\%, C_2 : 0\,\%)$. Regarding the tunability performance between different signal bandwidths, a maximum difference of 1 dB is present at $\mathrm{BER} = 1 \times 10^{-3}$ and up to 2 dB at $\mathrm{BER} = 1 \times 10^{-6}$.

For the case of a signal with $\mathrm{BW_{RF}} = 20\,\mathrm{MHz}$, the exhibited difference between tuning states is about $\Delta\mathrm{SNR} < 0.2\,\mathrm{dB}$ for a BER of 1×10^{-6}. Influence of the group delay over the BER considering the different tuning voltages is less pronounced compared to the 40 MHz case.

In Fig. 4.14 an exploded view of the marked area of Fig. 4.13 for a signal with $\mathrm{BW_{RF}} = 40\,\mathrm{MHz}$ is shown. Simulation results show that for values around 1×10^{-4}, a difference of around 0.5 dB is obtained in terms of SNR between the minimum and maximum applied tuning voltage. Considering a better BER performance around 1×10^{-6}, the difference in the SNR increases to more than 1 dB.

As shown in Fig. 4.9, in spite of different magnitude values of the forward reflection parameter, all of them with $|S_{11}| < -11.5\,\mathrm{dB}$, BER results exhibit a depen-

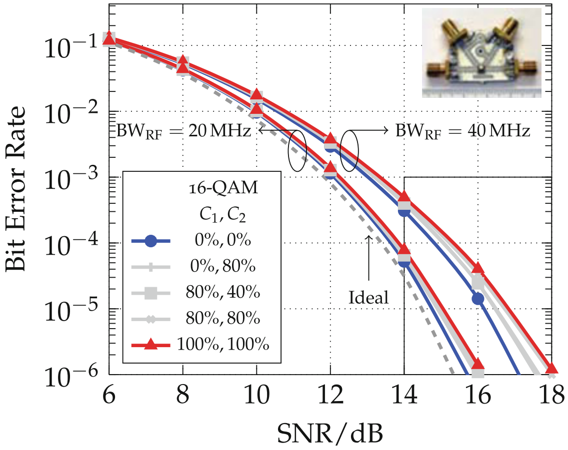

Fig. 4.13 BER comparison of different voltage tuning states for two RF signal bandwidth cases taking into account a 16-QAM scheme

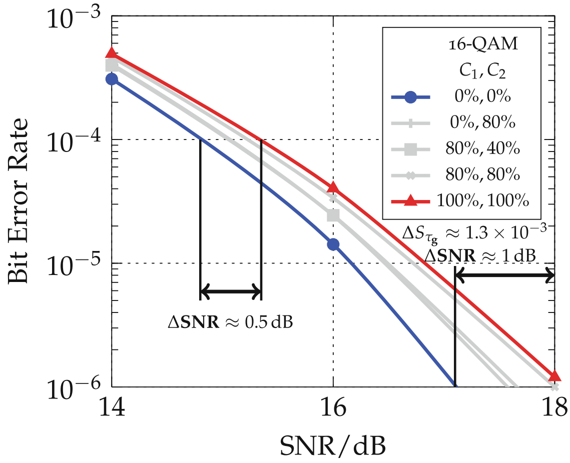

Fig. 4.14 BER exploded view of the marked area in Fig. 4.13 for a signal with $\mathrm{BW_{RF}} = 40\,\mathrm{MHz}$ taking into account a 16-QAM scheme

dency on the group delay variation presented due to the change over the phase parameter $\angle S_{21}$.

As a result of the analysis taking into account the BER and scattering parameters of the passive network, the distortion of the waveform due to a group delay variation around a frequency of operation f_c obeys the behavior described by Eq. 4.7. In other words, for a stronger nonlinear phase, higher values of the group delay variation S_{τ_g} yield a degradation of the BER performance. An example of this can be seen for the two boundary DC voltages in the varactors of the matching circuit, i.e. at 0 V (0 %) and 90 V (100 %), where the largest phase difference is present as shown in Figs. 4.10 and 4.11. Hence, the relation between calculated BER and group delay becomes obvious when group delay variation S_{τ_g} values are compared for different tuning states of the TMN.

To highlight this influence, in the case of the signal with $\mathrm{BW_{RF}} = 40\,\mathrm{MHz}$, an overview of the parameter values is shown in Table 4.2. The numerical comparison of the BER for different tuning voltages considers scattering parameters at a center frequency $f_\mathrm{c} = 1.9\,\mathrm{GHz}$ and group delay variations. It is to observe that the forward transmission remains almost constant. In the case of the input reflection,

Table 4.2 Comparison of different tuned varactor voltages at $f_c = 1.9\,\mathrm{GHz}$ for a signal with $\mathrm{BW_{RF}} = 40\,\mathrm{MHz}$ taking into account a 16-QAM scheme

$(C_1, C_2)/\%$	$\lvert S_{11}\rvert/\,\mathrm{dB}$	$\lvert S_{21}\rvert/\,\mathrm{dB}$	S_{τ_g}	$\mathrm{BER}_{18\,\mathrm{dB}}$
(0, 0)	−12.29	−1.35	$\mathbf{1.2 \times 10^{-3}}$	$\mathbf{1.0 \times 10^{-7}}$
(0, 80)	−12.53	−1.30	1.4×10^{-3}	4.0×10^{-7}
(80, 40)	−24.36	−1.25	1.5×10^{-3}	5.0×10^{-7}
(80, 80)	−16.51	−1.30	1.8×10^{-3}	1.0×10^{-6}
(100, 100)	−11.65	−1.56	$\mathbf{2.5 \times 10^{-3}}$	$\mathbf{1.2 \times 10^{-6}}$

although different values are measured, all tuning states satisfy a good input matching better than -10 dB. However, although in both parameters, $|S_{21}|$ and $|S_{11}|$ a good performance is achieved, the influence of dispersion on the system performance in a matching network yields different BER performance. This difference has been shown its dependence on the group delay response over the RF signal bandwidth.

The difference in S_{τ_g} of about 1.3×10^{-3} degrades the BER from 1.0×10^{-7} to 1.2×10^{-6} for tuning voltages between (0 %, 0 %) and (100 %, 100 %) at SNR = 18 dB. This small but non negligible difference in the group delay has an impact of around 1 dB when SNR is evaluated for a BER = 1×10^{-6} in a 16-QAM scheme. In summary, an optimal adaptive matching should satisfy a good input reflection $|S_{11}| \leq -10$ dB considering also the effect of the phase in the transmission parameter S_{21}. This evaluation of group delay variations S_{τ_g} can ensure the best possible matching among the complete set of tuning states that satisfy a matching condition.

64-QAM Modulation Scheme

The BER analysis of the selected tuning states for a 64-QAM modulation scheme with different signal bandwidths is shown in Fig. 4.15. To obtain an acceptable performance in terms of the BER with an RF signal bandwidth $\text{BW}_{\text{RF}} = 40$ MHz for all the set of tuning voltages, comparable higher SNR values are required than for the case of a signal with $\text{BW}_{\text{RF}} = 20$ MHz. Fundamentally, the influence of the phase variation in the BER can still be described by the group delay analysis. This means that when the biasing voltage of the varactors is increased from 0 to 100 %, an increase in the variation of the group delay is present.

Compared to the ideal case, a higher difference in the SNR than in the other schemes is exhibited due to the increase of the bits per symbol. This modulation scheme is the only that shows BER results towards those when a matching condition $|S_{11}| \leq -10$ dB is not fulfilled. Such is the case of the response for a signal with RF bandwidth $\text{BW}_{\text{RF}} = 40$ MHz. For $\text{BW}_{\text{RF}} = 20$ MHz, while for BER = 1×10^{-2}

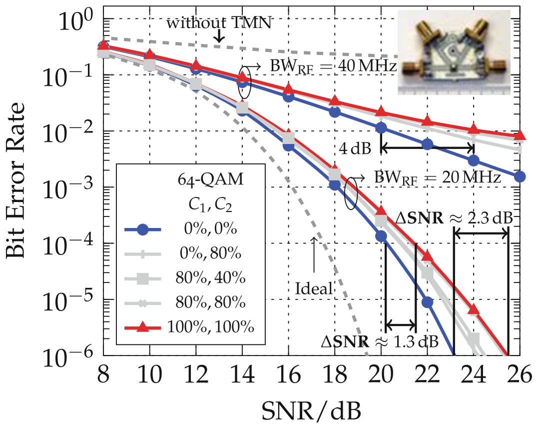

Fig. 4.15 BER comparison of different voltage tuning states for two RF signal bandwidth cases taking into account a 64-QAM modulation scheme

a maximum difference of 2 dB is present when a tuning state at (100 %, 100 %) is evaluated, a difference of almost 6 dB for a BER of 1×10^{-6} is computed.

Regarding only the tunability for the case of a signal with $\mathrm{BW}_{\mathrm{RF}} = 20$ MHz, it can be seen that at a BER $= 1.0 \times 10^{-4}$, the influence of the group delay dispersion between the $C_1 : 0\,\%, C_2 : 0\,\%$ and $C_1 : 100\,\%, C_2 : 100\,\%$ tuning states corresponds to a difference of 1.3 dB in terms of the SNR value, i.e. from 20.2 to 21.5 dB. If a better performance in terms of the BER is taken into account, the presented tuning states at a BER $= 1.0 \times 10^{-6}$ vary from each other due to the difference in the group delay, i.e. from 23.15 to 25.5 dB. By performing a group delay analysis of a set of matched impedances that fulfills the condition $|S_{11}| \leq -10$ dB, consequently shows, a difference of 2.3 dB between all tuning cases. In the case of $\mathrm{BW}_{\mathrm{RF}} = 40$ MHz at a BER $= 1.0 \times 10^{-2}$ this difference increases up to 4 dB.

Figure 4.16 shows an overview of all BER results. These results consider the set of all different voltage tuning states, as well as two different RF signal bandwidths $\mathrm{BW}_{\mathrm{RF}}$ with 20 and 40 MHz. As it can be seen from the three different modulation schemes (QPSK, 16-QAM and 64-QAM), the effect described in Sect. 4.2.2 caused by the frequency dispersion of the group delay for different tuning states of the impedance matching network is remarkable. Thus, when the spectral efficiency of the system at the receiver side is intended to be enhanced, a selection of the required tuning state considering group delay variations to satisfy a matching condition under changing conditions is required.

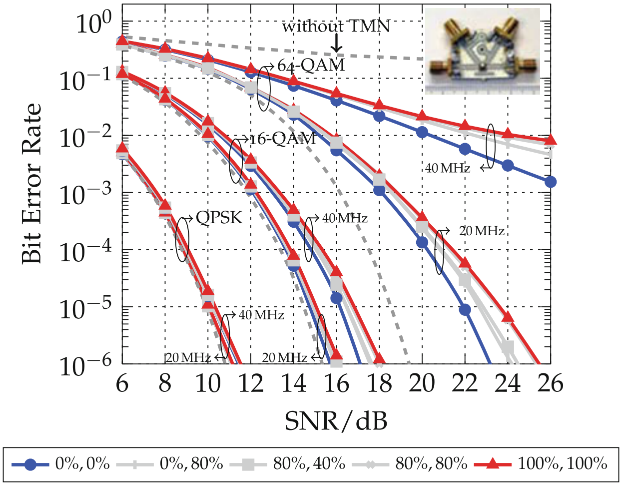

Fig. 4.16 BER comparison of different voltage tuning states for two RF signal bandwidth cases taking into account different modulation schemes; QPSK, 16-QAM and 64-QAM

4.2.4 Influence on Error Vector Magnitude

In practice, when the BER of the system exceeds defined thresholds, the given information cannot identify probable sources of signal distortion, such as the behavior of the symbols in the constellation diagram [32]. BER analysis is used to reach or to hold a certain level of signal quality in terms of power and noise in a communication system. Sources of distortion affecting a component or module in the whole system have been characterized in Sects. 4.2.2 and 4.2.3, i.e. in terms of additive noise, non-flat amplitude response, nonlinear phase response, group delay, RF bandwidth and modulation scheme. Hence, considering the In-phase and Quadrature components of a baseband signal in a constellation diagram, together with the aforementioned sources of distortion, evaluation of the matching network tunability is performed considering the Error Vector Magnitude.

Taking into account the computed BER performances exhibited by the characterized matching network, and once a defined threshold of an RF-Frontend architecture is reached with different digital modulation schemes e.g. QPSK, 16-QAM and 64-QAM, an EVM analysis of the same varactor tuning states (C_1, C_2) is performed. This analysis is carried out to assure a defined signal quality in terms of errors at the receiver side, by calculating how far the received bits are located from the ideal point in the constellation diagram. Furthermore, this analysis shows another way to verify that the best performance of the system is achieved, and to compare the results with those defined, e.g. by mobile standards.

Typically, the deviation of the transmitted reference signal to the received test signal, as shown in Fig. 4.17, is expressed as the percentage relative to the average transmitted power per symbol [33, 34] given by

$$\mathrm{EVM}_{\mathrm{rms}} = \sqrt{\frac{\sum_{i=1}^{N} |S_{\mathrm{ideal},i} - S_{\mathrm{meas},i}|^2}{\sum_{i=1}^{N} |S_{\mathrm{ideal},i}|^2}}, \tag{4.9}$$

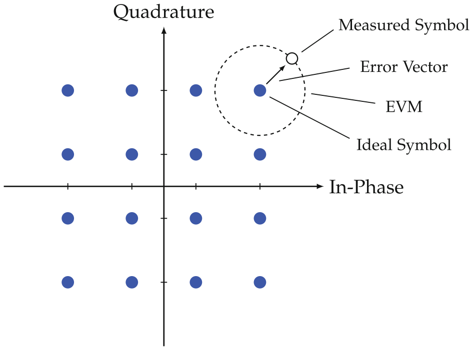

Fig. 4.17 IQ diagram for calculation of the Error Vector Magnitude. Transmitted reference signal: ideal constellation of a 16-QAM modulation scheme. Received test signal: measured symbol deviated from its origin vector

where S_{ideal} and S_{meas} represent the ideal and recovered ith symbols in the IQ plane, respectively. N represents the number of processed symbols in the constellation. And for a normalized constellation of i message points, thus, the error vector magnitude is defined as the root mean square $\mathrm{EVM_{rms}}$ that combines the error of the magnitude and phase of the In-phase and Quadrature components in the constellation diagram.

QPSK Modulation Scheme

Results in Fig. 4.18 and Table 4.3 of the QPSK modulation scheme are shown. In this case, a SNR level of 12 dB was selected for analysis giving BER results much smaller than 1×10^{-6}.

In Fig. 4.18, constellation diagrams are shown when the TMN is set for the initial tuning state $C_1 : 0\,\%$, $C_2 : 0\,\%$ with different signal bandwidths. It can be seen that the difference between both plots is almost negligible, $\mathrm{BW_{RF}} = 20\,\mathrm{MHz}$ (left) and $\mathrm{BW_{RF}} = 40\,\mathrm{MHz}$ (right). This difference can be numerically compared in Table 4.3 for the lowest ($C_1 : 0\,\%$, $C_2 : 0\,\%$) and the highest ($C_1 : 100\,\%$, $C_2 : 100\,\%$) applied biasing voltage to the varactors.

Results for either the lowest or the highest voltage present a difference of around 1.6 % in terms of the $\mathrm{EVM_{rms}}$ when the signal bandwidth $\mathrm{BW_{RF}}$ is switched.

16-QAM Modulation Scheme

Following a similar analysis as for the QPSK modulation scheme, results of the measured matching network tunability in terms of EVM analysis at different SNR

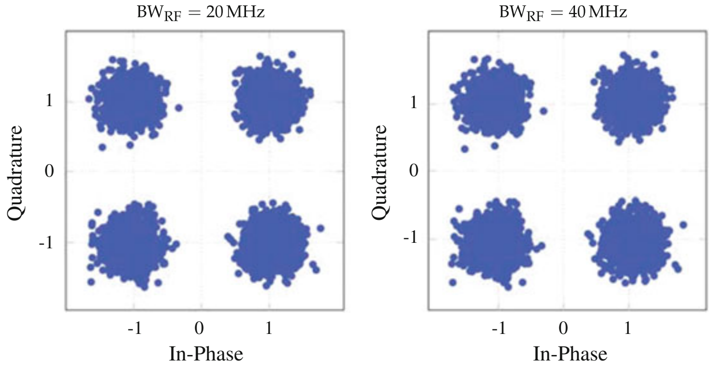

Fig. 4.18 QPSK modulation scheme. Scatter plots of voltage tuning values $C_1 : 0\,\%$, $C_2 : 0\,\%$ for $\mathrm{EVM_{rms}}$ and BER comparison with different signal bandwidths $\mathrm{BW_{RF}}$ values at SNR = 12 dB

Table 4.3 QPSK modulation scheme

QPSK	$\mathrm{BW_{RF}} = 20\,\mathrm{MHz}$		$\mathrm{BW_{RF}} = 40\,\mathrm{MHz}$	
$C_1 : C_2/\%$	0 : 0	100 : 100	0 : 0	100 : 100
$\mathrm{EVM_{rms}}/\%$	16.87	16.91	18.49	18.56
BER	1.3×10^{-7}	1.6×10^{-7}	3.3×10^{-7}	4.0×10^{-7}

Comparison of tuned varactor voltages for SNR = 12 dB with different signal bandwidths $\mathrm{BW_{RF}}$ at $f_c = 1.9\,\mathrm{GHz}$

values for a 16-QAM modulation scheme are analyzed. Required levels determined by different standards and technical specifications are taken into account for comparison [35–37].

In Fig. 4.19, constellation diagrams when the TMN is set for the initial tuning state $C_1 : 0\,\%$, $C_2 : 0\,\%$ are shown. Different SNR values (15 dB and 18 dB) and RF signal bandwidths (20 MHz and 40 MHz) of measured S-parameters at $f_c = 1.9\,\text{GHz}$ are evaluated. Considering the aforementioned specifications, all results exhibit an $\text{EVM}_{\text{rms}} < 13.5\,\%$ with BERs around 1×10^{-5}. In Table 4.4 the corresponding comparison of SNR = 15 dB and SNR = 18 dB for BER and EVM regarding the lowest ($C_1 : 0\,\%$, $C_2 : 0\,\%$) and the highest ($C_1 : 100\,\%$, $C_2 : 100\,\%$) biasing voltage applied to the varactors is shown.

Table 4.4 yields two types of comparisons between the corresponding tuning states for the scatter plots: (a) the comparison taking into account a SNR value with different signal bandwidths BW_{RF} (horizontally oriented); and (b) the comparison taking into account a signal bandwidth BW_{RF} with different SNR values (vertically oriented).

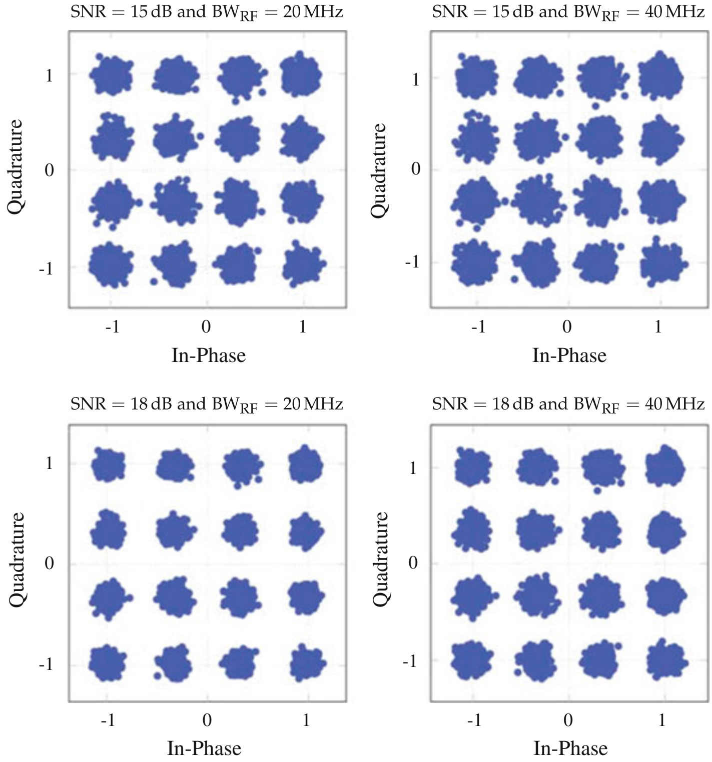

Fig. 4.19 16-QAM modulation scheme. Scatter plots of voltage tuning values $C_1 : 0\,\%$, $C_2 : 0\,\%$ for EVM_{rms} and BER comparison with different signal bandwidths BW_{RF} values at SNR = 15 dB and SNR = 18 dB

Table 4.4 16-QAM modulation scheme

16-QAM	$BW_{RF} = 20\,MHz$		$BW_{RF} = 40\,MHz$	
SNR = 15 dB				
$C_1 : C_2/\%$	0 : 0	100 : 100	0 : 0	100 : 100
$EVM_{rms}/\%$	9.82	9.99	12.19	12.41
BER	5.8×10^{-6}	1.3×10^{-5}	7.4×10^{-5}	1.6×10^{-4}
SNR = 18 dB				
$C_1 : C_2/\%$	0 : 0	100 : 100	0 : 0	100 : 100
$EVM_{rms}/\%$	7.73	7.97	10.49	10.78
BER	$<1.0 \times 10^{-7}$	$<1.0 \times 10^{-7}$	1.0×10^{-7}	1.2×10^{-6}

Comparison of tuned varactor voltages for different SNR values and signal bandwidths BW_{RF} at $f_c = 1.9\,GHz$

In the first case (a), difference in the EVM_{rms} for SNR = 15 dB is present, i.e. while for $BW_{RF} = 20\,MHz$ corresponds $EVM_{rms} = 9.82\,\%$, for $BW_{RF} = 40\,MHz$ corresponds $EVM_{rms} = 12.19\,\%$. In the latter case (b), comparing the same signal bandwidth $BW_{RF} = 20\,MHz$ and tuning state ($C_1 : 0\,\%, C_2 : 0\,\%$), $EVM_{rms} = 9.82\,\%$ for SNR = 15 dB is obtained compared to $EVM_{rms} = 7.73\,\%$ for SNR = 18 dB for $BW_{RF} = 40\,MHz$.

Due to the effect caused by the group delay and amplitude variations of the S_{21} parameter at the f_c carrier frequency, different results in terms of BER and EVM can be observed: (a) while the EVM_{rms} difference between tuning state values of the impedance matching network from $C_1 : 0\,\%, C_2 : 0\,\%$ to $C_1 : 100\,\%, C_2 : 100\,\%$ considering both modulation bandwidths is almost negligible; (b) the influence at a fixed SNR in terms of the BER notably increases by switching the modulation signal bandwidth, e.g. from 1.6×10^{-4} to 5.8×10^{-6} for SNR = 15 dB, and from 1.2×10^{-6} to a value much lower than $<1 \times 10^{-7}$ for SNR = 18 dB.

64-QAM Modulation Scheme

In Fig. 4.20 and Table 4.5 results of the 64-QAM modulation scheme are shown. Constellation diagrams are shown when the TMN is set for the initial tuning state voltage $C_1 : 0\,\%, C_2 : 0\,\%$ at a SNR of 22 dB with RF bandwidth $BW_{RF} = 20\,MHz$ (left) and $BW_{RF} = 40\,MHz$ (right).

For this modulation scheme, a notable difference can be observed when the signal bandwidth BW_{RF} is increased, yielding a significant BER degradation. A detailed comparison in terms of the EVM and BER is presented in Table 4.5. The difference in terms of the EVM_{rms} taking into account the same BW_{RF} varies by less than 0.4 %, as similarly shown in the other modulation schemes. Furthermore, the comparison between both bandwidths BW_{RF} for all tuning states results in a difference of less than 4 %.

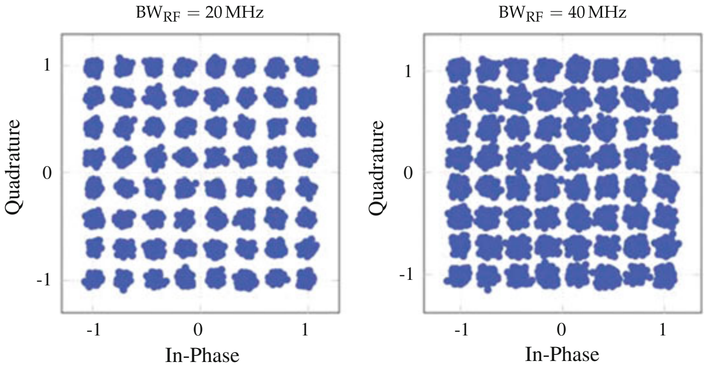

Fig. 4.20 64-QAM modulation scheme. Scatter plots of voltage tuning values $C_1 : 0\,\%$, $C_2 : 0\,\%$ for $\mathrm{EVM_{rms}}$ and BER comparison with different signal bandwidths $\mathrm{BW_{RF}}$ values at $\mathrm{SNR} = 22\,\mathrm{dB}$

Table 4.5 64-QAM modulation scheme

64-QAM	$\mathrm{BW_{RF}} = 20\,\mathrm{MHz}$		$\mathrm{BW_{RF}} = 40\,\mathrm{MHz}$	
$C_1 : C_2/\%$	0 : 0	100 : 100	0 : 0	100 : 100
$\mathrm{EVM_{rms}}/\%$	5.64	5.99	9.03	9.39
BER	8.9×10^{-6}	5.6×10^{-5}	5.7×10^{-3}	1.4×10^{-2}

Comparison of tuned varactor voltages for $\mathrm{SNR} = 22\,\mathrm{dB}$ with different signal bandwidths $\mathrm{BW_{RF}}$ at $f_c = 1.9\,\mathrm{GHz}$

Comparison Between Different Modulation Schemes

Taking into account the EVM requirement from different standards of current and upcoming technologies, such as UMTS and LTE [37, 38], a comparison for different digital modulation schemes is shown, i.e. for QPSK 18.5 %, for 16-QAM 13.5 % and for 64-QAM 9 %.

Considering the analyzed matching network, to provide a general performance of the complete set of voltage tuning states, the general EVM for a defined $\mathrm{BW_{RF}}$ and SNR can be calculated. The average over a number of single EVM measurements is defined, thus, by

$$\overline{\mathrm{EVM_{rms}}} = \sqrt{\frac{1}{\max\left(\gamma_{\mathrm{s},i}\right)} \sum_{i=1}^{\gamma_{\mathrm{s},i}} \mathrm{EVM}^2_{\mathrm{rms},i}}, \tag{4.10}$$

where $\mathrm{EVM}_{\mathrm{rms},i}$ is the corresponding EVM value of each tuning state γ_s in the TMN, i.e. the selected combinations of each varactor biasing voltages (C_1, C_2): (0 V, 0 V), (0 V, 72 V), (72 V, 36 V), (72 V, 72 V), and (90 V, 90 V).

In order to clearly show the behavior of the EVM while the SNR is increased, two cases were analyzed, i.e. $\mathrm{SNR} = 15\,\mathrm{dB}$ and $\mathrm{SNR} = 18\,\mathrm{dB}$, for the 16-QAM modulation scheme.

In the case of SNR $= 15\,\text{dB}$, both signal bandwidth BW_{RF} cases lie below the required standard $\text{EVM}_{\text{rms}} = 13.5\,\%$, i.e. for the $\text{BW}_{\text{RF}} = 20\,\text{MHz}$ case, an $\overline{\text{EVM}_{\text{rms}}}$ value of 9.98 % is obtained, and for the $\text{BW}_{\text{RF}} = 40\,\text{MHz}$ case, an $\overline{\text{EVM}_{\text{rms}}}$ value of 12.43 % is achieved. In the case of SNR $= 18\,\text{dB}$, a considerable better performance is attained. For a signal bandwidth $\text{BW}_{\text{RF}} = 20\,\text{MHz}$, the averaged EVM_{rms} value lies below 8 %, and for the $\text{BW}_{\text{RF}} = 40\,\text{MHz}$ case, the $\overline{\text{EVM}_{\text{rms}}}$ value lies below the required standard of 11 %.

In the case of the QPSK modulation scheme, while results for the signal bandwidth $\text{BW}_{\text{RF}} = 20\,\text{MHz}$ achieve the minimum requirement of $\text{EVM}_{\text{rms}} = 18.5\,\%$, i.e. a value of $\overline{\text{EVM}_{\text{rms}}} = 16.95\,\%$, results for a signal bandwidth $\text{BW}_{\text{RF}} = 40\,\text{MHz}$ exhibit a behavior of $\overline{\text{EVM}_{\text{rms}}} = 18.63\,\%$.

Finally, in the case of the 64-QAM modulation scheme an $\text{EVM}_{\text{rms}} = 9\,\%$ is required. For the $\text{BW}_{\text{RF}} = 20\,\text{MHz}$ case, an $\overline{\text{EVM}_{\text{rms}}}$ value below 6 % is obtained. And in the case of the $\text{BW}_{\text{RF}} = 40\,\text{MHz}$, an $\overline{\text{EVM}_{\text{rms}}}$ value around 9 % is reached.

In Figs. 4.21 and 4.22 an overview of all different tuning states, from $C_1 : 0\,\%$, $C_2 : 0\,\%$ to $C_1 : 100\,\%$, $C_2 : 100\,\%$, per modulation scheme at a defined SNR with $\text{BW}_{\text{RF}} = 20\,\text{MHz}$ and $\text{BW}_{\text{RF}} = 40\,\text{MHz}$ respectively, is shown. A different level of the SNR for each modulation scheme is selected. Thus, an acceptable performance in terms of BER and EVM is ensured.

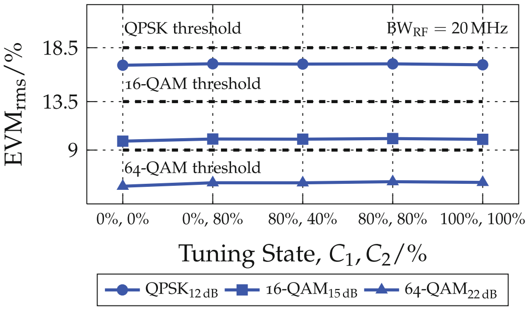

Fig. 4.21 EVM of each tuning state with a defined modulation scheme, SNR level and $\text{BW}_{\text{RF}} = 20\,\text{MHz}$ for $\overline{\text{EVM}_{\text{rms}}}$ comparison

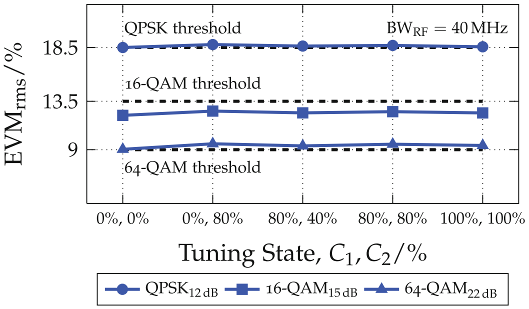

Fig. 4.22 EVM of each tuning state with a defined modulation scheme, SNR level and $\text{BW}_{\text{RF}} = 40\,\text{MHz}$ for $\overline{\text{EVM}_{\text{rms}}}$ comparison

4.2.5 Relation Between Bit Error Rate and Error Vector Magnitude

In Table 4.6 the averaged Error Vector Magnitude $\overline{\mathrm{EVM}_{\mathrm{rms}}}$ comparison, taking into account values of different specifications, per modulation scheme and signal bandwidth $\mathrm{BW}_{\mathrm{RF}}$ is summarized. The values can be compared to the BER performance shown in Fig. 4.16 for each digital modulation scheme and signal bandwidth. The averaged $\mathrm{EVM}_{\mathrm{rms}}$ value exhibited by $\mathrm{BW}_{\mathrm{RF}} = 20\,\mathrm{MHz}$ clearly satisfies the required value set by the technical specification in all modulation schemes with BERs below 1×10^{-4}. In the case of the evaluation for $\mathrm{BW}_{\mathrm{RF}} = 40\,\mathrm{MHz}$, however, the averaged $\mathrm{EVM}_{\mathrm{rms}}$ value is around the required specification in the case of the three digital modulation schemes: 16-QAM, QPSK and 64-QAM.

Considering the error probability, 16-QAM and QPSK schemes present a maximum SNR of 1 dB difference between all tuning states in the TMN maintaining a BER in the order of 1×10^{-6} for both signal bandwidths $\mathrm{BW}_{\mathrm{RF}}$. The 64-QAM scheme exhibits, however, a difference of 2.3 dB in the SNR between all tuning states holding a BER value of 1×10^{-6} for $\mathrm{BW}_{\mathrm{RF}} = 20\,\mathrm{MHz}$. Since an increase of the signal bandwidth $\mathrm{BW}_{\mathrm{RF}}$ to hold BERs in the order of 1×10^{-6} would result in a much higher SNR compared to QPSK and 16-QAM, for $\mathrm{BW}_{\mathrm{RF}} = 40\,\mathrm{MHz}$, a performance lower than $\mathrm{SNR} = 30\,\mathrm{dB}$ is considered. Hence, resulting in a difference of 6 dB in the SNR maintaining a BER of 1×10^{-2} when all tuning states of the TMN are considered.

In conclusion, Fig. 4.23 shows a comparison of the $\mathrm{EVM}_{\mathrm{rms}}$ considering BERs from different digital modulation schemes. Signal bandwidths $\mathrm{BW}_{\mathrm{RF}}$ of 20 MHz and 40 MHz together with the maximum and minimum voltage tuning states of the varactors in the TMN, i.e. 0 %, 0 % and 100 %, 100 %, are also considered.

The relation between the EVM and BER confirms that the modulation scheme with the lowest order, i.e. QPSK, is less susceptible to the influence of group delay variations considering different signal bandwidths $\mathrm{BW}_{\mathrm{RF}}$ and the tunability of the varactors in the matching network. BER and EVM values exhibit a greater difference when modulation schemes with a higher order are evaluated, i.e. 16-QAM and 64-QAM. Fundamentally, it can be observed that for a lower EVM a higher BER is present, hence, confirming an influence due to dispersion in the tunability of the matching network. These results, however, show that the performance of the matching

Table 4.6 Comparison of QPSK, 16-QAM and 64-QAM modulation schemes in terms of SNR and averaged Error Vector Magnitude $\overline{\mathrm{EVM}_{\mathrm{rms}}}$ with different signal bandwidths $\mathrm{BW}_{\mathrm{RF}}$

Scheme	SNR/dB	Std[a] $\mathrm{EVM}_{\mathrm{rms}}$/%	$\overline{\mathrm{EVM}_{\mathrm{rms}}}$/% per $\mathrm{BW}_{\mathrm{RF}}$	
			20 MHz	40 MHz
QPSK	12	18.5	16.95	18.634
16-QAM	15	13.5	9.98	12.43
64-QAM	22	9	5.92	9.36

[a] Standard taken from 3GPP technical specification [37]

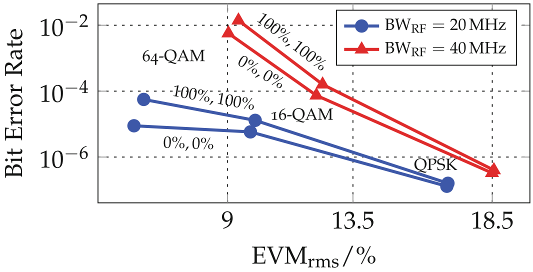

Fig. 4.23 Comparison of $\mathrm{EVM_{rms}}$ in terms of the BER considering different: (i) digital modulation schemes: QPSK, 16-QAM and 64-QAM, (ii) voltage tuning states of the varactors in the TMN: 0 %, 0 % and 100 %, 100 %, and (iii) signal bandwidths $\mathrm{BW_{RF}}$ of 20 MHz and 40 MHz

network fulfills requirements set by standards considering $\mathrm{EVM_{rms}}$ values of 9, 13.5, and 18.5 % for QPSK, 16-QAM, and 64-QAM, correspondingly.

Summarizing the complete analysis, it has been shown that to predict the behavior, and/or to provide the highest performance of a component in a communication system an efficient tuning of the varactors has to be taken into account. This tuning, therefore has to consider, apart from the typical RF characterization, the quality of a signal by means of BER and EVM when an adaptively matching is performed.

Consequently, to enhance the performance of an adaptive matching by means of agile components within the hardware of a reconfigurable frontend, the complete system can be reconfigured in terms of analog and digital measures. That is, ideally, an error free reception of data with the lowest EVM possible value to maximize the available SNR.

In the case of the investigations presented in this work, to improve the total efficiency or to recognize the best performance of a tunable matching network, e.g. at the input port of the antenna according to a defined scenario, different criteria have been considered:

- S-parameters of RF components at a defined carrier frequency f_c,
- phase linearity of the RF components,
- group delay across overall signal bandwidth,
- RF signal bandwidth,
- SNR level,
- BER level,
- EVM level,
- and defined digital modulation scheme.

Thus, by providing an agile and accurate selection of the varactor values, e.g. in the tunable impedance matching network, the most suitable system performance for a given scenario under real conditions is attained.

References

1. H.W. Bode, *Network Analysis and Feedback Amplifier Design* (D. Van Nostrand Company, New York, 1945)
2. R.M. Fano, Theoretical limitations on the broadband matching of arbitrary impedances. Technical report, Massachusetts Institute of Technology, Research Laboratory of Electronics (1948)
3. M. Pelosi, O. Franek, M. Knudsen, G. Pedersen, J. Andersen, Antenna proximity effects for talk and data modes in mobile phones. IEEE Antennas Propag. Mag. **52**, 15–27 (2010)
4. W. Yu, S. Yang, C.-L. Tang, D. Tu, Accurate simulation of the radiation performance of a mobile slide phone in a hand-head position. IEEE Antennas Propag. Mag. **52**, 168–177 (2010)
5. A. Azizzadeh, L. Mohammadi, Degradation of ber by group delay in digital phase modulation, in *Proceedings of Advanced International Conference on Telecommunications, Washington* (2008), pp. 350–354
6. P. Scragg, Digital microwave radio signatures for 16qam modem testing, in *Proceedings of South African Conference on Communications and Signal Processing* (1989), pp. 49–51
7. D. Scherer, Measurement tools for digital video transmission. IEEE Trans. Broadcast. **39**, 350–363 (1993)
8. P. Martel, G. Lossois, C. Danchesi, D. Brunei, L. Noel, Experimental investigations on ber degradations due to analogue channel filtering in zero-if receivers for fdd wcdma. Electron. Lett. **44**, 138–139 (2008)
9. A. Georgiadis, Gain, phase imbalance, and phase noise effects on error vector magnitude. IEEE Trans. Veh. Technol. **53**, 443–449 (2004)
10. T. Jensen, T. Larsen, Robust computation of error vector magnitude for wireless standards. IEEE Trans. Commun. **61**, 648–657 (2013)
11. J.D. Jackson, *Classical Electrodynamics* (Wiley, Hoboken, 1999)
12. T.S. Rappaport, *Wireless Communications Principles and Practice* (Prentice Hall PTR, New Jersey, 2002)
13. J.G. Proakis, *Digital Communications* (McGraw-Hill, Boston, 2001)
14. N. Lay, M. Dillon, E. Satorius, J. Mulligan, A communications system testbed, in *1996 Conference Record of the Thirtieth Asilomar Conference on Signals, Systems and Computers*, vol. 1 (1996), pp. 663–667
15. B. Shishkin, D. Pfeil, D. Nguyen, K. Wanuga, J. Chacko, J. Johnson, N. Kandasamy, T. Kurzweg, K. Dandekar, *SDC Testbed: Software Defined Communications Testbed for Wireless Radio and Optical Networking* (2011), pp. 300–306
16. D. Adasiak, M. Grela, D. Rosolowski, Flexible offline testbed for verification of new rf techniques and concepts, in *Proceedings of 17th International Conference on Microwaves, Radar and Wireless Communications* (2008), pp. 1–4
17. R. Morawski, T. Le-Ngoc, O. Naeem, Wireless and Wireline Mimo Testbed (2003)
18. R. Rao, W. Zhu, S. Lang, C. Oberli, D. Browne, J. Bhatia, J.-F. Frigon, J. Wang, P. Gupta, H. Lee, D. Liu, S. Wong, M. Fitz, B. Daneshrad, O. Takeshita, Multi-antenna testbeds for research and education in wireless communications. IEEE Commun. Ma **42**, 72–81 (2004)
19. R. Freeman, *Radio System Design for Telecommunication* (Wiley, New Jersey, 2007)
20. Y. Zheng, H. Maune, A. Giere, M. Sazegar, R. Jakoby, Constraints on efficient control of tunable impedance matching network based on barium-strontium-titanate thick-film varactors, in *38th European Microwave Conference, EuMC* (2008)
21. H. Maune, S.M.Y. Zheng, X. Zhou, A. Giere, P. Scheele, F. Paul, J. Binder, R. Jakoby, Nonlinear ceramics for tunable microwave devices part ii: Rf-characterization and component desig. Microsyst. Technol. **17**(2), 213–224 (2011)
22. Y. Zheng, *Tunable Multiband Ferroelectric Devices for Reconfigurable RF-Frontends* (Springer, New York, 2013)
23. P. Scheele, A. Giere, Y. Zheng, F. Goelden, R. Jakoby, Modeling and applications of ferroelectric-thick film devices with resistive electrodes for linearity improvement and tuning-voltage reduction. IEEE Trans. Microw. Theory Tech. **55**, 383–390 (2007)

24. Matching circuit optimization for antenna application. Technical report, CST AG (2012)
25. Bluetooth antenna design. Technical report, Texas Instruments (2013)
26. P. Mathiopoulos, H. Ohnishi, K. Feher, Study of 1024-qam system performance in the presence of filtering imperfections. IEE Proc. I Commun. Speech Vis. **136**, 175–179 (1989)
27. E.D. Sunde, Pulse transmission by am, fm, and pm in the presence of phase distortion. Bell Syst. Tech. J. **40**, 353–422 (1961)
28. H. Bogucka, K. Wesolowski, Frequency-domain echo cancellation in digital multicarrier modulation systems. IEEE Trans. Commun. **48**, 333–342 (2000)
29. S. Sesia, M. Baker, I. Toufik, *LTE–The UMTS Long Term Evolution: From Theory to Practice*, 2nd edn. (Wiley, Chichester, 2011)
30. H. Holma, A. Toskala, *WCDMA for UMTS: Radio Access for Third Generation Mobile Communications* (Wiley, New York, 2002)
31. J. Heiskala, J. Terry, *OFDM Wireless LANs: A Theoretical and Practical Guide* (SAMS, Indianapolis, 2001)
32. H. Arslan, H. Mahmoud, Error vector magnitude to snr conversion for nondata-aided receivers. IEEE Trans. Wirel. Commun. **8**, 2694–2704 (2009)
33. H. Yap, *Designing To Digital Wireless Specifications Using Circuit Envelope Simulation*, vol.1 (1997), pp. 173–176
34. R. Hassun, M. Flaherty, R. Matreci, M. Taylor, *Effective Evaluation of Link Quality Using Error Vector Magnitude Techniques* (1997), pp. 89–94
35. 3GPP ts 25.141.v5.15.0 technical specification group radio access network; base station (BS) conformance testing (FDD) (2009)
36. 3GPP ts 36.101.v8.8.0 technical specification group radio access network evolved universal terrestrial radio access; evolved universal terrestrial radio access (E-UTRA); user equipment (UE) radio transmission and reception (2009)
37. 3GPP ts 36.141.v10.1.0 lte; evolved universal terrestrial radio access (E-UTRA); base station (BS) conformance testing (3gpp ts 36.141 version 10.1.0 release 10) (2011)
38. 3GPP TR 25.814 v7.1.0 technical specification group radio access network; physical layer aspects for evolved universal terrestrial radio access (UTRA) (2006)

Chapter 5
System Integration and Control of Tunable Components

Considering the exponential growth of technology related to the realization of circuits [1], a new kind of architectures including reconfigurable components can be implemented in portable devices. Apart from the microwave characterization and the exhibited performance at a system level of a tunable component, a design that eases its system integration into any communication device is also required [2]. Due to physical and electrical limitations, such as size restrictions and available power supply, it is a sensitive task to obtain a precise control of a tunable component when the goal is the integration into a handheld device.

In this chapter, a solution targeting reconfigurable architecturesc considering a high-voltage control of a tunable matching network for system integration into portable devices is proposed. For example, such a reconfigurable architecture is the transceiver shown in Fig. 1.1 (Chap. 1).

In the first sections of this chapter, the components that confirm the proof of concept are introduced and briefly discussed, e.g. considering the operation frequency and the required tuning voltage for control. These requirements are established by the properties of the tunable matching network. Here, the matching network based on ferroelectric varactors presented in Chap. 4 is considered for further investigations. In the second part, a method to enable an adaptive control of the tunable matching device by means of a coupler detector module is proposed. Finally, after integrating an architecture in form of a demonstrator, diverse measurements confirmed the principle of functionality.

5.1 Dualband Antenna Module with Tunable Matching Network

Integration of tunable components is necessary to enable reconfigurable architectures for portable devices like PDAs, laptops, mobile phones and tablets. Nevertheless, this represents a challenging task when specifications such as compactness and minimal

E. Gonzalez Rodriguez, *Reconfigurable Transceiver Architecture for Multiband RF-Frontends*, Smart Sensors, Measurement and Instrumentation 17,
DOI 10.1007/978-3-319-24581-2_5

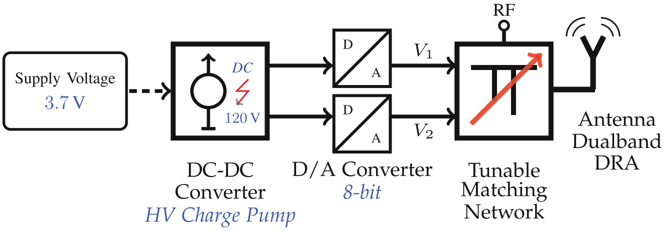

Fig. 5.1 Proof of concept of a reconfigurable antenna module with different kind of technologies, i.e. DRA with tunable matching network based on ferroelectric varactors enabled by CMOS high-voltage technology handling up to 120 V [3, 4]

energy consumption have to be also fulfilled, while the required spectrum remains covered. By focusing on the system integration of a reconfigurable antenna architecture based on different components and technologies, the following reconfigurable antenna proof of concept is proposed and implemented.

In the block diagram of Fig. 5.1, core functionality of the reconfigurable antenna module is shown. By means of this concept, the use of functional materials that require a high-voltage, e.g. ferroelectric, liquid crystal, and MEMS, are enabled in such a way that the antenna of the RF-Frontend can be reconfigured to ensure proper functionality under different environments.

To realize a proof of concept that demonstrates an accurate tuning of a TMN module, CMOS technology was used to generate the required high-voltage (HV). This includes a high-voltage charge pump providing at least 90 V from a typical 3.7 V battery as used in current mobile phones, with two digital analog (D/A) converters, each one to tune one ferroelectric varactor of the matching network [3, 4]. In the following sections the components of the reconfigurable architecture are introduced, as well as the principle of operation using a dualband dielectric resonator antenna (DRA).

5.1.1 Dualband Dielectric Resonator Antenna

An attractive employment of tunable multiband antennas, e.g. in mobile devices, feature the independent band tuning capability considering a single operation frequency while the restricted volume of the device is efficiently utilized [5, 6]. In contrast to the UWB antenna of the demonstrator shown in Chap. 3, in this chapter a smaller antenna is used with narrowband characteristic. This antenna exemplary demonstrates the influence of the environment over operation at a designed center frequency, and how the detuning of the antenna is corrected by performing an adaptive matching. However, the developed approach to be presented can be also applied to UWB antennas.

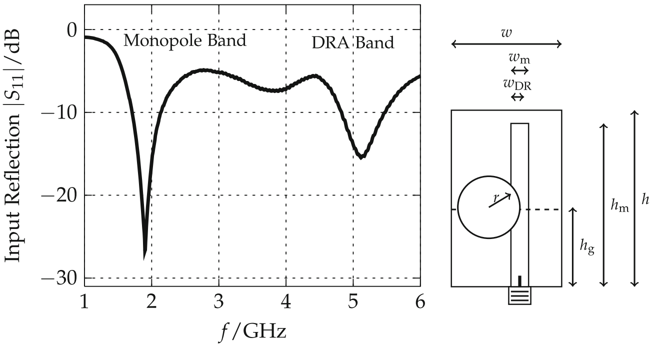

h	50 mm
h_m	48 mm
h_g	17.5 mm
w	24 mm
w_m	1.8 mm
w_{DR}	0.6 mm

Fig. 5.2 Hybrid dielectric dualband resonator antenna [7, 8]. Input reflection $|S_{11}|$ with operation bands at $f_{c1} = 1.9$ GHz and $f_{c2} = 5.1$ GHz

The input reflection $|S_{11}|$ of the low-profile antenna and its dimensions are shown in Fig. 5.2 [7, 8]. The antenna consists of a printed monopole, covering a lower frequency band at 1.9 GHz band with an input matching better than −25 dB. The added dielectric resonator, placed over the monopole which acts as a feed, covers an upper frequency band at 5.1 GHz with an input matching of −15 dB. The DRA is fabricated from glass-ceramic material with a relative permittivity $\varepsilon_r = 22$ and loss tangent $\tan\delta = 0.005$. The monopole is printed on a Rogers 4003C substrate with $\varepsilon_r = 3.66$ and height of 0.81 mm.

The DRA is constructed from a glass-ceramic material. This material provides diverse advantages over ordinary ceramic materials [7]. Among the most important characteristics is that highly accurate geometries can be achieved. During ceramization, the shrinkage of the glass ceramic ($<$1 %) is much smaller than the sintering of a conventional ceramic ($>$10 %). Furthermore, due to a well refined glassy phase, pore free materials can be obtained [8]. This material is consequently considered as an attractive option for communication technologies where multiband frequency operation and/or multiservice antennas at the user equipment are required [9]. Therefore, the increase of hardware in the user equipment can be avoided, e.g. by using a minimum number of antennas.

For evaluation of the reconfigurable module a dielectric resonator antenna was employed. An important advantage of using a dielectric resonator is that a multiband characteristic can be easily enabled for a simple monopole antenna. Furthermore, the placement of the dielectric resonator has minimal effects on the resonance of the monopole itself resulting in an almost negligible influence in terms of the radiation efficiency and the frequency of operation [10].

5.1.2 Adaptive Control Methodology of Tunable Matching Network

The overall operation of the reconfigurable antenna architecture envisions to follow a methodology so that the tunable matching network together with the adaptive control can be enabled in the most efficient way.

A solution is proposed based on requirements to be fulfilled by the components in the architecture. Thus, apart from the reviewed BER and EVM, the frequency of operation as well as the input reflection $|S_{11}|$ are to be considered. Furthermore to achieve this requirement, the tunability response has to be taken into account. Because the tunable matching network presented in Chap. 4 includes two varactors, each one from 0 to 90 V, an abstract geometric representation of the form 2^n can be introduced. In this approach, as shown in Fig. 5.3, n represents the amount of varactors that controls the matching network. Thus, the amount of vertices in the polygons represent the combination between the minimum and maximum tuning state of each varactor. The methodology starts on an arbitrary point in the polygon. The arbitrary point represents a determined tuning state of both varactors in an unmatched case. Then, the final tuning state that satisfies a matching criteria is found after a number of iterations.

Depending on the application and focusing on the behavior of the input reflection $|S_{11}|$ that depends on the tuning voltage, different solutions can be applied to achieve efficiently a certain matching condition. For example, (i) if the goal is to carry out a spectrum sensing, *tuning over a determined frequency range* can be applied. That is, alternating constantly the biasing voltage of one varactor and then the other varactor. In this case the approach is called spiral seeking. (ii) If the goal, is to have a *fine matching tuning at a single frequency of operation*, one varactor can be tuned up to a certain point, until the required matching is achieved. If the condition is not achieved,

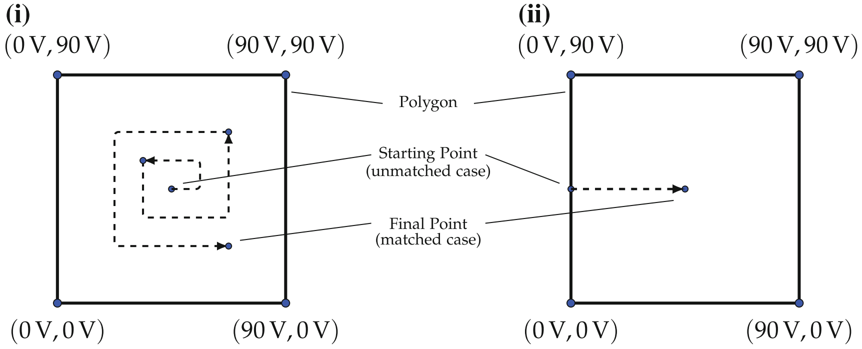

Fig. 5.3 Polygon of the form 2^n based on the bias voltages to control the behavior of a tunable matching network with two varactors. Two solutions can be implemented taking into account the geometric principle: (i) spiral seeking approach oriented for spectrum sensing, and (ii) edge to center approach for fine matching tuning at a defined frequency of operation

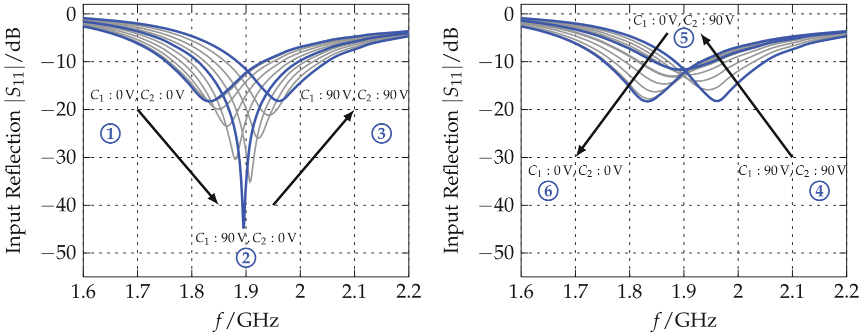

Fig. 5.4 Response of tunable matching network based on ferroelectric varactors employing a spiral seeking approach. Considering the boundary values 0 and 90 V, the gradual voltage tuning of the varactors is used as the base to perform an adaptive and accurate control of the reconfigurable antenna module along the frequency axis

the second varactor is again tuned, and again the first varactor repeats the refining process. In this case the approach is called edge to center.

This principle can also be represented in the Smith Chart by mapping the matched impedances according to its corresponding tuning state. However, for practical cases the shape of the polygon vanishes, and thus, makes unclear its graphical representation for this explanation purposes.

In Fig. 5.4, a representation of the input reflection of the matching network considering the varactor tuning voltage from 0 to 90 V measured in a 50 Ω environment is shown. In the case of this matching network it can be seen that the two ferroelectric varactors, C_1 and C_2, yield four boundary tuning states depending on the biasing voltage: (0 V, 0 V), (90 V, 0 V), (0 V, 90 V), and (90 V, 90 V). Furthermore, based on the described geometric principle, in this example, a spiral seeking approach is graphically described by tuning the varactors in the form (0 V, 0 V) → (90 V, 0 V) → (90 V, 90 V) → (0 V, 90 V) → (0 V, 0 V), resulting, in a scanning of matched bands from around 1.8 to 2.0 GHz holding an input reflection of at least −11.5 dB.

5.1.3 High-Voltage Generation for Tunable Components

Investigations on the performance of a tunable matching network based on ferroelectric varactors for different mobile standards considering microwave characterization, e.g. scattering parameters, and a digital system analysis, e.g. BER and EVM, have been demonstrated in Chap. 4. It has been shown that each voltage tuning state of the varactors in the matching network yield a different performance to improve the signal quality. Fundamentally, this high-voltage is of utmost importance to precisely control the tuning of the varactors in the matching network. Consequently, to carry

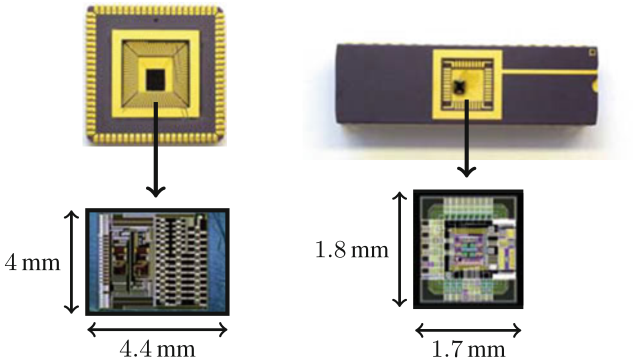

Fig. 5.5 *Top* Mounted ASICs on top of chip sockets for evaluation. *Bottom* Layout of HV charge pump [3] (*left*) and D/A converter [4] (*right*)

out this implementation, a solution to enable the required high-voltage tuning into handheld devices has been faced.

In cooperation with the Integrierte Elektronische Systeme (IES) group at Technische Universiät Darmstadt, TICMO Graduiertenkolleg,[1] and within the framework of the research priority program LOEWE Cocoon,[2] to overcome the integration constraint of high-voltage generation into a portable device, two different kinds of integrated circuits were developed. These ICs can essentially provide the biasing voltage to control tunable components, in this case of the TMN module. The first one is a high-voltage charge pump [3] responsible to generate the required biasing of at least 90 V for the matching network. And the second one is a digital analog converter [4] which sets the amount of voltage to tune the varactor. Therefore, two D/A converters are required. Since the D/A converter includes 8-bit for control, the integrated circuit can provide steps of 0.35 V considering this matching network. This value provides high flexibility when a fine tuning is required considering that the matching network module can be tuned from 0 to 90 V within a frequency range of 200 MHz.

In Fig. 5.5 mounted ASICs (Application-specific integrated circuit) on chip sockets (top) and layout of the ICs (bottom) are shown. The footprint size of the HV charge pump with on-chip clock generators (left) and D/A converter (right) is 17.6 mm^2 and 3.1 mm^2, respectively.

Both ICs were fabricated in AMS H35 CMOS technology (0.35 µm) from Austriamicrosystems which enables operation voltages up to 120 V. Since both ICs use the same technology for fabrication, a further integration in a single chip can be realized. The ASICs are mounted on empty chip sockets for single performance measurement, as well as for measurement purpose of the demonstrator.

---

[1] Tunable Integrated Components in Microwave Technology and Optics, GRK1037.

[2] Landes-Offensive zur Entwicklung Wissenschaftlich-ökonomischer Exzellenz, Cooperative Sensor Communication.

The high DC voltage up to 120 V presented in [3] is generated from a 3.7 V nominal DC supply with a maximal load current $I_{\mathrm{L}} = 100\,\mu\mathrm{A}$ based on a modified Pelliconi charge pump structure. This modified design adopts a dynamic bulk-biasing technique [11] to improve the output voltage saturation that a conventional Pelliconi charge pump presents [12]. With respect to the D/A converters, the current consumption of the ICs is 60 μA when they operate at a voltage of 120 V. Hence, this high voltage can still allow proper operation of the charge pump output voltage. Furthermore, the rising time to tune the voltage from 0 to 90 V is confined as

$$\Delta t_{\mathrm{max}} = \frac{V_{\mathrm{max}} \cdot C(V_{\mathrm{max}})}{I_{\mathrm{D/A}}}, \tag{5.1}$$

where $I_{\mathrm{D/A}}$ is the current provided by the D/A converter, V_{max} is the maximum applied tuning voltage by the charge pump to the TMN module, and $C(V_{\mathrm{max}})$ is the corresponding capacitance of the varactor at the maximum voltage tuning state. BST layers allow switching times in the order of nanoseconds [13]. Hence, the limiting factor for the switching time is determined by the DACs resulting in $\Delta t_{\mathrm{max}} = 0.44\,\mu\mathrm{s}$ when the maximum tuning voltage of 90 V with a capacitance of 0.31 pF is considered.

Since TMNs require a precise voltage to provide the desired matching, D/A converters play a crucial role during the selection of the correct varactor tuning once a mismatch of the antenna input impedance occurs. Therefore, two static characteristics can evaluate the accuracy of D/A converters: the differential nonlinearity (DNL) and the integral nonlinearity (INL). These characteristics are correspondingly, the deviation from the ideal step and the accumulated error to express the total deviation (Appendix A.3). In the ideal case, each analog output step size, given in terms of the input voltage, should correspond to exactly one least significant bit (LSB). Nevertheless, real D/A converters tend to differ from their ideal values, i.e. a difference of the analog increment per step compared to an exact LSB occurs. These inherent effects are caused due to fabrication processes, tolerances and mismatch variations [14].

In regard to this implementation, values of 0.17 LSB for the DNL, and of 0.48 LSB for the INL case were achieved. Since these measured values are smaller than 0.5 LSB, these D/A converters fulfill the requirement to provide an accurate driving voltage for the tunable matching network. Thus, the D/A converters can provide a voltage step of 0.35 V with an accuracy of ±0.175 V considering the maximum voltage of 90 V.

5.2 Adaptive Control Principle and Performance

Although novel tunable components have emerged in the last years, less attention has been given to their integration considering the monitoring and control into current portable devices. An important challenge to solve is therefore the signal optimization at the antenna input port, for instance, when matching networks employ components such as varactors requiring voltages in the order of 100 V.

Two different scenarios can be considered when an antenna is reconfigured by employing a matching circuit; (i) either when an antenna is tuned to operate at different frequency bands to provide another service or to sense another carrier with improved spectrum conditions, or (ii) to guarantee a defined performance at a center frequency. In this implementation the latter case is considered for study due to the challenging task that the impedance matching of an antenna represents in mobile phone applications when is affected by the presence of objects located in the vicinity of the device [15–17]. Therefore, an architecture is proposed that performs (i) the control of the matching network, (ii) the generation of accurate high biasing voltage, (iii) the signal monitoring, e.g. using a detector circuit with directional coupler, and (iv) the overall communication of the components, i.e. the link between the antenna and the processing unit so that the overall system can be continuously self-reconfigured.

The complete reconfigurable antenna architecture is shown in Fig. 5.6 including the adaptive control, e.g. to satisfy the matching condition of at least $|S_{11}| \leq -10\,\text{dB}$ in the antenna at a frequency of operation. The core of the reconfigurable platform consists of a dualband antenna, and a tunable matching network based on ferroelectric varactors. The required high biasing tuning voltage is enabled by CMOS charge pump and D/A converters to generate the correct input voltage to the TMN module. Complementing the proof of concept shown in Fig. 5.1, by employing these components along with a coupler detector module and FPGA, overall system integration of the reconfigurable antenna module is demonstrated. Thus, assurance of the proper antenna performance using compact reconfigurable components evaluated under different scenarios is further shown.

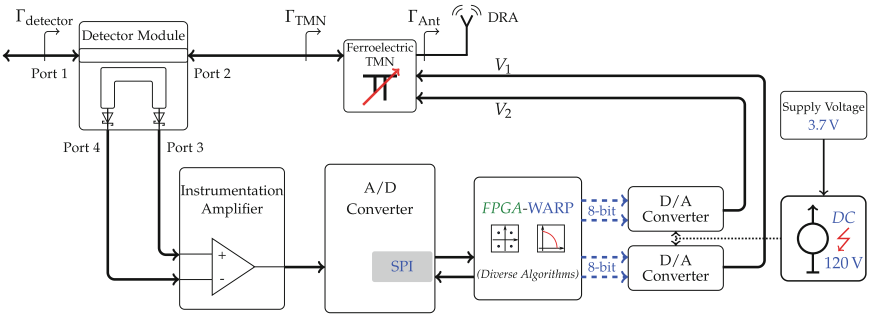

Fig. 5.6 Tunable antenna architecture. Autonomous reconfigurable platform employing components based on novel technologies, i.e. TMN based on ferroelectric varactors, dualband DRA antenna based on glass-ceramics and generation of high voltage from 3.7 V battery by means of a CMOS charge pump and D/A converter

The process begins when the signal at the input port of the antenna (Γ_{Ant}) is reflected as a result of a detuning due to the influence of the surrounding environment, such as proximity to metallic surfaces and human body, e.g. head and hand. In that way, the coupler module together with detector diodes, monitors the change in the input impedance of the antenna located now at the reference port of the matching network (Γ_{TMN}), and rectifies the sampled signal to enable its evaluation, e.g. in terms of voltage.

In detail, when the coupler module detects any variation over the antenna input impedance, this variation also appear at the reference port of the matching network (Γ_{TMN}). However, the matching network itself compensates this influence by looking out for a tuning state that satisfies a required matching condition of the antenna, e.g. $|S_{11}| \leq -10\,\mathrm{dB}$.

This variation in the input reflection $|S_{11}|$ of the antenna, now travelling in backward direction from port 2 to the reference port of the directional coupler ($\Gamma_{\mathrm{detector}}$), consequently also appears at port 4 as a portion of the reflected signal, respectively. Based on a design including detector diodes at port 3 and port 4 branches, the RF voltage is rectified. To interpret the meaning of the monitored signal, i.e. if a matching condition is achieved or a compensation is required, by means of an instrumentation amplifier and A/D converter, the rectified RF samples are differentiated. Thereafter, the resulting signal is amplified and digitalized.

Data is further processed by an FPGA where an optimization algorithm can be developed taking into account the properties of the matching network. Such is the case of the number of varactors used, covered frequency and occupied bandwidth. Although the implementation of algorithms represent an enormous field of study, the tunability behavior has to be clearly understood to realize an effective matching. Thereafter, wide alternatives of solutions can be applied, e.g. steepest decent, gradient, among others [18, 19]. Therefore, focus on the consequences and limitations of the varactor tuning is given throughout this work rather than addressing the development of an algorithm.

In the presented implementation, the condition to obtain the minimum reflection coefficient Γ_{Ant} corresponds to the maximum difference exhibited by the scattering parameters at the frequency of interest in the output ports 3 and 4 of the directional coupler. In other words, considering the RF voltage detector diodes, the best possible matching condition is conducted by the greatest voltage difference between ports 3 and 4 of the detector module. In this case a 50 Ω reference impedance is considered, e.g. as used in mobile phone applications.

Finally, after determining which voltage combination is necessary to improve the signal, e.g. by means of an algorithm executed from the FPGA, the D/A converters, fed by the HV charge pump, set the new voltages for the matching network. In this manner, this iterative process is realized to ensure the best possible matching condition at a defined frequency. This process is naturally limited by the frequency range of operation of the TMN module and the detector module itself.

5.2.1 Detector Module

The goal of this circuit is to monitor the reflection coefficient of the antenna to perform a proper selection of the varactor voltages in the tunable matching network. Considering the printed monopole of the presented dualband antenna, a compensation of the impedance mismatch in the lower band at 1.9 GHz can be achieved when the input reflection $|S_{11}|$ degrades due to the influence of the surrounding environment.

In the past, different methods for power measurement have been studied besides the RF properties and characterization of single components [20]. Nevertheless, less attention has been drawn to the implementation of this kind of circuits targeting the control of tunable components. Furthermore, apart from the control, two different scenarios should be compared according to the required matching: maximum output power and minimum reflection matching. Considering the maximum output power, this can be achieved by fulfilling the conjugate complex criteria $\underline{Z}_{\mathrm{S}} = \underline{Z}_{\mathrm{L}}^{*}$. In the second case, the minimal reflection matching condition can be met when $\underline{Z}_{\mathrm{S}} = \underline{Z}_{\mathrm{L}}$, i.e. when both, real and imaginary parts are equal [21]. Both criteria only agree when both impedances are equal and purely real, i.e. $Z_{\mathrm{S}} = Z_{\mathrm{L}}$.

For this implementation a minimal reflection matching is considered to optimize the input reflection $|S_{11}|$, however, the same detector module can be used between the TMN module and the antenna to maximize the power transferred from the power amplifier to the antenna [22, 23]. Therefore, an approach to enable monitoring functionality is proposed taking into account the limitations in terms of the component tuning frequency, reflection matching and voltage requirements.

The detector module essentially includes a directional coupler and two RF voltage detector diodes to rectify and compare a sample of the monitored signal. The output voltage to decide if reflections are present at the input port of the antenna, and therefore at the matching network, should be compensated by the TMN module itself.

The operation principle of the directional coupler can be described based on the complex scattering parameters matrix of a reciprocal four-port network of a directional coupler (Appendix A.2). To realize the directional coupler shown in Fig. 5.7, two line sections with port terminations are to be considered for this implementation. Thus, four RF ports are defined to analyze the prototype; in the main line with input port 1 and output port 2, and in the coupled line with input port 3 and output port 4 [24].

Considering previous port configuration, scattering parameters can be described as follows: input reflection and isolation parameters, S_{11} and S_{41} respectively, approach its best value towards a minimum zero. Forward transmission S_{21} parameter reaches its best value towards a maximum of a unity. And the coupling coefficient κ, which in this case is defined by a threshold of 20 dB, is described by the S_{31} parameter, i.e. a sampled signal with 1 % of the total signal energy is taken into the coupled line.

Two modules in planar microstrip technology matched for different center frequencies were fabricated on a Rogers 5880 substrate with $\varepsilon_r = 2.2$, loss tangent $\tan\delta = 0.0001$ and 1.576 mm thickness. This substrate compared to the FR_4, e.g.

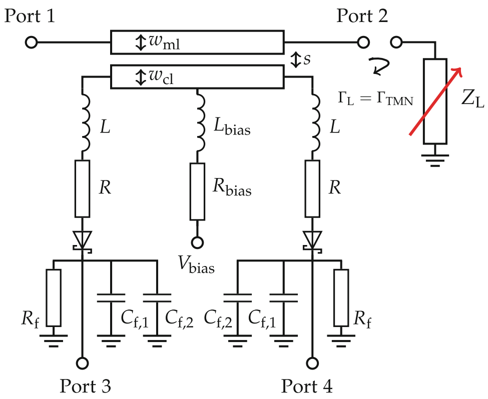

Module	1	2
f_{c}/GHz	1.4...1.6	1.7...2.0
$Z_{0,\text{ coupled line}}/\Omega$	50	126
κ/dB	20	20
w_{ml}/mm	4.88	4.88
w_{cl}/mm	4.88	0.78
s/mm	0.6	1.5
L/nH	13	22
R/Ω	92	310
$C_{\mathrm{f,1}}$/pF	4.3	4.3
$C_{\mathrm{f,2}}$/nF	33	33
$R_{\mathrm{f}}/\mathrm{k}\Omega$	1	1
L_{bias}/nH	47	30
R_{bias}/Ω	200	200

Fig. 5.7 Specifications of detector modules based on −20 dB directional couplers with RF detector Schottky diodes for monitoring of voltage variations across the load

used for the gain amplifier in the transceiver shown in Chap. 3, yields a wider width of the 50 Ω line offering a more robust solution for fabrication. Specially when the width of the coupled line in the directional coupler is decreased to obtain a higher impedance resulting in higher voltages. HSMS-2850 zero bias Schottky detector diodes from Avago Technologies [25] were used for rectification with RC low pass filter at the outputs of ports 3 and 4 for noise suppression and smoothness of the signal.

Regarding the architecture diagram of Fig. 5.6, a detailed view of the directional coupler with detector diode is shown in Fig. 5.7. The main parameters for the design of the −20 dB directional couplers with diode detectors for rectification of the signal are shown in the table included in Fig. 5.7. To evaluate the variation of the input reflection at port 1 of the main line considering different reflection coefficient values Γ_{L} at port 2, the voltage difference $\Delta V_{\mathrm{P}_3-\mathrm{P}_4}$ between port 3 and port 4 of the detector module is measured. External biasing for detector diodes is introduced in the center part of the coupled line to increase the detection performance when the RF detectors operate with higher current–voltage characteristic.

A directional coupler owns an inherent wideband characteristic. However, when the detector circuit is included to rectify the RF signal the overall detector module becomes narrowband. Fundamentally, since the diodes in the detector circuit require to be matched at the impedance characteristic of the coupled line, a reactive matching of the form $R + jX$ is realized based on an inductance in series with a resistor. As a result, this matching is essentially narrowband. Nevertheless, at the expense of sacrificing dynamic range of the detected voltage, a broadband matching can be achieved [26, 27]. In that way, whereas the inductance matches the reactive part of the diode, the resistive part, which simultaneously also adjusts the dynamic range of the detector circuit, can easily be matched.

In Fig. 5.8 the fabricated prototypes for evaluation are shown. The first prototype, detector module 1, is fully 50 Ω matched for operation at 1.5 GHz, i.e. both, the main

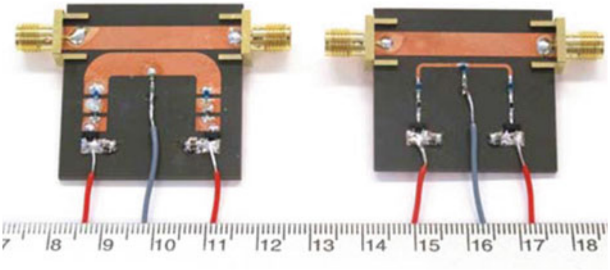

Fig. 5.8 Fabricated prototypes of detector modules 1 and 2. Voltage detector modules for operation frequencies at 1.5 GHz (*left*) and 1.9 GHz (*right*) in microstrip technology with HSMS-2850 zero bias Schottky detector diodes

line and coupled line with the same width. The second prototype, detector module 2, designed for operation at 1.9 GHz is also 50 Ω matched along the main line. However, the coupled line has an impedance of 126 Ω resulting in higher detected voltages at ports 3 and 4 of the detector module.

To summarize the fabrication of the voltage detector module, first, the directional coupler was designed to achieve specifications, such as a coupling coefficient κ and frequency range of operation. Thereafter, the detector circuit was included in the simulations. And since addition of this circuit influences the response of the previous design, the directional coupler is now optimized to achieve the required specifications with the detector circuit. These specifications consider the influence of inductances, Schottky diodes and resistors in the coupled line branches.

5.2.2 Linear Impedance Evaluation for Voltage Detection

According to Fig. 5.9, real impedance values taken from SMD resistors were used to cover the complete range of Z_L impedances in the Smith Chart along its radius in terms of the reflection coefficient $\Gamma_\mathrm{L} = \frac{Z_\mathrm{L}-Z_\mathrm{S}}{Z_\mathrm{L}+Z_\mathrm{S}}$ with source impedance Z_S normalized to 50 Ω.

In the table of Fig. 5.9 the set of impedances Z_L in terms of the reflection coefficient Γ_L are shown. The set of normalized impedances $Z_\mathrm{L,\,norm}$ with reference impedance $Z_0 = 50\,\Omega$ in terms of the Γ_L value is equally distributed along the real axis of the Smith Chart. The purpose of this distribution is to perform a linear evaluation of the detected voltages considering different loads. Moreover, if the linear distribution would rotate around its origin $\Gamma_\mathrm{L} = 0$ axis, i.e. at $\mathrm{Z}_\mathrm{L,\,norm} = 1$, voltage evaluation with complex impedances that consider also the imaginary plane over the same linear axis would still hold the linear condition.

Γ_L	Z_L/Ω (var. ±5%)	$Z_{L,\,\text{norm}}$
-1	short	0
-0.8	5.6	0.11
-0.6	13	0.26
-0.4	22	0.44
-0.2	33	0.66
0	50	1
$+0.2$	75	1.5
$+0.4$	110	2.2
$+0.6$	200	4
$+0.8$	430	8.6
$+1$	open	∞

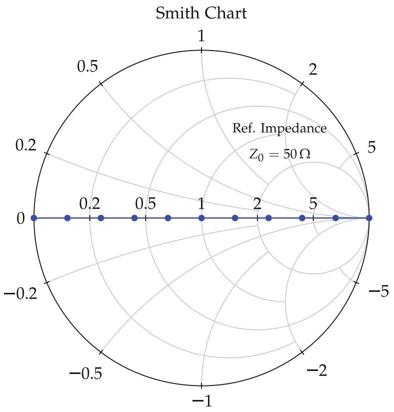

Fig. 5.9 Smith Chart with equally distributed reflection coefficient Γ_L values along the real axis, i.e. different normalized impedances $Z_{L,\,\text{norm}}$ considering a linear evaluation of the adaptive control module are taken into account

To optimize the input reflection of the signal at the antenna port, such as in Fig. 5.7, the signal is monitored by the detector module. The detector module provides two voltages for comparison at port 3 and port 4 related to the incoming signal at ports port 1 and port 2, respectively.

Both signals at ports 3 and 4 of the detector module are compared in such a way that for the highest voltage difference the matching condition approaches a reflection coefficient moving towards $\Gamma_L \rightarrow 0$, i.e. the matched case with the lowest $|S_{11}|$ value. And for the lowest voltage difference, the reflection coefficient converges on values towards $\Gamma_L \rightarrow \pm 1$, i.e. the input reflection requires optimization to reach at least the condition $|S_{11}| \leq -10\,\text{dB}$.

In ideal cases, a perfect symmetry between negative and positive values with same magnitude of the reflection coefficient Γ_L can be achieved. In cases where the RF detector operates at other frequency different from the designed, changes in the impedance characteristic of the detector diode are present. Thus, an asymmetric response arises. Furthermore, tolerances and fabrication constraints of the employed components can also contribute to this asymmetric behavior. The consequences of this asymmetry, considering the usability of the detector module are explained in detail in the following sections.

Microwave Characterization of the Detector Module

The design of a detector module considers a compromise between the matching at the input port of the main line, the effect of the coupling coefficient between the lines, and the maximum detected voltage difference at a desired operation frequency. As an example of this, measurements and simulations of the optimized directional coupler without considering the effect of the detector circuit are shown in Fig. 5.10.

The setup for evaluation employed a 4-Port network analyzer from Agilent, and for the simulations AWR Microwave Office. In the case of directional coupler 1, in spite of an initial simulate coupling coefficient parameter $\kappa = -20\,\text{dB}$, the coupling

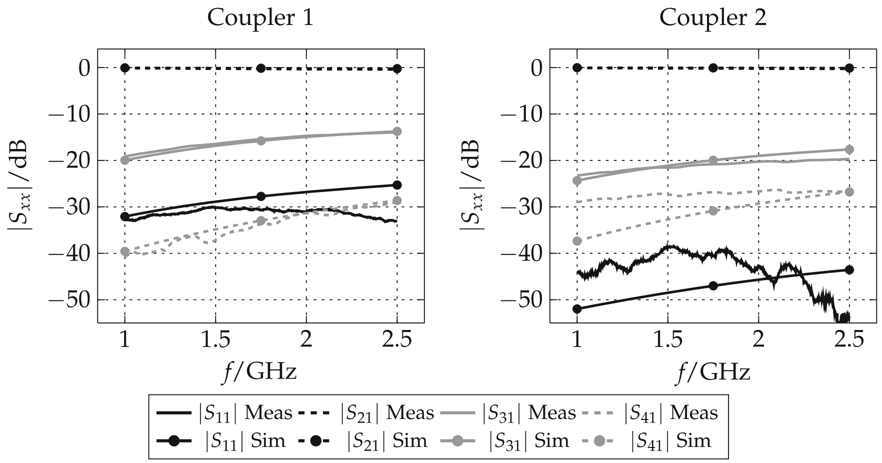

Fig. 5.10 Scattering parameters measurement and simulation of coupler 1 and 2 for $\Gamma_L = 0$. $|S_{21}|$ parameter with an insertion loss of less than −0.3 dB. $|S_{11}|$ parameter with a reflection lower than −40 dB. Difference between coupling factor $|S_{31}|$ and $|S_{41}|$ parameter of 18 dB for coupler 1 at 1.5 GHz and of 8 dB for coupler 2 at 1.9 GHz

$|S_{31}|$ is increased to a value around −17 dB. In the case of directional coupler 2, the $|S_{31}|$ remains close to −20 dB at an expense of a reduction in the $|S_{41}|$ isolation. In other words, the difference between $|S_{31}|$ and $|S_{41}|$ at a defined center frequency will determine the maximum detected voltage when $Z_{\text{Ant}} = 50\,\Omega$, i.e. $\Gamma_{\text{Ant}} = 0$. In these prototypes a difference of 18 dB for coupler 1 at 1.5 GHz, and of 8 dB for coupler 2 at 1.9 GHz, is achieved. This results in a larger detection range for coupler 1 compared to coupler 2 without considering the influence of the detector circuit.

Simulations in terms of the scattering parameters for different load impedances are performed to show operation of the detector module at defined center frequency. In Fig. 5.11, a S-parameter result of the main line ports, i.e. $|S_{11}|$ and $|S_{21}|$, and the coupled line ports, i.e. $|S_{31}|$ and $|S_{41}|$, are shown for directional coupler 1 including the rectification circuit with detector diodes.

By sweeping different reflection coefficient values at port 2 of the main line to obtain scattering parameter results, it can be clearly recognized that for $\Gamma_L = 0$, i.e. $Z_L = 50\,\Omega$, a minimum value lower than −25 dB for the input reflection $|S_{11}|$ is obtained. The forward transmission $|S_{21}|$ remains almost flat at 0 dB over the complete frequency range. And in the remaining cases when $\Gamma_L \to \pm 1$, the value of the input reflection $|S_{11}|$ increases towards zero and the value of the forward transmission $|S_{21}|$ decreases below −60 dB.

In the case of the coupled line, for the $|S_{31}|$ it can be seen that the value around the center frequency $f_c = 1.5$ GHz exhibits an almost constant behavior, and thus, referring to the coupling coefficient κ specification. In the case of the isolation $|S_{41}|$

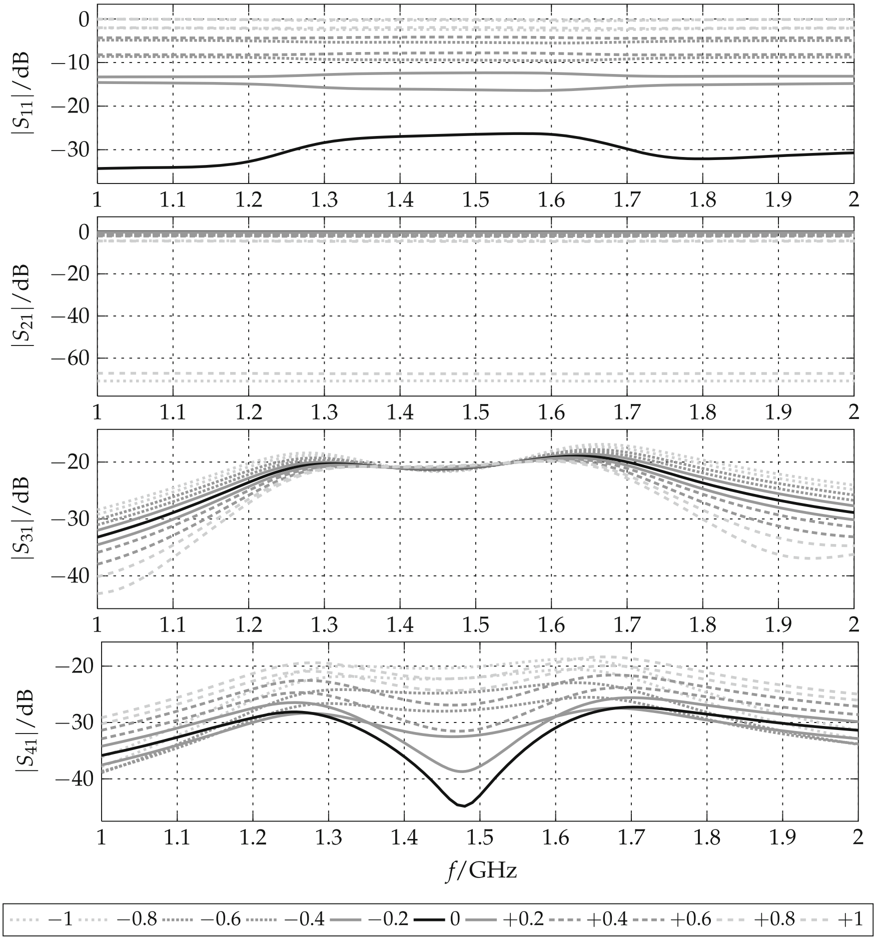

Fig. 5.11 Scattering parameters sweep simulation for different reflection coefficient values $\Gamma_\mathrm{L} = [-1, \ldots, +1]$ of directional coupler 1 with detector diodes and rectification circuit tuned at a center frequency $f_\mathrm{c} = 1.5\,\mathrm{GHz}$. *S-Parameters notation:* S_{11}: *Input reflection.* S_{21}: *Forward transmission.* S_{31}: *Coupling factor* κ. S_{41}: *Isolation*

at the operation frequency of 1.5 GHz, the behavior shows that for $\Gamma_\mathrm{L} = 0$ a value of around −45 dB is achieved, while values approaching a maximum of −20 dB are obtained when the reflection coefficient is evaluated for $\Gamma_\mathrm{L} \to \pm 1$. Finally, regarding the directivity of the directional coupler, an acceptable value of around +25 dB is reached.

5.2.3 Measurements and Performance of Detector Module

Voltage detection measurements considering different reflection coefficients Γ_L, i.e. for different Z_L load impedances, were carried out with the setup shown in Fig. 5.12. A network analyzer was employed at port P1 of the detector module to set up the input signal in terms of frequency and input power. Two digital multimeters to read out the detected voltages at ports 3 and 4, and a source meter for external biasing of the Schottky detector diodes were utilized. Although the Schottky detector typically does not require any external bias for operation, higher detected voltages can be obtained by applying a forward DC bias voltage. Thus, resulting in a larger detection range that benefits the accuracy of the adaptive matching process. The overall setup made use of a GPIB (General Purpose Interface Bus) link for communication via Matlab.

The detector circuit should be equally matched in both branches of the directional coupler, i.e. ports 3 and 4, considering the frequency of operation at which the reflection coefficient is to be monitored. In this way, a symmetric voltage behavior, in the ideal case, can be achieved when evenly negative and positive values of the reflection coefficient Γ_L are evaluated. For example, minimum detected voltage difference for $\Gamma_\mathrm{L} = \pm 1$ and maximum detected voltage difference for $\Gamma_\mathrm{L} = 0$.

An estimation of the maximum voltage difference between ports 3 and 4 of a detector module in terms of the characteristic impedance $Z_{0,\,\text{coupled line}}$ along the coupled line, can be calculated by

$$\frac{\Delta V_{\text{max},\,\text{P}_3-\text{P}_4}}{V} = \sqrt{10^{\frac{\left(\frac{P_\text{in}}{\text{dBm}} - \frac{\kappa}{\text{dB}}\right)}{10}} \cdot 1\text{mW} \cdot \frac{Z_{0,\,\text{coupled line}}}{\Omega}}. \tag{5.2}$$

Thus, the detection of voltage in terms of power for the ideal case takes into account for detector module 1 $Z_{0,\,\text{coupled line 1}} = 50\,\Omega$, and for detector module 2 $Z_{0,\,\text{coupled line 2}} = 126\,\Omega$, both with κ coupling factor. That means, a perfect matching condition with minimum reflection when $\Gamma_\mathrm{L} = 0$, yields

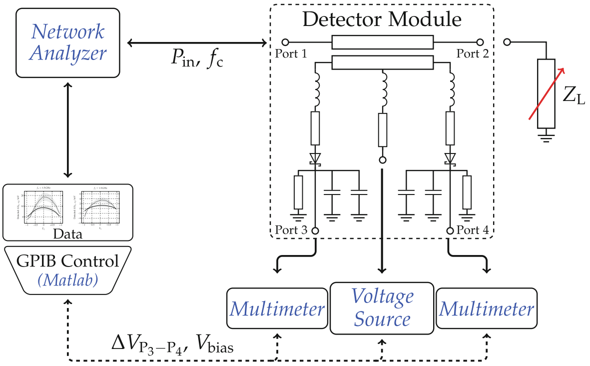

Fig. 5.12 Measurement setup for voltage detector module measurements. The setup is controlled via GPIB communication with different Z_L load impedances to represent a set of Γ_L reflection coefficients

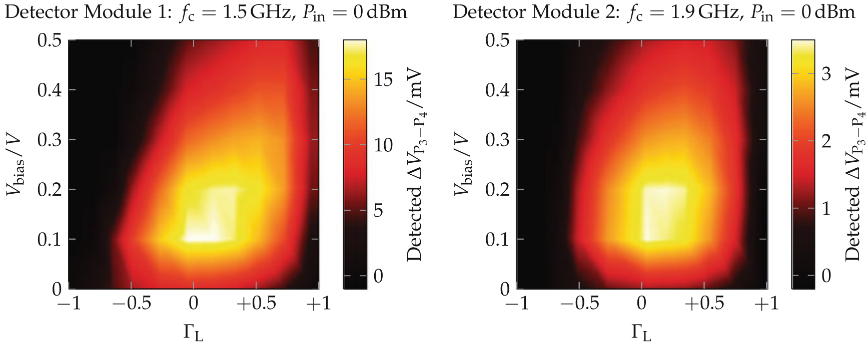

Fig. 5.13 Detected voltage in terms of diode biasing voltage V_{bias}, and reflection coefficient Γ_L at a center frequency f_c for detector modules 1 and 2. Both detector modules exhibit its maximum detected voltage difference $\Delta V_{P_3-P_4}$ at $\Gamma_L = 0$ for external biasing up to $V_{\mathrm{bias}} = 0.1\,\mathrm{V}$

$$\frac{P_{\mathrm{in}}}{\mathrm{dBm}} = \frac{P_{P_1}}{\mathrm{dBm}} = \frac{P_{P_3}}{\mathrm{dBm}} + \frac{\kappa}{\mathrm{dB}} \tag{5.3}$$

without energy at isolation port 4. Therefore, considering the maximum power level of the input signal recommended by the manufacturer, and based on Eq. (5.2) in the case of an input power $P_{\mathrm{in}} = 0\,\mathrm{dBm}$, the maximum voltage difference $\Delta V_{\mathrm{max},\,P_3-P_4}$ results in 22 mV for detector module 1 and 35 mV for detector module 2.

Performance of detector modules considering external biasing voltage V_{bias} from 0 to 0.5 V at the designed center frequency of each detector module is shown in Fig. 5.13. Measurements were performed at frequencies $f_c = 1.5\,\mathrm{GHz}$ for module 1, and at $f_c = 1.9\,\mathrm{GHz}$ for module 2. The resulting detected voltage difference $\Delta V_{P_3-P_4}$ between ports 3 and 4 shows that the maximum detected voltage shifts from a reflection coefficient $\Gamma_L = 0$ towards a value of $\Gamma_L = 1$ when the biasing voltage of the diodes is increased.

In the case of detector module 1, when the detector is operated at $V_{\mathrm{bias}} = 0.1\,\mathrm{V}$, the overall response of the module reaches a detection around 20 mV at $\Gamma_L = 0$ as predicted by Eq. (5.2). In the case of detector module 2, the expected detected voltage of around 35 mV described by Eq. (5.2) is strongly decreased to values around 4 mV. On the one hand, due to fabrication constraints of the soldered elements in the 126 Ω coupled line, resulting in an inaccurate matching for the detector diode. And on the other, due to the range difference shown by the coupling $|S_{31}|$ and isolation $|S_{41}|$ in Fig. 5.10, and thus, decreasing the overall voltage difference.

The maximum detected voltage difference in both modules at $\Gamma_L = 0$ corresponds to an external biasing around $V_{\mathrm{bias}} = 0.1\,\mathrm{V}$. As a consequence of the diode impedance dependence on the saturation current and the externally applied biasing, a symmetric behavior with maximum detected voltage difference at $\Gamma_L = 0$ is observed for lower biasing voltages.

To confirm the correct operation of the detector modules, separated voltage measurements of port 3 and port 4 at $f_c = 1.5\,\mathrm{GHz}$ for module 1, and at $f_c = 1.9\,\mathrm{GHz}$

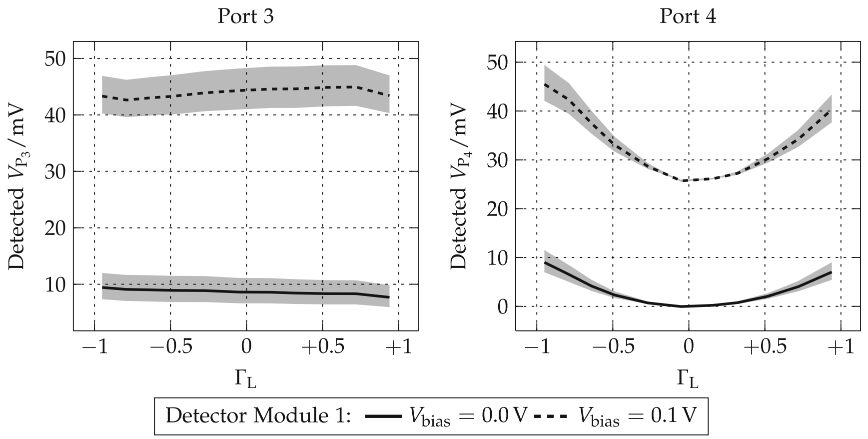

Fig. 5.14 Single port voltage measurements of port 3 and port 4 in terms of the reflection coefficient Γ_L for detector module 1 at $f_c = 1.5$ GHz and input power $P_{in} = 0$ dBm. The *shadowed area* represents evaluation for input power P_{in} between −1 and +1 dB

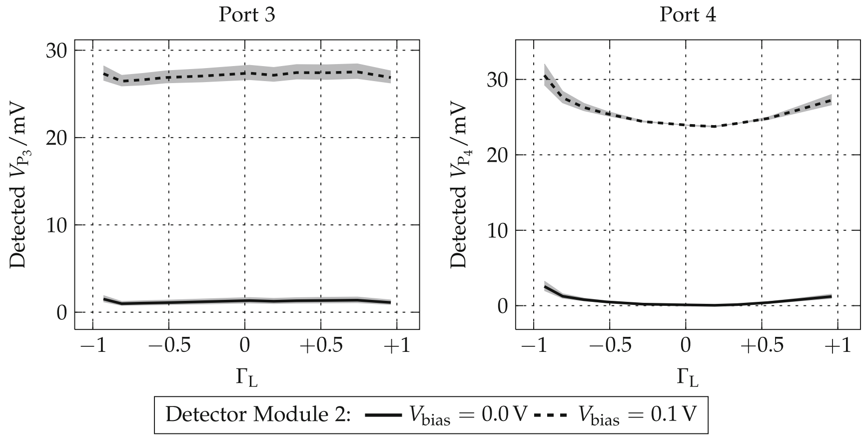

Fig. 5.15 Single port voltage measurements of port 3 and port 4 in terms of the reflection coefficient Γ_L for detector module 2 at $f_c = 1.9$ GHz and input power $P_{in} = 0$ dBm. The *shadowed area* represents evaluation for input power P_{in} between −1 and +1 dBm

for module 2, are shown in Figs. 5.14 and 5.15 respectively. It is clear to observe that while the voltage at port 3 in both modules exhibits a relatively flat and constant response, the behavior of detected voltage at port 4 is different in module 1 than in module 2. In the case of module 1, a sharper bending is obtained at values approaching $|\Gamma_L| \rightarrow 0$ than in the case of module 2, and therefore, resulting in a larger detection range.

In Figs. 5.16 and 5.17 the behavior of modules 1 and 2 is shown in terms of the difference between detected voltages $\Delta V_{P_3 - P_4}$, and the reflection coefficient Γ_L at

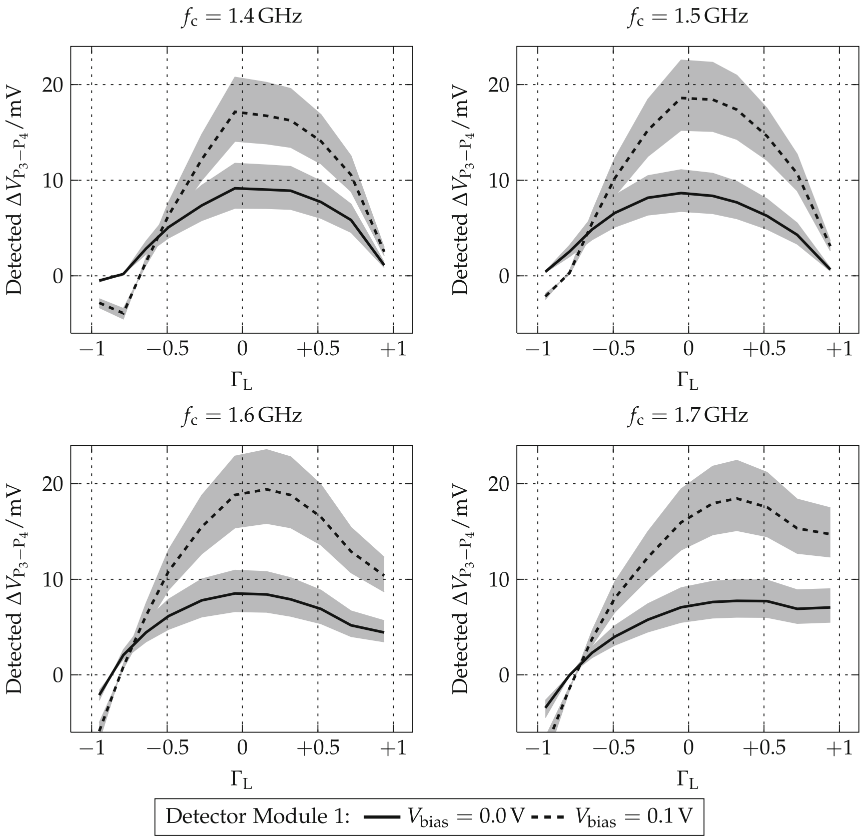

Fig. 5.16 Measured detected voltage for module 1 with 50 Ω main line and coupled line. Measurement of the detected voltage difference $\Delta V_{P_3-P_4}$ between ports 3 and 4 for different reflection coefficient Γ_L values taking into account: center frequency f_c and diode biasing voltage V_{bias}. Working frequency range: from 1.4 to 1.6 GHz with input power $P_{in} = 0\,\mathrm{dBm}$. The *shadowed area* represents evaluation for input power P_{in} between −1 and +1 dBm

different center frequencies f_c. Considering the results of the detector module in terms of diodes' biasing voltage, measurements were performed with and without applying external biasing voltage of the detector diodes with $V_{bias} = 0\,\mathrm{V}$ and $V_{bias} = 0.1\,\mathrm{V}$, and input power $P_{in} = 0\,\mathrm{dBm}$ to investigate the behavior of the detector module in terms of voltage sensitivity[3] and detection range. The shadowed area represents the measured input power from $P_{in} = -1\,\mathrm{dBm}$ and $P_{in} = +1\,\mathrm{dBm}$.

In Fig. 5.16 module 1 exhibits a symmetric behavior at the designed center frequency $f_c = 1.5$ GHz in the case of $V_{bias} = 0\,\mathrm{V}$ and $P_{in} = 0\,\mathrm{dBm}$ with maximum value $\Delta V_{P_3-P_4}$ at $\Gamma_L = 0$. In the other frequency cases, at $f_c = 1.4\,\mathrm{GHz}$ for values

---

[3] Sensitivity of the detector module is here considered as the variation of the resulting voltages from port 3 and port 4 (V_{P_3} and V_{P_4}), with respect to the variation of the reflection coefficient Γ_L at port 2.

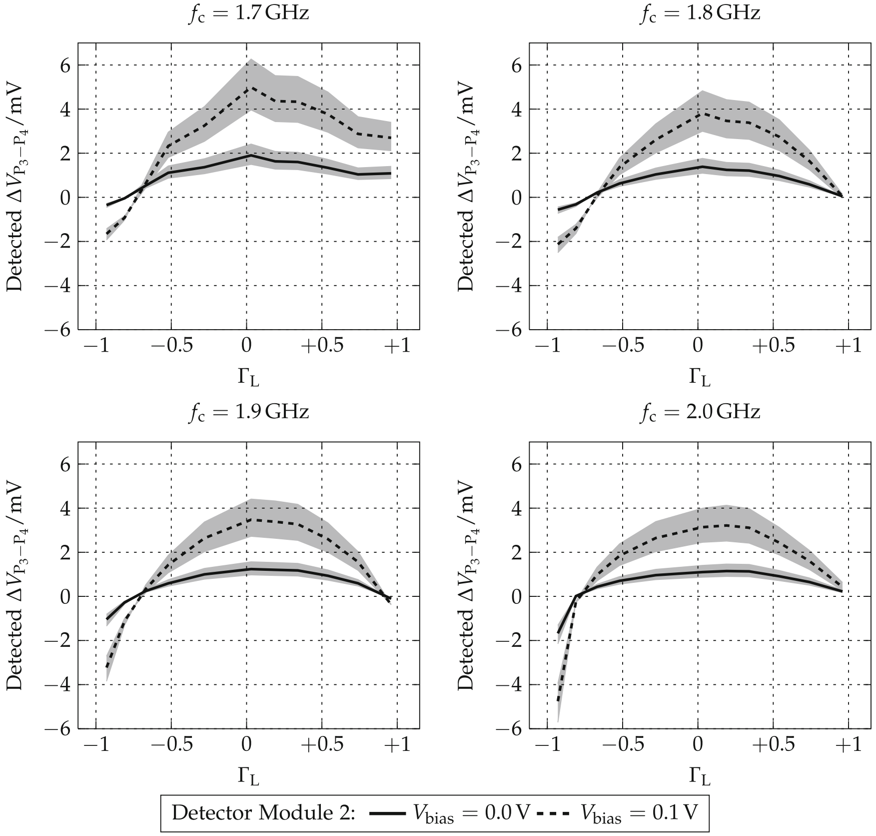

Fig. 5.17 Measured detected voltage for module 2 with 50 Ω main line and 126 Ω coupled line. Measurement of the detected voltage difference $\Delta V_{P_3-P_4}$ between ports 3 and 4 for different reflection coefficient Γ_L values taking into account: center frequency f_c and diode biasing voltage V_{bias}. Working frequency range: from 1.7 to 1.9 GHz with input power $P_{in} = 0\,\text{dBm}$. The *shadowed area* represents evaluation for input power P_{in} between −1 and +1 dB

of $\Gamma_L < 0$ and at $f_c = 1.6\,\text{GHz}$ for values of $\Gamma_L > 0$ although the detected voltage slightly experiences an asymmetric response, the maximum $\Delta V_{P_3-P_4}$ is still located at $\Gamma_L = 0$.

If biasing voltage $V_{bias} = 0.1\,\text{V}$ is applied, the overall response of the module increases the detection range from around 9 mV to almost 20 mV. However, this produces also a change in the impedance of the diode resulting in a stronger asymmetric behavior when the reflection coefficient approaches values $|\Gamma_L| \to 1$.

The asymmetric response arises as a consequence of operation at a different center frequency and biasing voltage of the detector diodes, thus, resulting in an unbalanced matching in the branches at ports P3 and P4 with respect to the impedance of the RF detector under these different conditions. Consequently, this nonlinear effect produces that the maximum detected voltage at a designed f_c and originally centered at $\Gamma_L = 0$, shifts the value itself to a higher reflection coefficient value deforming the overall response. For example, $\Gamma_L = +0.2$ at $f_c = 1.6$ GHz, and $\Gamma_L = +0.3$ with an even stronger asymmetric effect when the frequency is increased to $f_c = 1.7$ GHz.

In Fig. 5.17, it can be seen that module 2 exhibits a symmetric behavior with a maximum detected voltage $\Delta V_{P_3-P_4}$ for a reflection coefficient $\Gamma_L = 0$, i.e. $Z_L = 50\,\Omega$, from 1.7 to 1.9 GHz with and without applying external biasing voltage V_{bias} at input power $P_{in} = 0$ dBm. When the Schottky diodes of the detector module are biased with $V_{bias} = 0.1$ V, the maximum detected voltage difference ΔV_{P3-P4} at $\Gamma_L = 0$ increases from 1 mV to almost 4 mV at 1.9 GHz. At 2.0 GHz, without external biasing, the maximum detected voltage difference $\Delta V_{P_3-P_4}$ is shifted to a value around $\Gamma_L = +0.2$ since the impedance of the diode differs from the matching performed at the designed frequency $f_c = 1.9$ GHz. This effect is more pronounced when external biasing $V_{bias} = 0.1$ V is applied.

The best results can be found as a result of a compromise considering center frequency f_c, detected voltage difference $\Delta V_{P_3-P_4}$, external biasing V_{bias} and symmetry with maximum detected voltage with respect to Γ_L. In the case of detector module 1 at $f_c = 1.5$ GHz without external biasing this corresponds to a value $V_{bias} = 0$ V. And for detector module 2 at $f_c = 1.9$ GHz with external biasing $V_{bias} = 0.1$ V.

An overview of the aforementioned cases with input power $P_{in} = 0$ dBm is shown in Fig. 5.18. With this power a frequency sweep from 1.4 to 1.7 GHz for detector module 1, and from 1.6 to 2.0 GHz for detector module 2 is performed. While module 1 exhibits a good performance with maximum $\Delta V_{P_3-P_4}$ for $\Gamma_L = 0$ and minimum $\Delta V_{P_3-P_4}$ for $|\Gamma_L| = 1$ from 1.4 to 1.6 GHz with detected voltages of around $\Delta V_{P_3-P_4} = 7$ mV, module 2 operates from 1.7 to 2.0 GHz with detected voltages of around $\Delta V_{P_3-P_4} = 4$ mV.

To provide an overview of detector modules 1 and 2 in terms of the input power P_{in} tolerance, measurements of both modules are shown in Fig. 5.19. The measurements

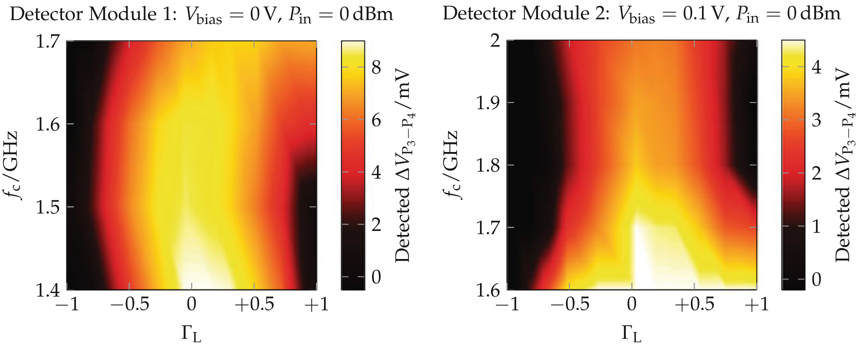

Fig. 5.18 Overview of voltage detector modules 1 and 2 in terms of the frequency range of operation f_c at a fixed externally biasing voltage $V_{bias} = 0.1$ V. Detector module 1 with operation range from 1.4 to 1.6 GHz. Detector module 2 with operation range from 1.7 to 2.0 GHz

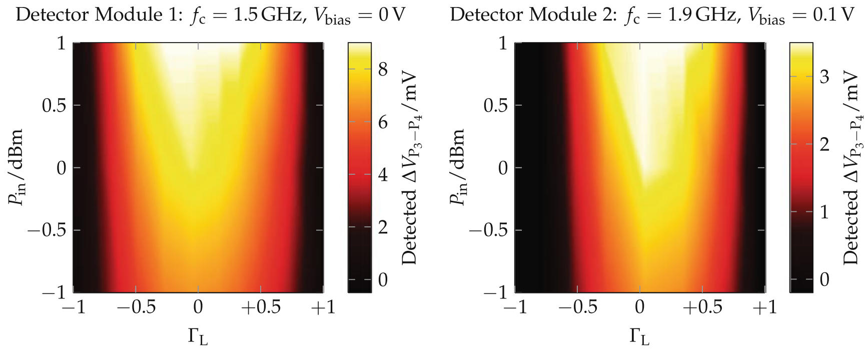

Fig. 5.19 Overview of voltage detector modules 1 and 2 in terms of the input power P_{in} at a frequency of operation $f_c = 1.5\,\text{GHz}$ for detector module 1 and $f_c = 1.9\,\text{GHz}$ for detector module 2 without external diode biasing voltage V_{bias}

are performed at its corresponding center frequency of operation f_c without external biasing, i.e. 1.5 and 1.9 GHz.

It can be seen in both cases that the influence in the variation of the input power P_{in} from −1 to +1 dBm is almost negligible. When the input power is increased, it produces higher detected voltages for a reflection coefficient $\Gamma_L = 0$ in both modules without affecting the symmetry in the remainder Γ_L values. In the case of module 1, a maximum variation of around ±2.4 mV with $\Delta V_{P_3-P_4} = 8.6\,\text{mV}$ is observed, and for module 2 of around ±1 mV with $\Delta V_{P_3-P_4} = 3.4\,\text{mV}$. For both modules a relative voltage variation of 30 % with respect to the maximum value at $\Gamma_L = 0$ is shown.

It has been shown in Fig. 5.18 that both detector modules perform well at a determined range of frequencies. Particularly at the designed center frequencies even with almost perfect symmetry as shown in Fig. 5.19, i.e. at $f_c = 1.5\,\text{GHz}$ for module 1, and at $f_c = 1.9\,\text{GHz}$ for module 2. However, to confine the proposed adaptive control approach, presented results require to be interpreted considering the voltage sensitivity of the detector modules. That means, the variation of the reflection coefficient in terms of the detected voltage difference $\Delta V_{P_3-P_4}$ at ports 3 and 4 of the directional coupler.

In Fig. 5.20, a numerical comparison considering the magnitude of the reflection coefficient $|\Gamma_L|$ in decibels compared to the detected voltage difference $\Delta V_{P_3-P_4}$ for both detector modules is shown. The magnitude reflection coefficient is considered to clearly observe the behavior of its negative and positive values in the same coordinate plane. This behavior determines whether the optimization algorithm (i) minimizes the cost function to a determined detected voltage in the case of a symmetric response, e.g. at 1.5 GHz for detector module 1 to obtain a reflection coefficient with at least −10 dB and $\Delta V_{P_3-P_4} = 8\,\text{mV}$; or (ii) maximizes the cost function to find the extreme value of the detected voltage in an asymmetric response, i.e. when a detected voltage difference $\Delta V_{P_3-P_4}$ represents two values of the reflection coefficient Γ_L.

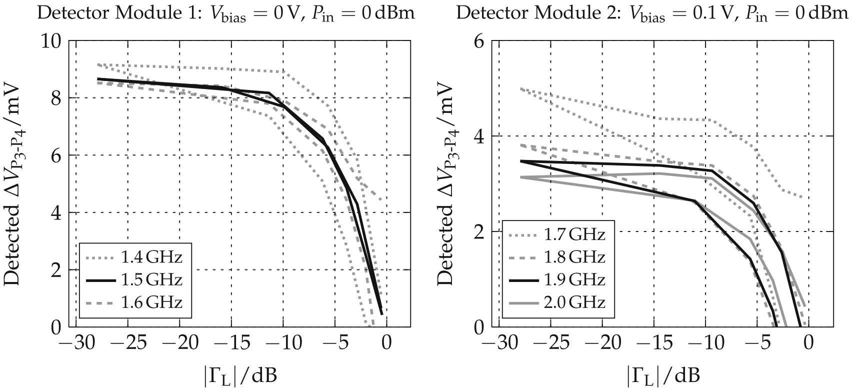

Fig. 5.20 Sensitivity performance of detector modules 1 and 2 at different operation frequencies f_c. The analysis considers the variation of detected voltage difference $\Delta V_{\text{P}_3-\text{P}_4}$ in terms of the absolute value of the reflection coefficient Γ_{L}. Depending on the operation frequency, while for module 1 the optimum value lies at around 9 mV, for module 2 this value lies between 3 and 5 mV

Different conclusions can be drawn from this analysis. At the designed center frequencies, detector module 1 shows a more symmetric behavior compared to detector module 2, i.e. at $f_c = 1.5$ GHz and $f_c = 1.9$ GHz respectively. Considering the operation bandwidth where at least the −10 dB matching condition can be achieved by finding the maximal value of $\Delta V_{\text{P}_3-\text{P}_4}$, module 1 can operate within a 200 MHz bandwidth from 1.4 to 1.6 GHz, yielding 13 % of relative bandwidth. In the same way, module 2 can operate within a 300 MHz bandwidth from 1.7 to 2.0 GHz, yielding 16 % of relative bandwidth. Regarding the detected voltage difference $\Delta V_{\text{P}_3-\text{P}_4}$, while module 1 is more sensitive reaching values around 9 mV, module 2 can find the best optimum value with voltages between 3 and 5 mV. However, to overcome this drawback, amplification of the detected voltage can be performed together with post processing and a high resolution A/D converter.

Considering previous results, to perform an adaptive control via tunable matching network, the detected voltage difference $\Delta V_{\text{P}_3-\text{P}_4}$, i.e. the monitored signal, has to be amplified to a voltage value suitable for the operation voltage range of the A/D converter from 0 to 5 V. To realize this task, the instrumentation amplifier INA116 from manufacturer Texas Instruments [28] and the 20-bit A/D converter LTC2377 from manufacturer Linear Technology [29] were employed (Appendix A.4). Considering the full range of the 20-bit A/D converter, discrete steps of around 5 µV can be obtained. The discretization voltage, shown in Table 5.1, considers the maximum voltage difference of each module at a reflection coefficient Γ_{L}. This yields for detector module 1 at 1.5 GHz steps of 8.6 nV, and in the case of detector module 2 at 1.9 GHz steps of 3.5 nV, when the instrumentation amplifier is set to a voltage gain of 540 and 1450 to cover the A/D converter range of 5 V.

To achieve a finer symmetric detection of the impedance variations in terms of the reflection coefficient Γ_{L}, and to increase the sensitivity of the detector module

Table 5.1 Discretization of voltage steps considering maximum voltage difference $\Delta V_{\text{max, P}_3-\text{P}_4}$ of detector modules at a center frequency, and required amplification gain to operate the 5 V voltage range of the 20-bit A/D converter

Module	f_c/GHz	$\Delta V_{\text{max, P}_3-\text{P}_4}$/mV	Voltage gain	$V_{\text{ADC steps}}$/μV	$V_{\text{Detector steps}}$/nV
1	1.5	8.65	540	5	8.6
2	1.9	3.47	1450	5	3.5

considering the voltage steps, a refinement in the branches of the coupled line can be carried out. This improvement takes into account the impedance of the detector diodes at the specific operation frequency or frequency range. Specifically, in the case of module 2, where soldering of components resulted in a challenging task due to the reduced width of the 126 Ω line, optimization of the matching balance at the terminals of the coupled line results in higher detected voltages. Furthermore, a compromise between the voltage range of the A/D conversion and voltage step of the detector module can be found. This compromise allows to obtain an accurate conversion without using all bits for digital conversion. Hence, resulting in reduced computation times to find the optimum matching value.

Taking into account the frequency of operation of the dualband antenna and tunable matching network module of the overall antenna architecture presented in this work, module 2 is selected. The performance shown by detector module 2 is compatible and in good agreement for functionality in terms of detected voltage to combine it with the remainder stages of the architecture shown in Fig. 5.6, i.e. instrumentation amplifier and A/D converter. Thus, according to the required specifications for further post-processing of the monitored signal by the D/A converter and the HV Charge-Pump, adaptive reconfiguration in the lower band of the dualband antenna can be performed.

5.2.4 FPGA-Control Based WARP Radio

To process the influence of the reflections at the antenna port, i.e. to detect and to read out the output voltages from the detector module, an FPGA is employed. The FPGA of the WARP board integrates a microcontroller core, MicroBlaze. This soft processor core, mainly designed for Xilinx FPGAs, is in charge of running the designed code. That means, tasks such as programming and running of diverse test and control algorithms can be also performed. For example, to select the correct tuning state of the varactors in the matching network module. In Fig. 5.21, an FPGA embedded in a WARP (Wireless Open-Access Research Radio) Radio v3 Board is shown [30].

Out of the scope of this work, however, foreseeing the further development of the overall reconfigurable architecture, significant advantages to use the WARP platform

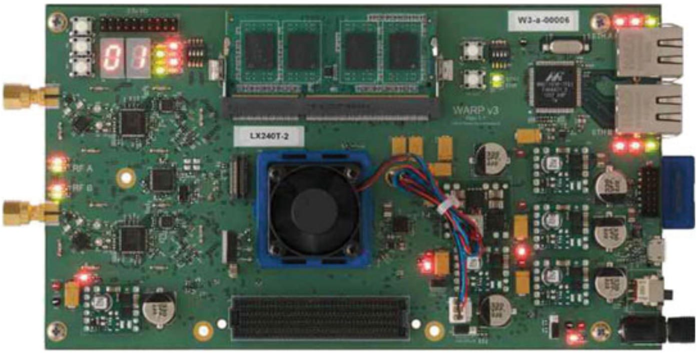

Fig. 5.21 WARP Radio v3 Board with RF modules at 2.4 and 5 GHz, FPGA Xilinx Virtex-6 and diverse I/O ports for connection with external hardware and software modules [30]

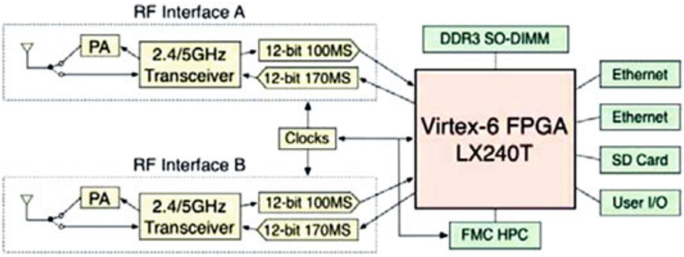

Fig. 5.22 Simplified block diagram of the WARP Radio v3 Board [30]

are to be mentioned. As one of the most important reasons for its employment is that this radio can directly perform digital baseband processing. In this way, no additional hardware for this part is required when a full analysis from the RF down to the baseband and vice versa is intended to be performed. Furthermore, other tasks can be implemented like interconnection with other hardware RF modules such as the Lime Microsystems Board (Chap. 3), or with other software tools for digital analysis such as Matlab/Simulink (Chap. 4).

The block diagram shown in Fig. 5.22 provides an overview of the WARP Board hardware design. The radio includes two Rx/Tx RF interfaces at 2.4 and 5 GHz. For this implementation, an Ethernet module, as well as User I/O of the WARP board together with an FMC (FPGA Mezzanine Card) module are used to set the necessary registers at the inputs of the high-voltage CMOS D/A converter, and hence, to tune the matching network module.

5.3 Reconfigurable Module Measurements

The reconfigurable antenna module was developed in two stages to carry out the proof of concept that integrates operation of the dualband antenna with adaptive control of the tunable matching network, high-voltage charge pump and D/A converters.

In the first stage, based on the block diagram of Fig. 5.1 a prototype for evaluation of the dualband antenna module is shown in Fig. 5.23. In the case of the D/A converters, switches (bottom left) are used to change the input code so that different tuning voltages can be generated. Thus, reconfiguration of the antenna is performed by changing the capacitance of the varactors in the TMN module.

In the second stage, to overcome the necessity to employ switches for control of the matching network, an adaptive control module based on a voltage detector module is included. The embedded FPGA in the WARP module together with voltage translator are employed to set up the D/A converters that provide the high voltage to tune the matching network module (Appendix A.5). Based on the block diagram of Fig. 5.6, the overall reconfigurable antenna architecture based on a dualband dielectric resonator antenna, ferroelectric tunable matching network, CMOS D/A converters with high-voltage charge pump supplied by a 3.7 V battery and the adaptive control is shown in Fig. 5.24.

The complete setup was measured to verify the voltage stability of the HV charge pump in joint functionality with the D/A converters, matching network and antenna. Furthermore, the control for the independent tuning of the monopole band at $f_c = 1.9$ GHz and its influence over the DRA band $f_c = 5.1$ GHz was investigated. Thus, different detuning cases were performed by simple reallocation or positioning of the antenna near metallic surfaces and the human body, e.g. next to the head or covered by the hand.

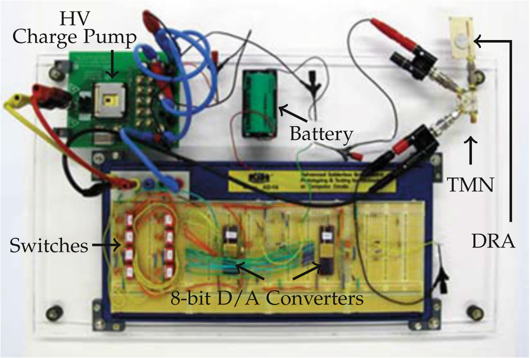

Fig. 5.23 Photo of the reconfigurable antenna demonstrator prototype. The setup for evaluation is integrated by DRA, ferroelectric matching network, HV charge pump supplied by a 3.7 V battery, D/A converters and dip switches for voltage control. The realized demonstrator has been developed within the framework of the LOEWE research priority program Cocoon "Cooperative Sensor Communication"

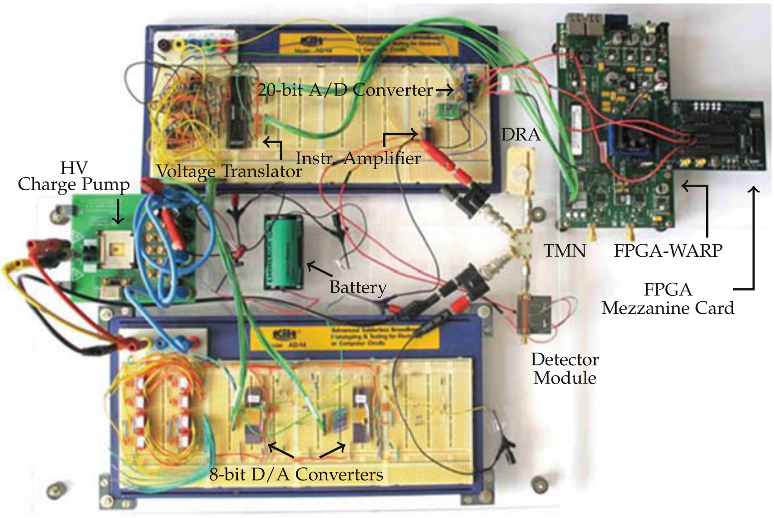

Fig. 5.24 Photo of the complete reconfigurable antenna demonstrator prototype. The setup for evaluation is integrated by DRA, ferroelectric matching network, HV charge pump supplied by a 3.7 V battery, D/A converters and adaptive DC control based on directional coupler with detector diodes, instrumentation amplifiers and FPGA embedded in a WARP Radio platform. The realized demonstrator has been developed within the framework of the LOEWE research priority program Cocoon "Cooperative Sensor Communication"

Fig. 5.25 Measured input reflection for different evaluated cases (matched/unmatched) of the DRA input impedance

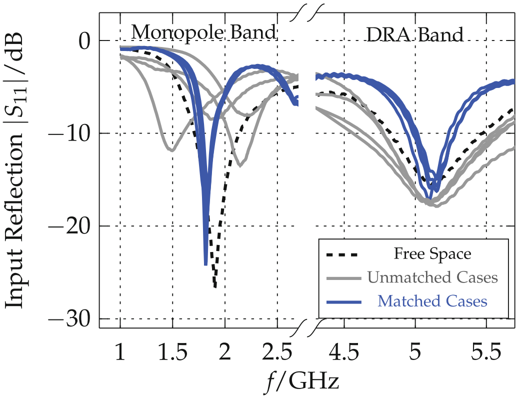

Measurement results of the input matching $|S_{11}|$ with and without matching for different cases of the dualband antenna are shown in Fig. 5.25. While strong mismatch in the lower band of the antenna is clearly observed by the influence of the detuning, in the upper band this influence is almost negligible in all cases since reflection values of around −15 dB are hold. In this way, the detuning influences mainly the monopole band by shifting the center frequency of the antenna into a lower or higher frequency, i.e. from 1.5 to 2.3 GHz, or by reducing the reflection to values worse than −10 dB.

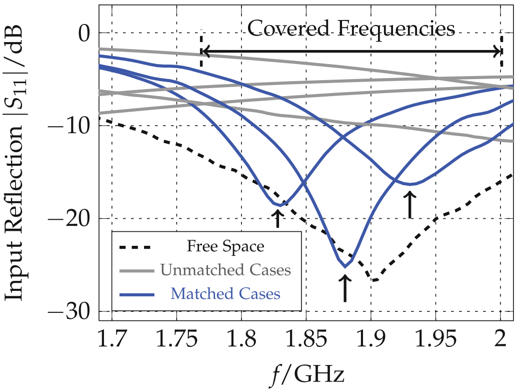

Fig. 5.26 Matching of the monopole band considering a spectrum sensing approach. Matching performed across different E-UTRA frequency operating bands for LTE (bands 2, 3, 9, 33, 35–37, 39) [31]

To compensate the observed mismatch of the lower band, the required tuning voltages of the matching network were applied. In this case a fine matching tuning approach at a fixed frequency is applied. Thus, the center frequency of the antenna is stabilized at the desired center frequency of 1.88 dB with reflection values around −25 dB. Furthermore, it can be seen that both bands become narrower when the $|S_{11}| \leq -10$ dB matching condition of the monopole band is satisfied by the TMN module, i.e. maximum 10 % of the total energy is reflected. For the lower band, the antenna bandwidth is reduced from 420 to 110 MHz, and for the upper band from 640 to 270 MHz, i.e. the antenna becomes more selective by 74 and 57 %, respectively.

Further focusing on the matching of the monopole band, to exemplify the spectrum sensing approach, matching across different frequency bands is shown in Fig. 5.26. Multiple measurements considering different biasing voltages of the tunable matching network show allocation of different operation frequencies for LTE. Compared to the results shown in Fig. 5.25, where a fine matching is demonstrated at a fixed frequency, in this case, tuning of the center frequency is performed covering diverse bands between 1.8 and 2 GHz with an input reflection $|S_{11}|$ better than −10 GHz.

In overview, three facts have been successfully faced to carry out the demonstration of the reconfigurable antenna proof of concept: the first one, is the accurate generation of the required tuning voltages for operation of the TMN module, i.e. by means of CMOS integrated circuits. The second one, is the monitoring of the signal that triggers the decision, if reconfiguration is whether necessary to be performed or not. And the last one, complemented by the first one and the latter, is that the architecture is able to adaptively reconfigure the hardware via software. This means, an FPGA-WARP embedded module is employed, where the monitoring and control methodology for the matching network can be programmed and therefore, to provide the required high voltage for the matching network.

After the proof of concept presented throughout this work, a general on-chip integration of the complete architecture is strongly recommended so that this prototype is enabled for commercial use within a portable device, hence, offering another possibility to employ reconfigurable devices. Furthermore, an optimization of the individual modules that integrate the architecture could improve the overall performance by following further considerations:

The presented approach has been demonstrated employing a dualband antenna. However, a wide variety of antennas can be used according to the required application considering, e.g. covered bands, compactness, gain, and directivity.

On the tunable matching network, important factors are the frequency range of operation, required tuning speed, required voltage, power consumption, linearity, and supported bandwidth according to the employed material to reconfigure the tunable device. However, apart from semiconductor technology and ferroelectric films, liquid crystal and RF MEMS take also a prominent place as an attractive solution to introduce tunability.

The frequency range of operation regarding the RF detector matching circuit together with the directional coupler are of primary importance. Thus, technology refinements such as soldering and investigation of diverse diodes to increase voltage sensitivity within a frequency range can avoid the use of an amplification stage for A/D conversion. On-chip integration can be another option to reduce the size of the overall module. Due to the reduced size of mobile devices, design of MIMO antenna systems require to cope with the intrinsic coupling between the antennas of the user equipment. By combining the presented detector module with tunable couplers, this concept can be further developed for MIMO applications to compensate the introduced coupling due to the employment of multiple antennas to cover different Tx/Rx bands, e.g. to enable spatial diversity or spatial multiplexing.

On the voltage of the reconfigurable antenna module, stacking of the integrated CMOS circuits, i.e. HV charge pump and D/A converter, can reduce the size of the footprint. Compatibility of the required input voltage between the FPGA and A/D converter can be performed to reduce the amount of employed external elements, such as voltage translator and inverting amplifiers.

Finally, apart from the required processing and refinement of the hardware part for enhancement of the RF-Frontend, integration and verification of the baseband processing including software and algorithms should be performed. In this way, architecture limitations in terms of digital measures can be also identified. Furthermore, although this demonstrator employs a narrowband antenna, the developed approach can be used targeting UWB antennas such as employed in the wide tuning range architecture presented in Chap. 3. However, the limitation is the inherent frequency dependence, and hence, driven bandwidth of state-of-the-art components.

Hence, the importance of this architecture resides fundamentally in ensuring a certain quality of service. That is, not only during a simple telephone call, but also in scenarios with high-quality demands. Such is the case of video resources or remote controlling of objects in sensor networks when portable devices are subject to different conditions, and thus, arising effects that severely alters the required performance.

References

1. G. Moore, Cramming more components onto integrated circuits. Proc. IEEE **86**(1), 82–85 (1998)
2. D. DeReus, S. Natarajan, S. Cunningham, A. Morris, Tunable capacitor series/shunt design for integrated tunable wireless front end applications, in *2011 IEEE 24th International Conference on Micro Electro Mechanical Systems (MEMS)* (2011), pp. 805–808
3. K. Hofmann, L. Shen, E. González-Rodríguez, H. Maune, D. Dahlhaus, R. Jakoby, Fully integrated high voltage charge pump for energy-efficient reconfigurable multi-band rf transceivers, in *IEEE International Telecommunications Energy Conference (INTELEC)* (2012)
4. J. Ning, L. Shen, E. Gonzáez, K. Hofmann, An integrated high voltage digital-to-analog converter for a reconfigurable antenna array. Analog Integr. Circuits Signal Process. **80**, 407–415 (2014)
5. J. McLean, A re-examination of the fundamental limits on the radiation q of electrically small antennas. IEEE Trans. Antennas Propag. **44**, 672 (1996)
6. Y. Zheng, A. Giere, R. Jakoby, A compact antenna with two independently tunable frequency bands, in *Antennas and Propagation Society International Symposium, 2008. AP-S 2008. IEEE*, July 2008, pp. 1–4
7. A. Mehmood, Y. Sun, Y. Zheng, O. H. Karabey, H. Braun, M. Hovhannisyan, M. Letz, R. Jakoby, Compact dual-band hybrid dielectric resonator antenna based on new glass-ceramic material, in *European Microwave Conference (EuMC)* (2013), pp. 763–766
8. M. Hovhannisyan, H. Braun, Y. Zheng, A. Mehmood, M. Letz, R. Jakoby, Bulk-glass ceramics with two microwave crystalline phases for antenna elements in wireless communications, in *Ferroelectrics Conference Sheffield, UK*, February 2013
9. 3GPP tr 36.814 v9.0.0 LTE technical specification group radio access network; evolved universal terrestrial radio access (E-UTRA); further advancements for E-UTRA physical layer aspects (release 9) (2010)
10. A. Petosa, *Dielectric Resonator Antenna Handbook* (Artech House, Norwood, 2007)
11. J. Shin, I.-Y. Chung, Y.-J. Park, H.S. Min, A new charge pump without degradation in threshold voltage due to body effect [memory applications]. IEEE J. Solid-State Circuits **35**(8), 1227–1230 (2000)
12. R. Pelliconi, D. Iezzi, A. Baroni, M. Pasotti, P. Rolandi, Power efficient charge pump in deep submicron standard cmos technology. IEEE J. Solid-State Circuits **38**(6), 1068–1071 (2003)
13. E.D. Mishina, N.E. Sherstyuk, V.I. Stadnichuk, A.S. Sigov, V.M. Mukhorotov, Y.I. Golovko, A. van Etteger, T. Rasing, Nonlinear-optical probing of nanosecond ferroelectric switching. Appl. Phys. Lett. **83**(12), 2402–2404 (2003)
14. M. Pelgrom, A.C.J. Duinmaijer, A. Welbers, Matching properties of mos transistors. IEEE J. Solid-State Circuits **24**(5), 1433–1439 (1989)
15. Q. Guo, R. Mittra, F. Lei, Z. Li, J. Ju, J. Byun, Interaction between internal antenna and external antenna of mobile phone and hand effect. IEEE Trans. Antennas Propag. **61**, 862–870 (2013)
16. J. Ilvonen, O. Kivekas, J. Holopainen, R. Valkonen, K. Rasilainen, P. Vainikainen, Mobile terminal antenna performance with the user's hand: effect of antenna dimensioning and location. IEEE Antennas Wirel. Propag. Lett. **10**, 772–775 (2011)
17. C.-H. Li, E. Ofli, N. Chavannes, N. Kuster, Effects of hand phantom on mobile phone antenna performance. IEEE Trans. Antennas Propag. **57**, 2763–2770 (2009)
18. Y. Zheng, H. Maune, A. Giere, M. Sazegar, R. Jakoby, Constraints on efficient control of tunable impedance matching network based on barium-strontium-titanate thick-film varactors, in *38th European Microwave Conference, EuMC* (2008)
19. T. Coleman, Y. Li, An interior, trust region approach for nonlinear minimization subject to bounds. SIAM J. Optim. **6**, 418–445 (1996)
20. D. Qiao, Y. Zhao, T. Hung, D. Kimball, M. Li, P. Asbeck, D. Choi, D. Kelly, Antenna impedance mismatch measurement and correction for adaptive cdma transceivers, in *Proceedings IEEE MTT-S International Microwave Symposium Digest* (2005), pp. 783–786

21. H. Maune, Y. Zheng, M. Sazegar, A. Giere, R. Jakoby, Compact devices for complex wave monitoring for tunable impedance matching networks. Frequenz **3–4**, 63–65 (2009)
22. H. Hedayati, M. Mobarak, G. Varin, P. Meunier, P. Gamand, E. Sanchez-Sinencio, K. Entesari, A 2-ghz highly linear efficient dual-mode bicmos power amplifier using a reconfigurable matching network. IEEE J. Solid-State Circuits **47**, 2385–2404 (2012)
23. H. Maune, M. Sazegar, R. Jakoby, Tunable impedance matching networks for agile rf power amplifiers, in *2011 IEEE MTT-S International Microwave Symposium Digest (MTT)*, June 2011, pp. 1–4
24. D. Pozar, *Microwave Engineering* (McGraw-Hill, New York, 1998)
25. Avago Technologies HSMS-285x Series Datasheet. Surface Mount Zero Bias Schottky Detector Diode (2009)
26. H.W. Bode, *Network Analysis and Feedback Amplifier Design* (D. Van Nostrand Company, Toronto, 1945)
27. R.M. Fano, Theoretical limitations on the broadband matching of arbitrary impedances, Technical report, Massachusetts Institute of Technology, Research Laboratory of Electronics, January 1948
28. Texas Instruments INA116 Datasheet. Ultra Low Input Bias Current Instrumentation Amplifier (2009)
29. Linear Technology LTC2377 Datasheet. Low Noise, Low Power, High Speed 20-bit Successive Approximation Register (SAR) ADC (2013)
30. WARP Project Website (2014)
31. LTE; evolved universal terrestrial radio access (e-utra); user equipment (ue) conformance specification; radio transmission and reception; part 1: Conformance testing (3gpp ts 36.521-1 version 10.4.0 release 10). etsi ts 136 521-1 v10.4.0 (2013-02) (2013)

Chapter 6
Summary and Outlook

In this work, focusing on reconfigurable transceiver architectures, a thorough investigation is given relying on proposed approaches and demonstrated hardware implementations. Such architectures can target innovative communication systems such as multiband and multistandard cognitive radios, software-defined-radios, wireless sensor networks handling diverse sources of information, e.g. smart environments, RFID and car-to-car communications, among others, together with current and future mobile communications like IMT-Advanced 4G and not yet standardized 5G.

It has been shown by means of one hardware architecture, that by employing state-of-the-art technologies, transmission and reception of signals can be achieved from the baseband part up to the RF part within a continuous frequency range up to 7 and 6 GHz, respectively. This concept includes a commercial available RF-signal processor from the manufacturer Lime Microsystems and a mixer module from the manufacturer RFMD along with wideband characteristic components. For further development of this hardware demonstrator, a refinement process focusing on a dedicated application should be performed, particularly bearing in mind diverse factors such as compactness of the antenna and circulator. Compatibility of the required operation frequency range among the diverse elements can be optimized, e.g. mixer and amplification stages. In the case of the mixer module, wider matching of at least 3 GHz can greatly improve the performance of extended transmission and reception frequency bands. Similarly, considering the employed circulator, a key factor is to increase its 3 dB bandwidth and isolation between Tx and Rx signal paths. Ideally, a compact wideband tuning duplexer could satisfy size and frequency requirements. Yet, state-of-the-art technology is not able to cover such wide frequency range. Consequently, a discretization of the wide frequency range can fulfill this requirement, e.g. by exploiting the tuning range of agile components such as phase shifters, amplifiers, filters and matching networks. Standing as potential candidates to realize this kind of components, aside from the well-established semiconductor technologies, MEMS and ferroelectric materials take a prominent place.

E. Gonzalez Rodriguez, *Reconfigurable Transceiver Architecture for Multiband RF-Frontends*, Smart Sensors, Measurement and Instrumentation 17,
DOI 10.1007/978-3-319-24581-2_6

Another primary contribution of this work, is the comprehensive investigation of the influence on system performance of the frequency dispersion targeting RF microwave tunable components, concretely, for reconfigurable architectures. Initially this topic dealt with a non tunable component to understand the fundamental behavior of this nonlinear effect, and afterwards by introducing an agile multiband component, i.e. a tunable impedance matching network. This investigation provides a bridge between the analog and digital worlds to demonstrate and to facilitate a relation between RF and baseband characteristics. That is, the characterization in terms of scattering parameters together with Bit Error Rate and Error Vector Magnitude. Hence, this results in an attractive approach to consider during the development process and utilization of such agile components, e.g. (i) to determine whether a component fulfills certain metrics and standards within a communication system, and (ii) to decide if a component reconfiguration is required at system level architecture considering aforementioned characteristics.

The complete analysis of the simulated filters as well as for the measured tunable impedance matching network has been performed by an implemented testbed developed in Matlab and Simulink assuming a $50\,\Omega$ environment. This testbed, together with a software and hardware implementation, were also used as the basis within the framework of the AiF[1] funded project "Entwicklung eines Modellsystems zur Charakterisierung der Übertragungsstrecken von industriellen Netzwerken zwischen Satellitenantenne und Receiver" (eng. "Development of a System Model for Characterization of Transmission Paths between the Satellite Antenna and the Receiver of Industrial Networks").

In effect, from a theoretical analysis based on filter characteristics, the influence of a nonlinear phase response is studied and evaluated resulting in group delay variations over the Bit Error Rate. A comparison between a flat filter and filter with ripples of 0.5 dB in the amplitude response, has shown that the joint influence of the amplitude, phase, and as consequence in the group delay across a defined signal bandwidth, raises a degradation of more than 2.5 dB in the signal-to-noise ratio for an error probability of at least 1×10^{-4} in a 16-QAM scheme.

The analysis of phase nonlinearities was also extended by the investigation of a tunable impedance matching network based on ferroelectric varactors with center frequency at $f_c = 1.9\,\text{GHz}$. The importance of these kind of components resides in the fact that they can ensure a defined signal quality and mitigate the effect of distortion sources at the input of the antenna in a portable device. The performance shown by its measured scattering parameters, and also represented in terms of the Bit Error Rate and Error Vector Magnitude places this functional material as a good candidate for employment in reconfigurable architectures. On the RF side, the TMN module has exhibited a maximum variation of the insertion loss of less than 0.2 dB and a return loss of less than −11 dB considering a tuning range from 1.8 to 2.0 GHz with tuning voltages up to 90 V.

---

[1] AiF: Arbeitsgemeinschaft industrieller Forschungsvereinigungen—eng. German Federation of Industrial Research Associations.

On the digital side at a component level, it can be considered the dispersion of the tunability from the untuned state to the maximum tuned state at an error probability of 1×10^{-6} for comparison. Also different digital modulation schemes are considered yielding noticeable variations in the SNR. For a QPSK digital scheme, a negligible influence is exhibited for signal bandwidths of 20 and 40 MHz. For the 16-QAM scheme, a variation in the SNR of up to 1 dB is present between untuned and maximum tuned state when a signal bandwidth of 40 MHz is tested. And finally, for the 64-QAM scheme, signals with a narrower bandwidth of at least 20 MHz have shown a difference in the SNR of 2 dB from the untuned state to the maximum tuned state. In terms of the error vector magnitude, digital modulation schemes QPSK, 16-QAM and 64-QAM have shown comparable good results to required levels established by current mobile standards, e.g. GSM, UMTS and LTE. These comparable EVM results considering the tunability of the matching network from the untuned state to the maximum tuned state, exhibited a variation of less than 0.4 % for 64-QAM scheme, less than 0.3 % for the 16-QAM scheme, and less than 0.1 % in the case of the QPSK scheme.

Another major contribution of this work, is the adaptive antenna matching approach that accurately controls the varactors in a matching network taking into account a high voltage in the range of 100 V. For this reason, to connect the digital analysis regarding the tunability in terms of scattering parameters with a tangible experimental comparison, a hardware implementation was developed during this work. This implementation enables the use of an adaptive control for matching networks exploiting tunable capacitances requiring voltages that today's devices, e.g. mobile phones and tablets, currently cannot sustain. Apart from the required high voltage, a precise control is also necessary, thus, resulting in a challenging task when targeting portable applications.

To demonstrate this approach under different real scenarios, an architecture is developed employing components based on different technologies. That is, the aforementioned TMN module with a dielectric resonator antenna based on glass-ceramics operating at 1.9 and 5 GHz, and a CMOS high voltage charge pump with digital analog converter capable to overcome the integration constraint of high-voltage in portable devices. This reconfigurable antenna module is complemented with a detector module based on directional coupler and RF Schottky diodes, and an embedded FPGA in a wireless open-access research radio. The developed method to perform an adaptive control of the varactors in a matching network was exemplary demonstrated for a narrowband antenna. However, this approach can also be applied to other kind of antennas, e.g. for compact tunable multiband antennas or the monopole antenna employed in the wide tuning transceiver architecture.

The demonstrators, such as the wide tuning transceiver architecture, and the reconfigurable antenna architecture have been developed within the framework of the LOEWE[2] research priority program Cocoon "Cooperative Sensor Communication". Furthermore, the results of this work are currently of special interest for development of a dedicated research area.

---

[2] LOEWE: Landes-Offensive zur Entwicklung Wissenschaftlich-Oekonomischer Exzellenz.

Potential for further development and refinement of the demonstrators has been thoroughly identified by revising the characteristic of each component and the influence over the complete architectures. However, another major focus of examination is the study in real time of different algorithms for hardware control, as well as to enable a flexible platform that extends the characterization and testing themselves. For example, in terms of digital and analog measures, considering other kind of tunable components and agile devices with promising properties. Hence, further special attention to the integration of the FPGA-WARP embedded module within the presented architectures is required.

In conclusion, from a general perspective and considering the diverse topics treated throughout this work, a significant understanding going from the theory and conception up to the implementation, to turn current communication architectures into efficient reconfigurable architectures has been acquired, demonstrated and discussed. Due to important achievements in diverse fields of technologies, from the groundworks in material sciences to the development of novel components in the area of microwave technology, a new era of autonomous wireless sensors, devices and networks will enable the convergence and creation of ever-increasing smart air interfaces.

Appendix

A.1 Group Delay Considering the Excitation of Two Cosinusoidal Responses

To investigate the influence of distortion in the phase of a component, the frequency response of a filter is considered [1]. Hence, for an arbitrary filter its transfer function can be expressed in terms of its zeros and poles as

$$H(j\omega) = |H(j\omega_0)|e^{j\theta(\omega_0)} = \frac{H_0 \Pi_{i=1}^{M}(j\omega - z_i)}{\Pi_{i=1}^{N}(j\omega - p_i)}, \tag{A.1}$$

where $|H(j\omega_0)|$ and $\theta(\omega_0)$ are the respectively amplitude and phase responses with center frequency ω_0.

Assuming an excitation composed by the sum of two cosinusoidal responses to the filter input of the form

$$x(t) = A_1 \cos(\omega_0 t) + A_2 \cos[(\omega_0 + \Delta\omega)t] \tag{A.2}$$

with frequencies $\Delta\omega \ll \omega_0$, the filter output yields

$$\begin{aligned} y(t) = {} & A_1 |H(j\omega_0)| \cos[\omega_0 t + \theta(\omega_0)] \\ & + A_2 |H[j(\omega_0 + \Delta\omega)]| \cos[(\omega_0 + \Delta\omega)t + \theta(\omega_0 + \Delta\omega)]. \end{aligned} \tag{A.3}$$

To express the change of the phase in terms of the frequency at ω_0 and $\omega_0 + \Delta\omega$ terms, (A.3) is rearranged as

$$\begin{aligned} y(t) = {} & A_1 |H(j\omega_0)| \cos\left\{\omega_0 \left[t + \tfrac{\theta(\omega_0)}{\omega_0}\right]\right\} \\ & + A_2 |H[j(\omega_0 + \Delta\omega)]| \cos\left\{(\omega_0 + \Delta\omega)\left[t + \tfrac{\theta(\omega_0 + \Delta\omega)}{\omega_0 + \Delta\omega}\right]\right\}. \end{aligned} \tag{A.4}$$

E. Gonzalez Rodriguez, *Reconfigurable Transceiver Architecture for Multiband RF-Frontends*, Smart Sensors, Measurement and Instrumentation 17,
DOI 10.1007/978-3-319-24581-2

Considering the definition of the derivative with respect to the center frequency [2]

$$\frac{\partial\theta(\omega_0)}{\partial\omega_0} \cong \frac{\theta(\omega_0+\Delta\omega)-\theta(\omega_0)}{\Delta\omega}, \tag{A.5}$$

the phase shift with respect to the frequency change can be expressed as

$$\frac{\theta(\omega_0+\Delta\omega)}{\omega_0+\Delta\omega} = \left(\frac{\theta(\omega_0)}{\omega_0} + \frac{\Delta\omega}{\omega_0}\cdot\frac{\partial\theta(\omega_0)}{\partial\omega_0}\right)\left(\frac{\omega_0}{\omega_0+\Delta\omega}\right). \tag{A.6}$$

By applying a Taylor series expansion of the second term in (A.6) considering $\frac{\Delta\omega}{\omega_0} \ll 1$, i.e. $\Delta\omega_0$ becomes infinitesimally small compared to the operation frequency, the expression can be reduced to

$$\frac{\theta(\omega_0+\Delta\omega)}{\omega_0+\Delta\omega} \cong \frac{\theta(\omega_0)}{\omega_0} + \left(\frac{\partial\theta(\omega_0)}{\partial\omega_0} - \frac{\theta(\omega_0)}{\omega_0}\right)\frac{\Delta\omega}{\omega_0}. \tag{A.7}$$

Substituting expression (A.7) into (A.4), yields

$$\begin{aligned} y(t) = A_1|H(j\omega_0)|\cos\left\{\omega_0\left[t+\tfrac{\theta(\omega_0)}{\omega_0}\right]\right\} \\ + A_2|H[j(\omega_0+\Delta\omega)]|\cos\left\{(\omega_0+\Delta\omega)\left[t+\tfrac{\theta(\omega_0)}{\omega_0}+\tau_T\right]\right\}, \end{aligned} \tag{A.8}$$

where the overall delay τ_T in terms of the frequency change

$$\tau_T = \frac{\Delta\omega}{\omega_0}\cdot\left(\frac{\partial\theta(\omega_0)}{\partial\omega_0} - \frac{\theta(\omega_0)}{\omega_0}\right) \tag{A.9}$$

includes the phase delay

$$\tau_\mathrm{p} = \frac{\theta(\omega_0)}{\omega_0}, \tag{A.10}$$

and group delay

$$\tau_\mathrm{g} = \frac{\partial\theta(\omega_0)}{\omega_0}. \tag{A.11}$$

A.2 Directional Coupler Four-Port Network

A directional coupler can be described based on the complex scattering parameters matrix of a reciprocal four-port network in the following form:

$$\overline{S} = \begin{pmatrix} S_{11} & S_{12} & S_{13} & S_{14} \\ S_{21} & S_{22} & S_{23} & S_{24} \\ S_{31} & S_{32} & S_{33} & S_{34} \\ S_{41} & S_{42} & S_{43} & S_{44} \end{pmatrix}. \tag{A.12}$$

If a scenario takes into account the magnitude values of a symmetric directional coupler with a coupling coefficient κ, the S-matrix can be defined as

$$|S| = \begin{pmatrix} S_{11,\,\mathrm{min}} \to 0 & S_{12,\,\mathrm{max}} \to 1 & \kappa & S_{41,\mathrm{min}} \to 0 \\ S_{21,\,\mathrm{max}} \to 1 & S_{22,\,\mathrm{min}} \to 0 & S_{32,\,\mathrm{min}} \to 0 & \kappa \\ \kappa & S_{32,\,\mathrm{min}} \to 0 & S_{33,\,\mathrm{min}} \to 0 & S_{43}, \to 1 \\ S_{41,\,\mathrm{min}} \to 0 & \kappa & S_{43,\mathrm{max}} \to 1 & S_{44,\mathrm{min}} \to 0 \end{pmatrix}. \tag{A.13}$$

Quantities used to characterize a directional coupler [3]:

Coupling	$\kappa = 10 \log \frac{P_1}{P_3}$ dB
Isolation	$I = 10 \log \frac{P_1}{P_4}$ dB
Directivity	$D = 10 \log \frac{P_3}{P_4}$ dB

The coupling factor points out the fraction of the input power present at the coupled port. The isolation is a measure to indicate the amount of delivered power to the isolated port, in the ideal case no power is delivered. The directivity indicates the level of isolation between the forward and backward waves.

A.3 Digital Analog Converter Static Performance

In a D/A converters two specifications evaluate the accuracy among analog values that correspond to a given digital input.

The differential nonlinearity of transition n [4] can be described as

$$\mathrm{DNL}_n = \mathrm{A_i} - \mathrm{I_i}, \tag{A.14}$$

where $\mathrm{A_i}$ is the actual increment height and $\mathrm{I_i}$ the ideal increment height at the given transition. Once both, the offset and gain errors have been substracted, the integral nonlinearity value can be obtained, i.e. the overall deviation from the original response [5]. Therefore, it can be defined as

$$\mathrm{INL}_n = \mathrm{In_{code}} - \mathrm{Ref_{value}}, \tag{A.15}$$

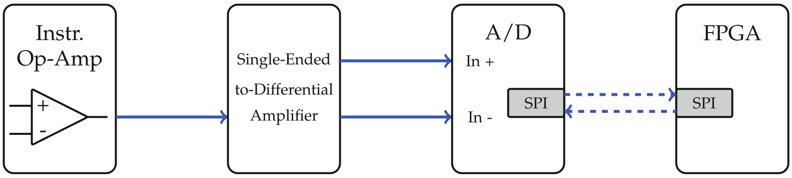

Fig. A.1 Detailed block diagram of the detected voltage path from the outputs of the detector module at ports 3 and 4 up to the input at the FPGA

where In_{code} is the output value for input code n and $\text{Ref}_{\text{value}}$ represents the output value of the reference line at the evaluated point [4].

A.4 Analog-to-Digital Conversion with Driver Stage

To perform analog-to-digital conversion, the employed 20-bit A/D converter LTC2377 from manufacturer Linear Technology [6] requires a differential input signal. And since the instrumentation amplifier INA116 from manufacturer Texas Instruments [7] outputs a single-ended voltage signal, a so called driver stage is necessary previous to the A/D converter. In this case, the IC LT6203 from Linear Technology [8] is used as the A/D driver. Figure A.1 shows the implemented solution.

A.5 FPGA Voltage Translation for High-Voltage CMOS D/A Converters

The FPGA embedded in the WARP Radio module outputs signals with 2.5 V. This voltage differs from the required −3.3 V inputs of the CMOS high voltage D/A converters to perform digital-to-analog conversion.
Generation of required voltage at inputs of high voltage D/A converter:

1. Translation from 2.5 to 3.3 V employing the IC 74AVCH20T245 from manufacturer NXP [9].
2. Inversion of voltage level to obtain −3.3 V using four LM324-N ICs quadruple operational amplifiers from Texas Instruments [10] to cover the necessary 16-bit of the HV CMOS D/A converters.

Figure A.2 describes the voltage translation from outputs at the FPGA down to high voltage D/A converters.

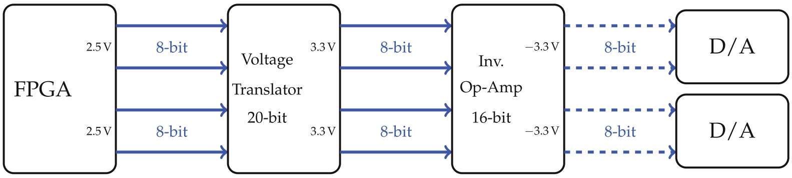

Fig. A.2 Detailed block diagram of the voltage conversion from the FPGA into the D/As. First, voltage is translated to a 3.3 V signal level, and then inverted to obtain the required −3.3 V level by the two 8-bit CMOS high voltage D/A converters

A.6 Integrated Circuits for Adaptive Control with Detector Module

Description	Component	Package
A/D converter	LTC2377-20	MSOP 16
A/D driver	LT62023	SO 8
Voltage translator	74AVCH20T245	TSSOP 56
Operational amplifier	LM324-N	DIP 14
Instrumentation amplifier	INA116	DIP 16

NR: Not required

References

1. A. Antoniou, *Digital Signal Processing: Signals, Systems, and Filters* (McGraw-Hill Publishing, New York, 2005)
2. C. Jordan, *Calculus of Finite Differences* (Chelsea Publishing Company, New York, 1950)
3. D. Pozar, *Microwave Engineering* (McGraw-Hill Publishing, New York, 1998)
4. R.J. Baker, H.W. Li, D.E. Boyce, *CMOS Circuit Design Layout and Simulation* (Wiley, New York, 1997)
5. D .A. Johns, K. Marin, *Analog Integrated Circuit Design* (Wiley, New York, 1997)
6. Linear Technology LTC2377 Datasheet. Low noise, low power, high speed 20-bit successive approximation register (SAR) ADC (2013)
7. Texas Instruments INA116 Datasheet. Ultra low input bias current instrumentation amplifier (2009)
8. Linear Technology LT6203 datasheet. Single/dual/quad 100 MHt, rail-to-rail input and output, ultralow noise, low power operational amps (2009)
9. NXP 74AVCH20T245 Datasheet. 20-bit dual suppliy translating transceiver with configurable voltage translation (2011)
10. Texas Instruments LM324-N Datasheet. Low power quadruple operational amplifier (2004)

Publications

1. M. Maasch, M. Schüßler, **E. González-Rodríguez**, C. Damm, G. Lubkowski, and R. Jakoby, “Voltage tunable split-ring-resonators for waveguide applications,” in *Proceedings of 3rd International Congress on Advanced Electromagnetic Materials in Microwaves and Optics, METAMATERIALS, (London, UK), August*, 2009
2. M. Maasch, C. Damm, **E. González-Rodríguez**, and R. Jakoby, “Measurement setup for effective material parameter extraction of dc biased artificial material structures,” in *Microwave Conference (EuMC), 2011 41st European*, pp. 357–360, Oct 2011
3. Y. Zheng, H. Maune, M. Sazegar, X. Zhou, **E. González-Rodríguez**, A. Mehmood, B. Baumgarten, and R. Jakoby, “Ferroelectric thick-film components for reconfigurable wireless communications,” in *European Meeting on Ferroelectricity (EMF2011), Bordeaux*, 2011
4. K. Kastell, T. Daskalou, **E. González-Rodríguez**, and R. Jakoby, “Potential of software-defined radios to enhance the quality of hybrid networks,” in *Microwaves, Communications, Antennas and Electronics Systems (COMCAS), 2011 IEEE International Conference on*, pp. 1–4, Nov 2011
5. K. Kastell, **E. Gonzáilez-Rodríguez**, T. Daskalou, and R. Jakoby, “Overview of implementation constraints for flexible and intelligent hybrid networks,” in *Applied Electrical Engineering and Computing Technologies (AEECT), 2011 IEEE Jordan Conference on*, pp. 1–5, Dec 2011
6. M. Maasch, C. Damm, M. Schüßler, **E. González-Rodríguez**, and R. Jakoby, “Varactor loaded tunable split ring resonators with simple biasing network,” in *Microwave Conference (GeMIC), 2011 German*, pp. 1–4, March 2011
7. **E. González-Rodríguez**, H. Maune, Y. Zheng, L. Shen, I. Shah, K. Hofmann, D. Dahlhaus, and R. Jakoby, “Impact of group delay on tunable impedance matching networks based on barium-strontium-titanate varactors,” in *Signals, Systems, and Electronics (ISSSE), 2012 International Symposium on*, pp. 1–5, Oct 2012

E. Gonzalez Rodriguez, *Reconfigurable Transceiver Architecture for Multiband RF-Frontends*, Smart Sensors, Measurement and Instrumentation 17,
DOI 10.1007/978-3-319-24581-2

8. K. Hofmann, L. Shen, **E. González-Rodríguez**, H. Maune, I. Shah, D. Dahlhaus, and R. Jakoby, "Fully integrated high voltage charge pump for energy-efficient reconfigurable multi-band rf-transceivers," in *Telecommunications Energy Conference (INTELEC), 2012 IEEE 34th International*, pp. 1–4, Sept 2012
9. **E. González-Rodríguez**, H. Maune, L. Shen, I. Shah, D. Dahlhaus, K. Hofmann, and R. Jakoby, "Reconfigurable radio frontends for cooperative sensor networks: Tasks and challenges," in *Signal Processing Advances in Wireless Communications (SPAWC), 2013 IEEE 14th Workshop on*, pp. 515–519, June 2013
10. **E. González-Rodríguez**, H. Maune, Y. Zheng, M. Sazegar, L. Shen, I. Shah, D. Dahlhaus, K. Hofmann, and R. Jakoby, "Tunable ferroelectric impedance matching networks and their impact on digital modulation system performance," AEÜ - International Journal of Electronics and Communications, vol. 67, no. 12, pp. 1107–1117, 2013
11. L. Shen, M. Saif, J. Ning, **E. González-Rodríguez**, H. Maune, R. Jakoby, and K. Hofmann, "*Integrierte hochvolt cmos asics zur ansteuerung von rekonfigurierbaren rf-frontends*," in 15. *Workshop Analogschaltungen am RBZ, Reutlingen, 2013*
12. **E. González-Rodríguez**, H. Maune, Y. Zheng, and R. Jakoby, "Universal wideband reconfigurable transceiver with extended frequency range up to 6 GHz," in *Radio and Wireless Symposium (RWS), 2014 IEEE*, pp. 40–42, Jan 2014
13. **E. González-Rodríguez**, A. Mehmood, Y. Zheng, H. Maune, L. Shen, J. Ning, H. Braun, M. Hovhannisyan, K. Hofmann, and R. Jakoby, "Reconfigurable dual-band antenna module with integrated high voltage charge pump and digital analog converter," in *Antennas and Propagation (EuCAP), 2014 8th European Conference on*, pp. 2749–2753, April 2014
14. **E. González-Rodríguez**, Y. Zheng, H. Maune, R. Jakoby, *Future Reconfigurable Radio Frontends for Cognitive Radio and Software Defined Radio: from Functional Materials to Spectrum Management (Chapter) in Software-Defined and Cognitive Radio Technologies for Dynamic Spectrum Access and Management.* IGI Global, Hershey, PA, United States, Wen-Chen, H. and Kaabouch, Naima, 2014
15. J. Ning, L. Shen, **E. González-Rodríguez**, and K. Hofmann, "An integrated high voltage digital-to-analog converter for a reconfigurable antenna array," *Analog Integrated Circuits and Signal Processing*, vol. 80, pp. 407–415, September 2014